Doctoral Thesis

University of Limoges
Ecole Doctorale Sciences et Ingénierie (SI) ED 653
Institute of Research for Ceramics (IRCER)

Thesis to obtain the degree of
Doctor of Philosophy of the University of Limoges
Ceramic Materials and Surface Treatments

Presented by
Kinga SZTYMELA
25th of September 2023

Fabrication of 3D electrodes for modern lithium-ion batteries by inkjet printing: opportunities and challenges

Thesis supervised by Fabrice ROSSIGNOL and Manuella CERBELAUD

JURY :

President of Jury :
Christel Laberty-Robert, Professor - Sorbonne Université (France)

Reviewers :
Christel Laberty-Robert, Professor - Sorbonne Université (France)
Lionel Presmanes, Research Director - Institut Carnot Chimie Balard Cirimat Toulouse (France)

Examiners :
Giorgia Franchin, Associate Professor - University of Padova (Italy)
Eduardo Saiz, Professor - Imperial College London (UK)
Andrea Zocca, Junior Researcher - BAM (Germany)
Manuella Cerbelaud, Researcher - IRCER, University of Limoges (France)
Fabrice Rossignol, Research Director - IRCER, University of Limoges (France)

I would like to express my heartfelt dedication of this thesis to my beloved parents, Mariola and Andrzej, as well as my great brothers, Szymon and Sebastian. You have been my unwavering source of strength, propelling me forward to successfully complete this academic journey. Despite the physical distance that has separated us, I always knew that I could rely on you during the most challenging moments.

Z głębi serca chciałabym zadedykować tę pracę moim ukochanym rodzicom, Marioli i Andrzejowi oraz moim wspaniałym braciom, Szymonowi i Sebastianowi. Byliście moim niezachwianym źródłem siły, napędzającej do pomyślnego ukończenia tej akademickiej podróży. Mimo dzielącej nas odległości, zawsze wiedziałam, że mogę na Was polegać w najtrudniejszych chwilach.

Remember to look up at the stars and not down at your feet. Try to make sense of what you see and wonder about what makes the Universe exist. Be curious. And however difficult life may seem, there is always something you can do and succeed at. It matters that you don't just give up.

Stephen Hawking

Acknowledgement

This project has received funding from the European Unions's Horizon 2020 research and innovation programme under grant agreement N° 875029. I would like to thank all the project partners who contributed to the work, especially colleagues from CEA, Fraunhofer IKTS, Umicore, DAIKINI, and Nanomakers. I sincerely appreciate the three years of exciting collaboration we have shared.

I would like to express my deepest gratitude to my supervisors, Manuella Cerbelaud and Fabrice Rossignol. Your unwavering support, guidance, and expertise have been invaluable. Not only have you generously shared your vast knowledge and insights, but you have created an outstanding working environment throughout the duration of my research. Thank you for making this journey an enjoyable and fulfilling experience. It has been an absolute pleasure collaborating with both of you.

I am also thankful to the staff of IRCER who have kindly provided me with assistance and advice: Pierre-Marie Geffroy, Marguerite Bienia, Pierre Carles, Julie Cornette, Julie Bourret, Marina Soustre, Sandra Blanchet, Mickaël Lacroix. Furthermore, I would like to extend my sincere thanks to the administrative department, specifically to Paméla Bathias and Valérie Magliulo. Thank you for your invaluable support!

Words cannot express my gratitude to the most important people in my life - my family. You are a huge part of this journey. You gave me a lot of power, confidence, and motivation!
I would like to thank my parents, Mariola and Andrzej for being for me all the time, for listening about my joys and sorrows, for your willingness to help, for your care and all the love you gave me. You are irreplaceable, and I am very grateful that I can always count on you.
I express my gratitude to two equally significant individuals in my life, my exceptional brothers, Szymon and Sebastian. Thank you for making me feel safe, and always believing in me. Whenever I faced challenges, I knew that you are ready to help me, which gave me the courage to continue.
Thank you to my excellent grandmother - Natalia, for all the love, empathy, and positivity. For the fact that like no one else you enjoyed my happiness and you grieved with me in difficult times. Your indulgence and understanding are invaluable.

I am extremely grateful to my dear friends who have supported me along this journey, whether near or far.
Laura, having you as my friend has brought me immense joy, as no one else celebrates my accomplishments quite like you do. I am truly grateful for your presence during even the toughest times, as you have provided me with boundless courage and motivation to persevere. Thank you for standing by my side and inspiring me to keep going.
Camellia, I want to express my gratitude for the countless moments and conversations we've shared. I knew I could always rely on you. Thank you for being an exceptional listener, for helping me grow, and for your genuine sensitivity and open-heartedness. Your presence in my life is truly treasured.
Roberta, thank you for always being there with a listening ear and words of encouragement. Your wisdom, kindness, understanding, loyalty, and willingness to lend a helping hand have eased the burdens along this path.
Angelika, thank you for your unwavering presence in both the good and challenging moments of my life. The moments we have shared together, filled with laughter and meaningful conversations, hold a special place in my heart. I am sincerely thankful for your understanding, which has offered me comfort and support.
Justyna, I am grateful for the countless conversations we have shared! Thank you for being an exceptional cousin and an incredible source of support.
To the best office mate, Raghvender. Thank you for all the conversations, help, and technical support!
I would like to extend the same sentiments of gratitude and appreciation to Marta, Julia, Wojtek, Alicja, Kasia, Maja, Remik, Gosia, Dawid, Munni, and Firas.

Special thanks go to Wojtuś, who has made the last months of this academic journey very colorful and special. You have been my rock and my source of support. Thank you for being next to me, for your patience, and indulgence, for all the deep conversations we have shared, and for making me smile. Your big heart has made this time significantly more manageable. Thank you sincerely for being by my side!

Podziękowania

Słowa nie są w stanie wyrazić mojej wdzięczności dla najważniejszych osób w moim życiu - mojej rodziny. Jesteście ogromną częścią tej podróży. Daliście mi dużo siły, pewności siebie i motywacji!

Chciałabym podziękować moim rodzicom, Marioli i Andrzejowi za to, że cały czas byliście dla mnie, słuchaliście o moich radościach i smutkach, za chęć pomocy, za troskę i całą miłość, którą mnie obdarzyliście. Jesteście niezastąpieni i jestem bardzo wdzięczna, że zawsze mogę na Was liczyć.

Wyrażam wdzięczność dwóm równie ważnym osobom w moim życiu, moim wyjątkowym braciom, Szymonowi i Sebastianowi. Dziękuję za poczucie bezpieczeństwa i za to że zawsze we mnie wierzyliście. Ilekroć stawałam przed wyzwaniami, wiedziałam, że jesteście gotowi mi pomóc, co dodawało mi odwagi do dalszego działania.

Dziękuję mojej wspaniałej babci - Natalii, za całą miłość, empatię i pozytywne nastawienie. Za to, że jak nikt inny cieszyłaś się moim szczęściem i smuciłaś ze mną w trudnych chwilach. Twoja wyrozumiałość i zrozumienie są nieocenione.

Droits d'auteurs

Table of contents

List of Figures

List of Tables

List of Abbreviations

3D – Three-Dimensional.
3D-SPE – 3D-Archimedean Spiral Structured Solid Polymer Electrolyte.

AEM – Active Electrode Material.
AJP – Aerosol Jet Printing.
AM – Additive Manufacturing.
ATD – Atomic Layer Deposition.

CA – Conductive Agent.
CAD – Computer-Aided Design.
CE – Coulombic Efficiency.
CIJ – Continuous Inkjet.
CMC – Carboxymethyl Cellulose.
CNTs – Carbon Nanotubes.

DIW – Direct Ink Writing.
DLS – Dynamic Light Scattering.
DOD – Drop on Demand.

EIS – Electrochemical Impedance Spectroscopy.
EVs – Electric Vehicles.

FDM – Fused Deposition Modeling.
FFF – Fused Filament Fabrication.
FIB-SEM – Focused Ion Beam Scanning Electron Microscopy.
FWHM – Full Width at Half Maximum.

HPE – Hybrid Polymer Electrolyte.

ICE – Internal Combustion Engine.

ICP – Inductively Coupled Plasma.
IEP – Iso-Electric Point.
IJP – Inkjet Printing.

KBr – Potassium Bromide.

LFP – $LiFePO_4$.
LIBs – Lithium-Ion Batteries.
LMD – Laser Metal Deposition.
LTO – $Li_4Ti_5O_{12}$.

NMC – $LiNi_xCo_yMn_zO_2$.
NMC333 – $LiNi_{0.3}Mn_{0.3}Co_{0.3}O_2$.
NMC622 – $LiNi_{0.6}Mn_{0.2}Co_{0.2}O_2$.
NMP – N-Methyl Pyrrolidone.

PAMA – Poly-Acrylic-co-Maleic Acid.
PEDOT:PSS – Poly(3,4-ethylenedioxythiophene) Polystyrene Sulfonate.
PEO – Poly(ethylene oxide).
PS – Polystyrene.
PVD – Physical Vapor Deposition.
PVDF – Polyvinylidene Fluoride.
PVP – Polyvinylpyrrolidone.
PZC – Point of Zero Charge.

SDL – Selective Deposition Lamination.
SEI – Solid Electrolyte Interface.
SiNPs – Silicon Nanoparticles.
SiNTs – Silicon Nanotubes.
SiNWs – Silicon Nanowires.
SLA – Stereolithography.
SLS – Selective Laser Sintering.
SSP – Size-Strain Plot.

UDM – Uniform Deformation Model.

W-H – Williamson-Hall.

0

General introduction

In recent years, the climate crisis became one of the biggest concerns of humanity. Global warming is accelerating, posing a threat to both people and the environment [1]. The excessive emission of CO_2, as the primary greenhouse gas is the main responsible for this problem [2]. As pandemic restrictions were eased, and passenger and goods movements began to take up after a historic fall in 2020, worldwide CO_2 emissions from the transport sector rebounded in 2021, accounting for 37% of CO_2 emissions from end-use sectors [3]. Following the commitment from COP21 Paris Climate Agreement and COP26 Glasgow Climate Pact, major car manufacturers pledged to stop selling fossil-fuel vehicles by 2035, promoting transport electrification, and increasing demand for batteries' production [4], [5]. Because of their high energy density to weight ratio, lithium-ion batteries (LIBs) are the most common energy storage systems used in the fabrication of electric vehicles (EVs) [6]. Although LIBs are state-of-the-art technology for EVs, their further development is anticipated, particularly in terms of energy density, power density, safety, life cycle, and cost [7].

One of the possible strategy for enhancing the battery performance include the implementation of advanced materials with relatively high energy and power densities.
Ni-rich $LiNi_xCo_yMn_zO_2$ (NMC) is a popular cathode material for LIBs chosen by many car manufacturers [8]. It provides high capacity, high rate capability, and improved structural stability [9].
Concerning the anode, the replacement of conventional graphite with silicon can significantly enhance the electrochemical characteristics of batteries. Silicon (Si) shows great promise for modern LIBs due to its high theoretical specific capacity ($4200\,\mathrm{mAhg^{-1}}$), which is 11 times higher than graphite ($372\,\mathrm{mAhg^{-1}}$) [10]. However, Si experiences significant volumetric changes (up to 400%) during lithiation/delithiation processes, which leads to electrode structure degradation, and consequently poor cycling stability [11], [12]. To overcome these challenges, various strategies have been proposed, such as the use of nanosized Si or carbon-coated Si materials.

Another promising strategy for the fabrication of the next-generation LIBs is an improved design of the electrodes using three-dimensional (3D) structures. The conventional layered electrodes, whose fabrication method is already well-elaborated and easily implementable for large-scale production, face a trade-off between energy density and power density [13]. Alternatively, 3D battery architecture offers a favorable balance by effectively exploiting the electrode's volume. Unlike planar structures, 3D electrodes offer a larger surface area that facilitates efficient ion transport and minimizes diffusion distances within the electrode. This facilitates faster charging and discharging, resulting in enhanced power density. At the same time, the 3D architecture allows for increased active material loading, enhancing energy density [14].

Many additive manufacturing (AM) techniques have been proposed for the fabrication of modern 3D batteries' structures: direct ink writing (DIW) [15], fused filament fabrication (FFF) [16], stereolithography (SLA) [17], aerosol jet printing (AJP) [18] and drop-on-demand (DOD) inkjet printing (IJP) [19]. Among them, DOD IJP offers many advantages over competing technologies. It allows for the deposition of a broad range of materials with high resolution and relatively high speed [20], [21]. The fast fabrication may be particularly interesting for the industry, where batteries are produced at large scale. In this technique, the picoliter droplets (typically in the range of 1-1000pL) of a functional ink are placed on a substrate, forming a pattern dictated by a CAD file [22], [23]. Therefore, the printed design can be easily modified, offering advantages in terms of scalability and affordability, while also minimizing the amount of wasted material.

The scope of this thesis was to examine the possibilities of fabrication of modern electrode architectures with state-of-the-art materials by IJP technology. This work was done in the frame of the European project ASTRABAT under grant agreement No 875029, which aims to develop optimal lithium-ion battery solutions for the increasing demands of the electric vehicle market in particular.

Chapter 1 provides a general overview of the research topic, focusing on the market of LIBs, materials used for their fabrication, and manufacturing methods. Inkjet printing technology is presented in detail, and the requirements for the ink formulations are discussed.
Chapter 2 summarizes the materials, different techniques and experimental methods used in the work.
In Chapter 3, a comparison of different milling techniques applied to grind cathode active material is presented, along with an analysis of their effects on the final powder properties. The changes in the materials' structure are evaluated through XRD analysis, and the electrochemical properties are also discussed.
The main topic of Chapter 4 is the fabrication of anodes using IJP technology. The formulation of stable aqueous inks using Si as an active material is covered in detail and their electrochemical properties are analyzed to assess the effect of compositions. Printability tests are performed, revealing the importance of powder surface chemistry.

Microstructural characterizations of printed patterns are presented. Finally, we address the issue of particle emissions during ink preparation and inkjet printing, and present measurements showing that the processes are safe for human health.

Chapter 5 is analogous to Chapter 4, but it focuses on the fabrication of the positive electrode. It discusses the development of stable inks using both water-based and organic solvents and assesses their impact on electrochemical properties. Printability tests are demonstrated revealing the strain hardening phenomenon, and other issues, which may hinder the ejection. Microstructural characterization of deposited structures is presented, followed by particle emission measurements.

1

Introduction

Summary

1.1 Lithium-ion batteries

1.1.1 Li-ion batteries - working principle

Lithium-ion batteries surpassed all other power sources in portable electronics and are widely considered the key battery technology for Electric Vehicles (EVs) [24]. They are credited for altering communications and transportation, allowing for the development of ultra-thin smartphones and long-range EVs [25]. The use of lithium, the lightest metallic element and one with the lowest density, makes this possible. Moreover, it shows the lowest standard electrode potential versus the standard hydrogen electrode (-3.04 V). LIBs offer the highest volumetric and gravimetric energy density among other known systems, like lead-acid, nickel-cadmium, and nickel metal hydroxide batteries [26].

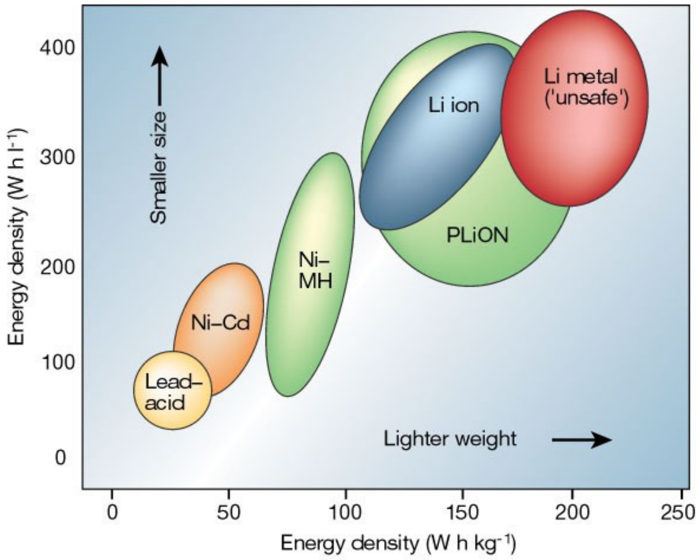

Figure 1.1: Volumetric and gravimetric energy densities for different battery technologies [26].

As shown in Figure 1.1, lithium batteries that use lithium metal as the anode have more advantageous characteristics than lithium-ion batteries. However, because of the high reactivity of metallic lithium and the safety issues, they were replaced by Li-ion batteries, where Li is only present in ionic form in electrolytes and on an atomic scale when intercalated into an anode [27].

LIBs generally consist of an anode, cathode, electrolyte, separator, and two current collectors (positive and negative). The electrical energy is stored in electrodes undergoing simultaneous oxidation and reduction processes. While charging, Li^+ ions are transported from the cathode host, passing through the electrolyte, and inserted into the anode. During the discharge, the process is reversed, and the electrons pass around the external circuit, providing electrical energy [28]. A schematic representation of the working principle of LIBs is shown in Figure 1.2.

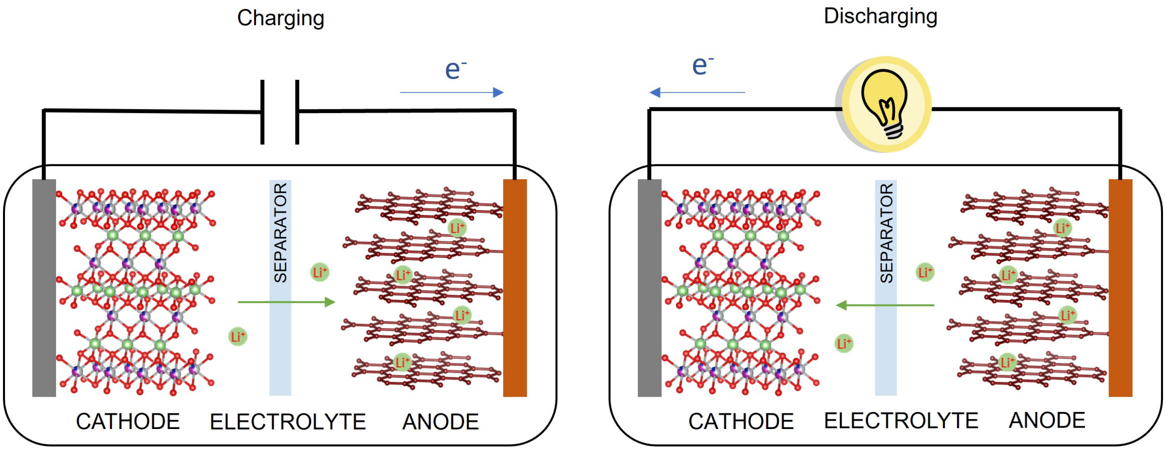

Figure 1.2: Schematic representation of the working principle of Li-ion batteries.

Taking $LiCoO_2$ as a cathode and graphite as an anode, the oxidation-reduction reactions taking place in the cell may be represented as follows:

Cathode:

$$\mathrm{Li_{1-x}CoO_2 + xLi^+ + xe^- \Leftrightarrow LiCoO_2}$$

Anode:

$$\mathrm{Li_xC_6 \Leftrightarrow +xLi^+ + xe^- + C_6}$$

The full reaction:

$$\mathrm{LiC_6 + CoO_2 \Leftrightarrow C_6 + LiCoO_2}$$

1.1.2 Li-ion batteries for electric vehicles - market

Once more, we are in the era of electric vehicles. Surprisingly, the rechargeable electric car is not a recent concept. The story began with the invention of lead-acid batteries in 1859 by Gaston Planté [29]. Camille Faure developed them in 1881, giving birth to the first rechargeable batteries for automobiles [30]. In April 1881, French inventor Gustave Trouvé tested the first human-carrying electric vehicle (with lead-acid batteries) on a Paris street - the Trouvé tricycle (Figure 1.3) [31].

Also, in 1881 Englishmen William Ayrton & John Perry constructed an electric tricycle with electric lights powered by ten lead-acid cells, providing 1/2 horsepower. The maximum speed was approximately 14 km/h, and the distance traveled with a single charge ranged from 16 to 40 kilometers depending on the terrain [32].

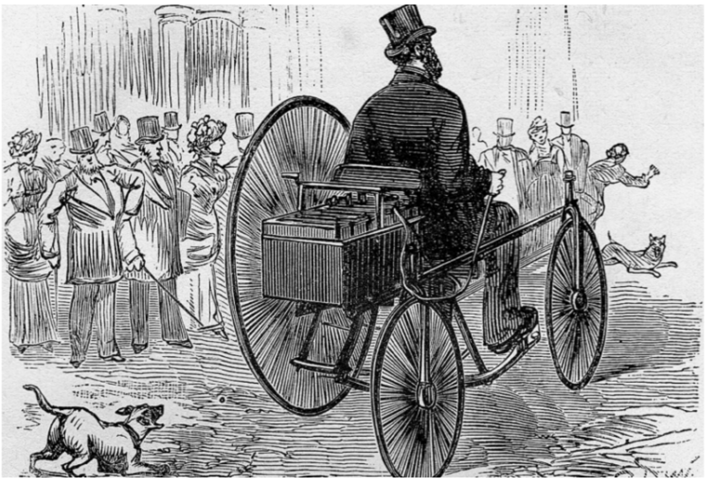

Figure 1.3: The first human-carrying electric vehicle invented by Gustave Trouvé [31].

The first automobile company, which produced electric vehicles for many years with the brand name *Jeantaud*, was created in 1893 by Charles Jeantaud. With a 36 horsepower car, they set the world record, at an average speed of 70 km/h. In 1899, the Belgian Camille Jenatzy broke the record with *Jamais contente* reaching 100 km/h.
Electrobat is thought to be the first successful vehicle. It was designed and constructed by mechanical engineer Henry G. Morris and chemist Pedro G. Salom in Philadelphia, Pennsylvania, in 1894. The initial version of this car was extremely heavy and slow, having steel tires to handle the massive weight of its massive lead battery. Later models were lighter and had pneumatic tires, allowing 40 kilometers per charge and a max speed of 32 km/h [33].
During the First World War, the demand for electric cars significantly increased. In 1914, the total number of electric vehicles in Europe was estimated to be around 3 200. Soon after, a series of events caused the development and mass production of petrol-powered cars, and the popularity of electric propulsion notably decreased. First and foremost, people had higher expectations. Since the quality of road infrastructure improved, it was feasible to travel long distances. As a result, a vehicle with a more extended range per charge and higher speed was desired. Fuel became widely available and affordable after substantial oil reserves were discovered in Texas, Oklahoma, and California. Furthermore, the use of silencers made the noise bearable. In the early 1900s, Henry Ford pioneered the mass production of gasoline-powered automobiles launching the Model T into the market. This car was competitively priced, making it accessible to the general public. In 1915, its price was 350$, and Ford Motor Company sold 472 350 copies [34], [35].

The popularity of fuel vehicles persisted until the 1970s energy crisis, which resulted in a rise in gasoline prices. It was the first event that once again sparked increased interest in electric cars. A new era began with the invention of nickel-metal hydride batteries in the 1990s and lithium-ion batteries in the 2000s [37]. With that, the green movement in the 1990s and early twenty-first century began to promote the idea of environmentally friendly cars that emit less pollution [33].

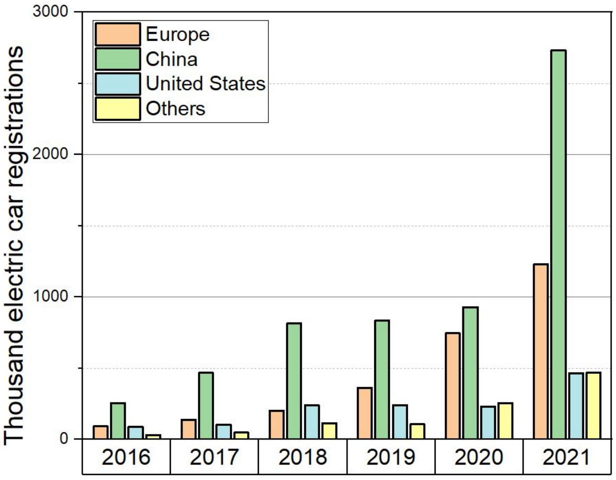

Figure 1.4: Electric car registrations in Europe, China, Unites States and other regions over the period 2016-2021. The data were taken from the report Global EV Outlook 2022 [36].

Following the COP21 Paris Climate Agreement [38], and COP26 Glasgow Climate Pact [5], major automakers (including GM, Ford, Volvo, BYD Auto, Jaguar Land Rover, and Mercedes-Benz), along with the governments of 24 wealthy nations, pledged to sell only electric cars globally by 2040, and in leading markets by 2035.

The electrification of transportation accelerated worldwide, not only in Europe. The chart in Figure 1.4 shows the number of registered electric cars in Europe, China, United States and other regions over the period 2016-2021.

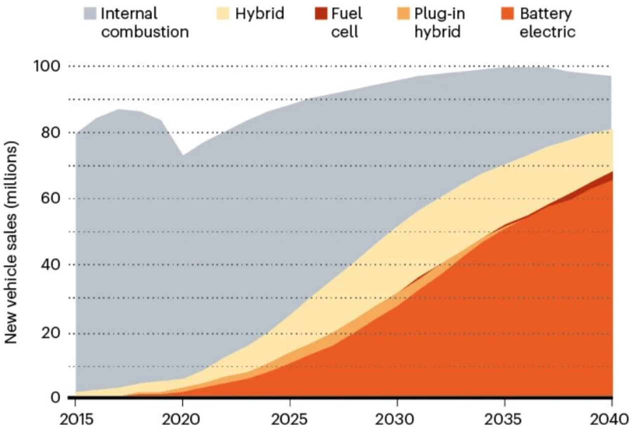

Figure 1.5: Sales of new vehicles worldwide over the period 2015-2040 [39].

In China, Europe, and other areas, the registration of EVs increased more than 10 times, with the highest number of 2 734 thousand registered cars in 2021 in China. In United States, a five-fold increase was observed.

It is anticipated that more and more vehicles with huge batteries inside will be on the road in the upcoming decades. According to the forecast *Bloomberg Finance LP* (Figure 1.5), electric vehicles are expected to account for over

50% of global new passenger car sales by the year 2040 [39].

The accelerated growth of the production of EVs entails increased interest in LIBs, which are the most common energy storage systems employed in the fabrication of modern electric cars [6].

This outstanding success is a result of their high energy and power density, long cycle life, relatively high level of safety, and gradually declining cost. Although LIBs are already very advanced, further development is required before EVs can compete with cars powered by Internal Combustion Engine (ICE) [7].

The main aspects that need to be improved are listed below [40], [41]:

Energy density - One of the major problems of EVs is the driving range of a vehicle, *i.e.*, the distance which can be traveled on a single charge of battery. This is dictated by the energy density, which is described as the amount of energy stored per volume or weight unit. The energy density may be increased by the multiplication of the number of batteries, which in turn contributes to the overall weight and cost of vehicles. Battery packs include not only cells but also additional components, such as thermal elements, busbars, battery management systems, *etc.* Therefore, cell design and packing efficiency should be improved to have a higher energy density.

Power density - Another important factor to consider when selecting an electric vehicle is power density, which represents the charging time. Currently, charging an EV takes hours (normal charging), which is problematic for driving long distances. The goal is to reduce the time to 10-15 minutes. Material properties and cell chemistry dictate the limits. Intercalation rate and diffusivity determine the speed of lithium-ion transport from the cathode to the anode side during charging. A large increase in the charge rate causes lithium plating at the anode, and consequently, the cell temperature rises, influencing battery lifetime, capacity, and safety. Various approaches have been suggested, such as implementing cell heating to enhance electrode kinetics. Nevertheless, there is a need for advanced innovations that enable rapid charging without compromising the battery's longevity or safety.

Life cycle - The life cycle is directly related to the number of driven kilometers until the battery is unsuitable to use. More specifically, the battery life can be defined as the time during which its capacity decreased to 80% of its initial capacity. To decrease the capacity loss, an insight into the degradation mechanisms is needed. Among them, the most common ones involve lithium-ion loss, lithium plating, growth of Solid Electrolyte Interface

(SEI), and volume change of electrodes. Thus, an appropriate selection of materials and optimization of operating conditions may extend the life cycle of the battery.

Cost - Although the operating cost of EVs is lower than those of ICE vehicles, the initial price of an EV is relatively high, mainly impacted by the battery cost. In order to boost the market of EVs, their price must be significantly reduced. It could be accomplished by the replacement of existing materials. For instance, because of its excellent thermal stability, cobalt is used in most cathode formulations. It is, however, one of the most costly battery materials. Substituting it with another compound could lower the battery price but also impact the safety and the cycle life. Therefore, there is a trade-off between the cost and the performance. Aside from the materials, the manufacturing process also considerably impacts the battery's price. The selection of a suitable fabrication method for line production and smart organization of operation procedures is, therefore, of great importance.

Safety - Because a battery failure might have catastrophic results, safety is one of the most significant aspects. Generally, before entering the market, batteries must undergo a series of tests, which are usually dictated by norms. Evaluations concern impact, thermal, vibration resistance, *etc.* Since commonly used liquid electrolytes are flammable and may cause an explosion, a solid electrolyte is preferred as a safer alternative.

Because of the constantly growing demand for LIBs, this technology attracted a lot of attention from both academia and industry. Their further improvements are possible and predicted characteristics are presented in Table 1.1.

It is forecasted that the energy density of LIBs will double its value by 2050. The charging time will be reduced below 10 minutes and the battery lifetime will be 2.5-5 times longer [7]. Therefore, considerable effort must be made to improve their performance. Researchers struggle to develop new strategies to help them achieve their objectives. Potential directions for the development relate to the use of novel materials for the fabrication of electrodes and the employment of a modern battery architecture directly associated with the fabrication methods.

These two strategies are the focus of this work and they are discussed in more detail in the following sections.

Table 1.1: Predicted performance characteristics of future LIBs. Data were taken from [7].

	Current (2020)	2030	2050
Gravimetric energy density at cell level (Wh kg^{-1})	160-260	275-320	>350
Volumetric energy density at cell level (Wh L^{-1})	450-730	750-900	>1000
Charging time (min) (20%-80% SOC*, 25°C)	15-30	10-15	<10
Battery lifetime (number of cycles for EV to 80% end-of-life capacity, 25°C)	*ca.* 1000	up to 2000	2500-5000

*SOC - State of charge - the amount of electricity remaining in the battery

Summary:

- Lithium-ion battery is the most common energy storage system in modern electric vehicles.
- Although lithium-ion batteries are already very advanced, further development is required before electric vehicles can compete with cars powered by internal combustion engines.
- Potential directions for the development of lithium-ion batteries relate to the use of novel materials for the fabrication of electrodes and the employment of a modern battery architecture.

1.2 Electrode materials for lithium-ion batteries

The development of rechargeable LIBs began in 1978 with the invention of intercalation electrodes by Stanley Whittingham [42]. The intercalation electrodes allowed for the reversible insertion of ions, atoms, or molecules between layers in a crystal lattice. He proposed an electrochemical cell composed of titanium disulfide and lithium metal as the electrodes ($Li/LiClO_4/TiS_2$) [43], and soon after Exxon company patented his invention. However, the commercialization turned out to be unsuccessful. The main problem was the alkali metal anode. While lithium anodes were used in primary batteries without any issues, rechargeable systems electrodes involve reversible accepting and releasing of lithium ions. Consequently, the metallic lithium regrows at the anode, creating dendrites and whiskers, which enlarge into the electrolyte. Once they reach the cathode, an unfortunate short circuit can occur [44].

John Bannister Goodenough and coworkers expanded Whittingham's research, inventing new cathode materials based on transition metal elements that crystallize in structures favorable to faster ions mobility. Consequently, in 1980 they elaborated [45] the $LiCoO_2$ layered structure, in 1986 [46], [47] the $LiMn_2O_4$ spinel structure, and in 1997 [48] the $LiFePO_4$ olivine's crystal system (Fig 1.6).

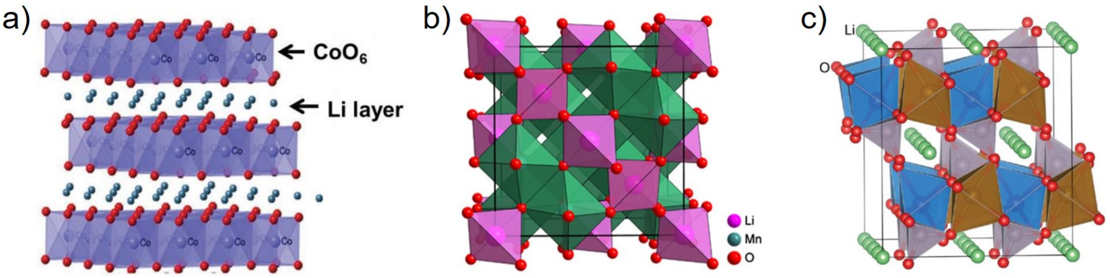

Figure 1.6: Crystal structure of: a) layered $LiCoO_2$ [49], b) spinel $LiMn_2O_4$ [50], c) olivine $LiFePO_4$ [51].

In the early 1980s, B. Scrosati and M. Lazzari proposed a new concept replacing the lithium electrode with another nonmetal intercalation electrode. Therefore, this new cell was built of two reversible electrodes, both capable of accepting and releasing lithium ions. Basically, in this electrochemical system, lithium ions *rock* from one side to another, hence its name *rocking chair batteries* [52], [53].

In 1985 [54], I. Kuribayashi and A. Yoshino filed patents for an electrochemical cell with $LiCoO_2$ cathode and an intercalation carbon anode. Soon after, in 1989 [55], Nishi *et al.* improved the performance of their cell, increasing the interlayer spacing of carbonaceous material of the anode. Based on their patent in 1991, Sony commercialized the first

Li-ion battery built of $LiCoO_2$ cathode and hard-carbon anode [56], [57]. Due to its high energy density, reliability, and long cycle life, it is used worldwide, predominantly in the portable electronics market [58].
Since then, many studies have been conducted to find new materials, that may improve the performance of rechargeable LIBs. The most promising candidates for the fabrication of electrodes are discussed in the following sections.

1.2.1 Cathode materials

As was already mentioned, Goodenough and coworkers found three classes of oxides, which constitute leading today's most popular cathode chemistries [59]. The focus is on layered oxides, as these materials were used for our study.
The materials of the first class - layered oxides - with the general formula $LiMO_2$ (M - a transition metal or a combination of transition metals) occurs in the hexagonal system R3m, in which Li and M ions alternate on the (111) planes and are surrounded by oxygen [60]. The most common transition metals used for layered oxide cathodes are cobalt, nickel, and manganese [61]. Nickel provides high capacity and ensures almost 80% of reversible extraction of Li ions [62]. The presence of cobalt in the lattice reduces ion mixing, which increases the rate capability and contributes to high power delivery and fast charging. As for manganese, it is responsible for safety, acting as a structural stabilizer [9], [63].
The first elaborated oxide cathode is the layered $LiCoO_2$ [45]. The considerable size difference between Li^+ and Co^{3+} cations results in fast lithium-ion diffusion and good electrical conductivity. Moreover, the presence of cobalt increases structural stability. $LiCoO_2$ oxide exhibits high performance voltage of 4 V, making it one of the best cathodes. However, its practical capacity is limited to 140 mAh/g, and when charging more than 50%, oxygen is extracted from the crystal lattice [59], [64], [65].
$LiNiO_2$ layered oxide as a cathode material is more favorable when considering the cost and the discharge capacity. However, this compound is difficult to synthesize because of its decomposition at high temperatures. Nevertheless, the electrochemical properties of $LiNiO_2$ are satisfying. The discharge capacity totals 200 mAh/g in the voltage range of 3.0 to 4.3 V [66], [67].
Since manganese is cheaper than cobalt and less toxic, $LiMnO_2$ was proposed as a layered oxide cathode for Li-ion batteries. Researchers were convinced that it is a noteworthy candidate with excellent electrochemical properties. However, its layered structure is rearranged during charge-discharge to the spinel-like configuration. Therefore, this compound could not find an application as a cathode [68], [69].

After years of working on the individual layer materials, a new type of oxide was discovered. It was realized that the synergistic effect of the Ni, Co, and Mn in layered materials could be advantageous [70], [71]. Ni-rich $LiNi_xCo_yMn_zO_2$ (NMC), offers higher capacity (nickel), higher rate capability (cobalt), and improved structural stability, ensuring safety (manganese) [9]. The cost associated with cobalt content in LIBs is a notable concern, which is directly related to the challenging mining process [72]. Therefore, low-cobalt, Ni-rich NMC became the most common cathode material for electric vehicles' batteries, chosen by many car manufacturers, for instance, Mitsubishi, Renault, Volkswagen, Nissan, Hyundai, Audi, Jaguar [8]. However, NMC suffers from structural and chemical instability, which causes a decline in cell performance over time [59]. Depending on the stoichiometric ratios of Ni, Mn, and Co atoms, it may have different characteristics [73].

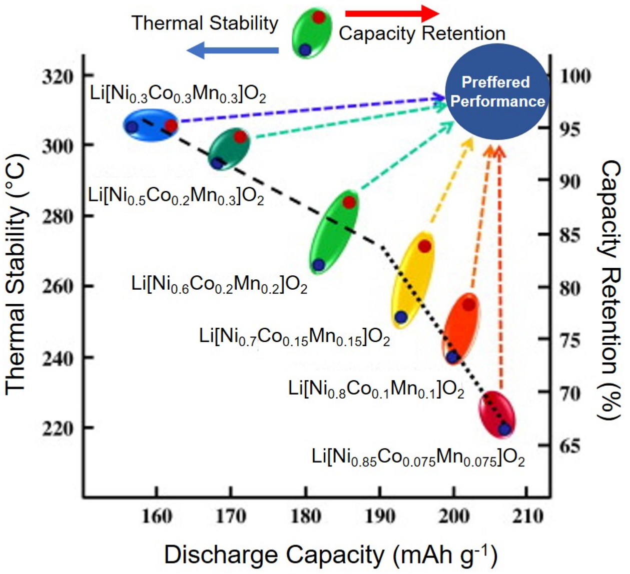

Figure 1.7: Link between discharge capacity, thermal stability, and capacity retention of NMC materials. Reproduced from [74].

As mentioned before, Ni offers high capacity so that a rich-nickel cathode could benefit the electrochemical performance, but at the same time, the thermal stability and ability retention deteriorate. NMC materials can deliver the specific capacity of around 200 mAh/g.

Figure 1.7 shows the relationship between the characteristics of different stoichiometric ratios of NMC materials. The plot clearly demonstrates the trade-off between capacity and safety. It seems unlikely that modifying the composition would be sufficient to create the perfect cathode material, which would have great capacity and excellent safety. Therefore, NMC needs to be specifically tailored for each application [74].

In our study, we used $LiNi_{0.3}Mn_{0.3}Co_{0.3}O_2$ (NMC333) and $LiNi_{0.6}Mn_{0.2}Co_{0.2}O_2$ (NMC622) for cathode fabrication. The details are presented in the further part of this work.

1.2.2 Anode materials

Because of the high theoretical capacity (3860 mAh/g), low density (0.59 g/cm^3), and lowest negative electrochemical potential (−3.04 V vs. the standard hydrogen electrode), lithium metal was considered one of the most promising anode materials for rechargeable batteries. However, the growth of Li dendrites and the low Coulombic Efficiency (CE) resulting in short cycle lifetime limited the application of Li metal anodes [75].

Since the commercialization of Li-ion batteries by Sony Corporation in 1991, graphite has been the most common anode material. Individual graphene sheets are held together by van der Waals forces to form a crystalline, layered structure. Its theoretical capacity as an anode in LIBs is 372 mAh/g. Despite many advantages, such as low cost, safety, easy handling, good cycling stability, *etc.*, many researchers focused on finding alternative materials with higher theoretical capacity, higher power density, and better electrode stability [76].

Among them, silicon (Si) is one of the most promising anode materials, and since, in this work, it is used for the fabrication of electrodes, it will be discussed in more detail. Except for the fact that Si is very cheap and abundant, it is characterized by the highest energy density known.

As observable on the equilibrium phase diagram (Figure 1.8), Si undergoes several phase transformations when Li is introduced into its structure at 450°C, resulting in a few voltage plateaus in the galvanostatic voltage curve. However, it is not the case for lithiation at room temperature, where only a single crystalline-to-amorphous conversion occurs [77].

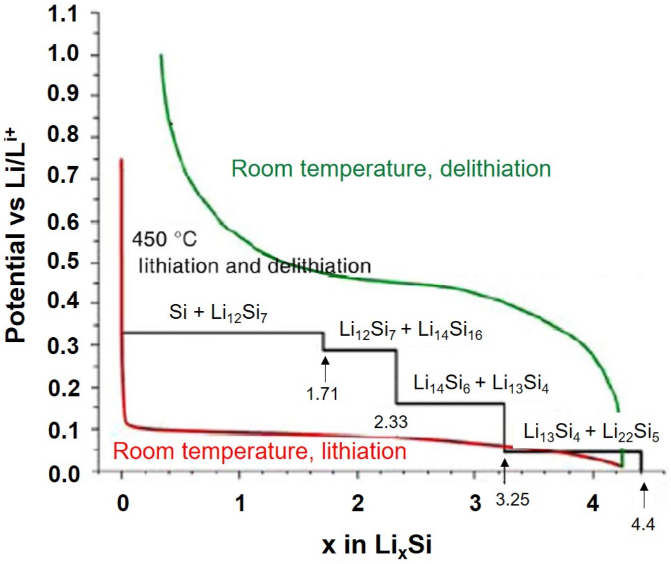

Figure 1.8: Galvanostatic lithiation/delithiation voltage curves of silicon at room temperature (red and green curves) and at 450°C (black curve). Reproduced from [77].

For $Li_{21}Si_5$, as the most lithium-rich structure, the theoretical specific energy density equals 4008 mAh/g. However, at room temperature, this phase is not observed and instead, the metastable $Li_{15}Si_4$ appears, showing the theoretical capacity of 3579 mAh/g [78].

Although Si anode offers excellent electrochemical properties, it suffers from a huge volume

expansion during the lithiation/delithiation process (up to 400%) [10]. The resulting stress and strain lead to the mechanical damage of the active material [79]–[81]. In accordance with research, three main mechanisms (Figure 1.9) of Si anode failure are identified:
1) During the Li–Si alloying/dealloying processes, the Si particles are subjected to cracking, and pulverization, resulting in the loss of electrical contact [77].
2) Significant morphological and volume changes are attributed to the charge/discharge process. During lithiation, Si particles swell and impinge on each other, and when Li ions are released, they contract, detaching from the conductive network. Additionally, the volume increase/decrease of the whole Si anode leads to the loss of contact with the current collector [12], [77].
3) During the charge/discharge cycle, SEI is created on the surface of Si particles as the electrolyte decomposition products. SEI layer serves as a barrier for further side reactions, which is crucial for the long cycle life of battery [82]. However, SEI can be destroyed during the Li disinsertion process when the volume of active material decreases. Consequently, the Si particle surface is re-exposed to the electrolyte forming thicker and thicker SEI upon the Li–Si alloying/dealloying cycle. As a result, SEI became detrimental, rather than favorable, continuously consuming the electrolyte, suppressing the electrical contact between Si particles and a current collector, weakening the electrochemical reactivity, and extending the Li-ions diffusion path [12], [83], [84].
These severe structural changes result in a low coulombic efficiency and rapid capacity decay [85].

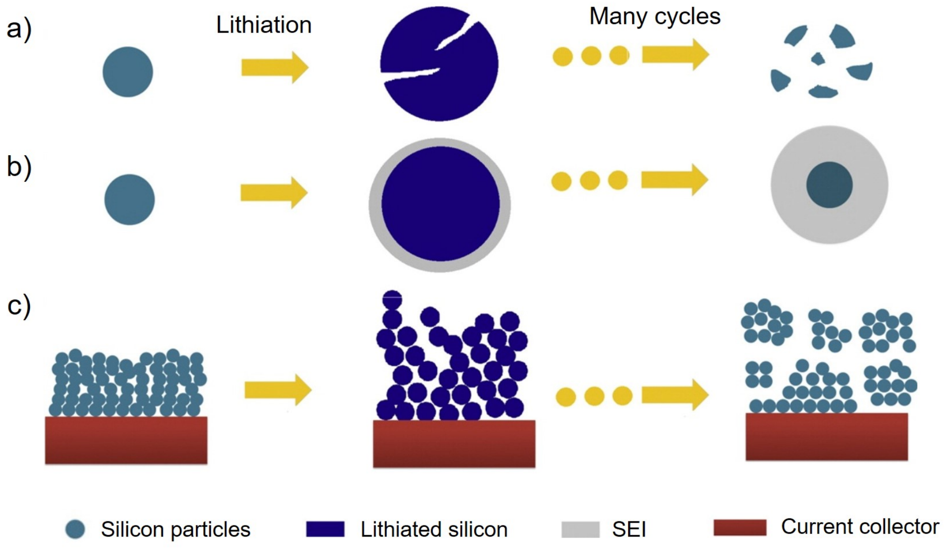

Figure 1.9: Mechanisms of Si anode damage: a) material pulverization, b) Morphology and volume change of the whole Si electrode, c) Instability of solid-electrolyte interphase (SEI). Reproduced from [77].

To overcome the issues related to this extremely large volume change, several strategies were proposed by researchers. It was reported that nanosized Si materials, such as Silicon Nanoparticles (SiNPs) [86]–[88], Silicon Nanowires (SiNWs)[89], [90], Silicon Nanotubes (SiNTs) [91], *etc.* can solve this problem. These nanostructured materials may sustain large volumetric deformations without mechanical fracture. Furthermore, their high surface areas benefit shorter ionic and electronic diffusion paths, improving the electrode kinetics. However, it was reported that due to the high surface energy, the nanoparticles merge during the insertion/extraction process, creating a thick block after a few cycles. The further electrochemical reactions are then impossible [92]. To prevent this direct contact between Si particles, the carbon-coated Si was proposed [93]–[95]. Apart from serving as the physical barrier impeding the aggregation of active material, the coating provides the following functions: improving the electron transport, accommodating the volume changes during the lithiation process, and preventing the direct contact of Si with electrolyte, thus limiting the SEI layer formation [96].

Another idea to accommodate the large volumetric changes is to fabricate an electrode with a special architecture [97], to use an amorphous silicon [98] or a porous structure of anode material [99], [100]. Furthermore, a suitable polymeric binder may also be very helpful in overcoming the problem of Si expansion [11].

In this work, a few strategies were adopted to overcome the issues of large volume changes. We have tested SiNPs and carbon-coated SiNPs as anode materials. Moreover, we tried to fabricate Three-Dimensional (3D) anode architectures, that may accommodate the structure expansion.

1.2.3 Electrode compositions

Composite materials applied for the fabrication of electrodes in LIBs should supply the ionic reactants and electrons to the surface of Active Electrode Material (AEM) particles. Therefore, they should have both electronic and Li$^+$ ionic conductivity [102], [103]. Electrodes usually consist of AEM, Conductive Agent (CA), and a binder, as shown in Figure 1.10. The combination of AEM and CA powders should ensure a mixed ionic and electric conductivity. A binder is necessary to obtain appropriate mechanical properties of deposited films, like toughness, compressibility, and tensile strength.

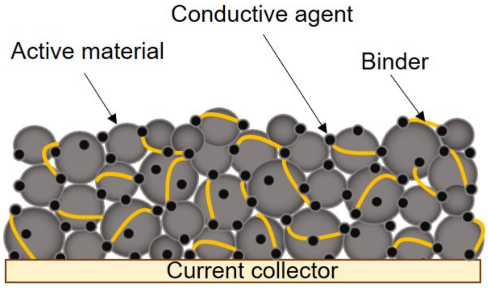

Figure 1.10: Schematic representation of a typical electrode structure [101].

Summary:

- One of the most promising material for the cathode of modern lithium-ion batteries is NMC, with the synergistic effect of Ni, Co, and Mn. However, NMC suffers from structural and chemical instability, which causes a decline in cell performance over time.
- Silicon is one of the most promising and most often used anode materials, but it suffers from a huge volume expansion during the lithiation/delithiation process (up to 400%), which may lead to the mechanical damage of the active material.
- To overcome the issues related to this extremely large volume change, several strategies may be employed, such as, the use of silicon nanoparticles or carbon-coated silicon, and fabrication of electrode with a special architecture.
- Electrodes of LIBs usually consist of AEM, CA, and a binder. AEM and CA powders must ensure a mixed ionic and electric conductivity, while binder is necessary to obtain appropriate mechanical properties of deposited films.

1.3 Battery architecture and fabrication methods

1.3.1 State-of-the-art of Li-ion battery manufacturing technology

The present state-of-the-art of Li-ion battery manufacturing technology, widely adopted at the industrial scale (Samsung SDI, CATL, LG Chem, Panasonic, and others), is divided into three major steps: electrode fabrication, cell assembly, and electrochemistry activation.

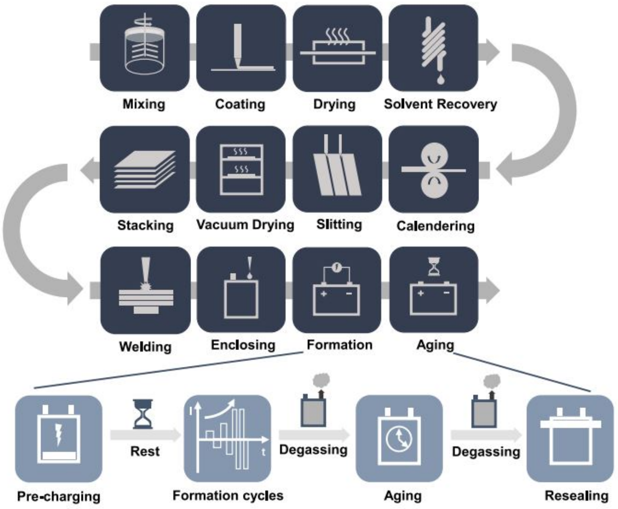

Figure 1.11: Typical process chain for Lithium-ion batteries [104].

Figure 1.11 depicts a typical battery process chain that uses the wet coating techniques for cell components deposition.

In the first step, a homogeneous slurry consisting of AEM, CA, binder, and solvent is formulated. Subsequently, the prepared suspension is deposited on the current collector (usually Al foil for the cathode and Cu foil for the anode) via one of the wet coating methods, such as slot die coating [105] or tape casting [106]. Then, during the dying step of the deposited films, a solvent is evaporated. Generally, the cathode slurry includes N-Methyl Pyrrolidone (NMP), which is able to dissolve the binder. However, this organic solvent is highly toxic and subjected to strict emissions regulations. Next, the calendaring process is implemented to improve the electrodes' energy density and physical properties (density, adhesion, conductivity, *etc.*). Afterward, the previously prepared components are slit to an appropriate dimension to suit the cell design. They are placed in the vacuum oven to remove the excess water. The cell assembly step starts with stacking electrodes and separators layer by layer. Next, the welding (most commonly ultrasonic welding) bonds the copper and aluminum tabs with current collectors. Thus prepared, the cell is placed in the designed enclosure, filled with electrolytes, and sealed. In the last step, the electrochemistry activation must be performed. The goal of this procedure is the formation of a stable solid-electrolyte interface (SEI) layer. To avoid the corrosion of the copper current collector, the cells are charged at the beginning to a relatively low voltage, which is followed by an interval for electrolyte wetting. The charging/discharging process is executed at a gradually increasing rate to form a stable SEI. After the formation process, the generated gas during cycling must be released. Then, the batteries are stored to complete electrolyte wetting and stabilize SEI. Before the final sealing, another degassing step must be applied. Afterward, the cells can be delivered to the end product manufacturers [104].

1.3.2 Battery architecture

Conventional laminated battery structure consists of alternately deposited layers of electrodes (see Figure 1.12). Although the fabrication process of such cells is relatively easy, there is a trade-off between the energy density and the power density [13]. More active material must be loaded to enhance the energy density, resulting in a thicker electrode. This, in consequence, limit the power density due to the slow diffusion of Li ions. Moreover, as the electrode expands and contracts while cycling, the mechanical integrity also declines with film thickness [107], [108].

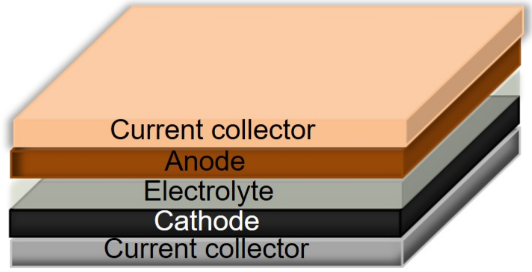

Figure 1.12: Schematic representation of conventional laminated battery structure.

On the contrary, 3D battery architecture allows the electrolyte to penetrate among active components, enhancing the surface-to-volume ratios and resulting in a shorter diffusion path of Li-ions. Increased loading of active material is possible without restricting ion diffusion. Therefore, 3D cells might have both a high energy density and a high power density. Additionally, high-capacity materials that undergo significant volumetric changes during cycling may be used [14].

The literature review shows the different 3D architectures, among which the most common are presented in Figure 1.13.

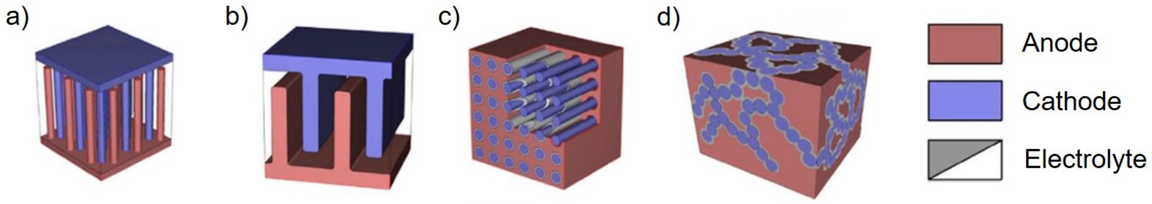

Figure 1.13: Different 3D battery structures: a) interdigitated rod electrodes, b) trench design, c) concentric architecture, d) sponge design [107].

The first proposed structure (Figure 1.13a) consists of alternating pillars of anode and cathode in the form of ordered arrays, separated by an electrolyte. The trench design

(Figure 1.13b) is quite similar, except that instead of pillars, it is composed of interdigitated plates. In the concentric architecture (Figure 1.13c), the electrolyte volume is reduced; thus, the energy density increases. A layer of electrolyte is coated on the rods of the cathode or anode, while the other electrode material fills the empty space. Another option is the sponge design (Figure 1.13d), which does not represent an ordered structure but is instead made up of a network of randomly oriented electrode materials that are then covered with an electrolyte. The other active material occupies the remaining space [107].

1.3.3 3D lithium-ion battery architecture

Some of the first studies on the fabrication of 3D battery architecture were done using a perforated substrate. Nathan *et al.* [109] fabricated a 3D microbattery based on a microchannel plate consisting of thousands of holes per square centimeter, increasing the surface area per given footprint (initial 2D substrate area) by more than an order of magnitude. Wet chemistry was used to sequentially deposit the films of Ni cathode current collector, a MoO_yS_z cathode, a Hybrid Polymer Electrolyte (HPE), and a lithiated graphite anode on all exposed surfaces of the substrate (Figure 1.14a). It was reported that the capacity of such a manufactured cell was roughly 30 times higher than that of a similarly constructed planar cell with the same footprint and cathode thickness.

Eustache *et al.* [110] designed a silicon microtube scaffold consisting of micropillars and microcontainers (Figure 1.14b). Subsequently, using the Atomic Layer Deposition (ATD) technique, Pt current collector and TiO_2 anode were deposited into the silicon structure. The surface capacity of the anode was $0.2\,mAh/cm^2$ at C/10, and the authors claimed that this was the highest value reported for a 3D TiO_2 negative electrode.

Some authors also reported self-supported 3D batteries fabricated by template synthesis, which uses the idea that the pores of host material may serve as a template for shaping a new product [107]. Li *et al.* [111] used the sol-gel template synthesis to prepare SnO_2 nanofibers. The template, made of microporous polycarbonate, was submerged in a tin oxide-based sol and then put on a Pt current collector. Subsequently, the polycarbonate was burnt in oxygen plasma. Finally, the electrode consisted of monodisperse SnO_2 nanofibers of 110 nm in diameter placed on a current collector like the bristles of a brush, which can be seen in Figure 1.14c. Authors reported extraordinary rate capabilities with a high life cycle (1400 cycles), which was superior to any electrodes of this type described previously.

Another interesting approach for the fabrication of 3D batteries is templating, in which a biological material is used as a template. Chen *et al.* [112] used Tobacco Mosaic Virus (TMV) to build a template on a stainless steel current collector. The virus has a cylindrical shape with an outer and inner diameter of 18 nm and 4 nm, respectively, and is 300 nm long. The virus was genetically modified so that self-assembly onto different surfaces is possible, and it may be metal coated in electroless plating solutions. In the study, the virus was vertically aligned on the current collector and subsequently covered by Ni (electroless plating) and Si (Physical Vapor Deposition (PVD)). TEM image (Figure 1.14d) shows the layers of Ni and Si deposited on the virus rod. Such fabricated silicon anode exhibits a high capacity of 3300 mAh/g and excellent cycling stability (0.20% loss per cycle at 1C). A colloidal system template can be used to manufacture battery cells with ordered porosity. First, the voids between closed-packed spheres are filled with the target material. Subsequently, the spheres are removed, and the negative replica of the initial structure, commonly named "inverse opals," is created [113]. Liu *et al.* [114] formed a colloidal template from Polystyrene (PS) and filled the interstitial space by electrodeposition of Ni. After removing the PS, Si was deposited on the Ni inverse opal (see Figure 1.14e). The authors demonstrated that this 3D architecture resulted in lower interfacial resistance and higher Li ion diffusion coefficient, enhancing the battery performance.

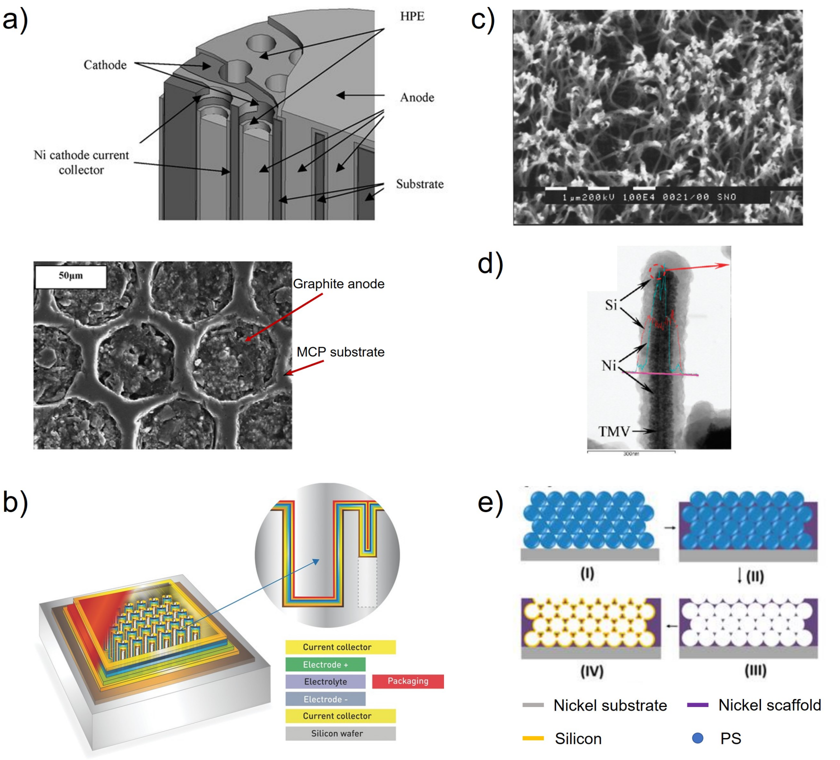

Figure 1.14: Examples of 3D lithium-ion battery architectures: a) 3D microbattery done using a perforated substrate [109], b) 3D battery based on a silicon scaffold [110], c) template-synthesized SnO_2 anode [111], d) silicon anode fabricated by deposition of Ni and Si layers on the virus rod [112], e) schematic representation of the fabrication of electrodeposited Si-on-Ni inverse opal structure for lithium-ion microbattery by colloidal crystal template method [114].

Although all the above-mentioned studies proved that 3D battery structures are beneficial for electrochemical performance, fabrication techniques are complicated and time-consuming, compared to the conventional manufacturing process. Fast manufacturing methods that may be easily implemented at the industrial scale are needed to reduce batteries' costs and allow for mass production.

A step forward in the fabrication of 3D structures for LIBs was the implementation of Additive Manufacturing (AM) technologies, which refer to a wide range of methods that build an object layer by layer directly from a Computer-Aided Design (CAD) model [115]. According to ASTM F2792 Standards, AM techniques are divided into the following categories: 1) vat photopolymerization (*e.g.*, SLA), 2) powder bed fusion (*e.g.*, Selective Laser Sintering (SLS)), 3) binder jetting, 4) material jetting (*e.g.*, IJP, Aerosol Jet Printing (AJP)), 5) sheet lamination (*e.g.*, Selective Deposition Lamination (SDL), 6) material extrusion (*e.g.*, FFF, FDM), 7) directed energy deposition (*e.g.*, Laser Metal Deposition (LMD)) [116]. Compared to conventional manufacturing methods, AM enables the fabrication of geometrically complex structures with minimal material waste [23]. A thorough discussion on the various AM technologies for the fabrication of batteries can be found in reviews [117], [118].

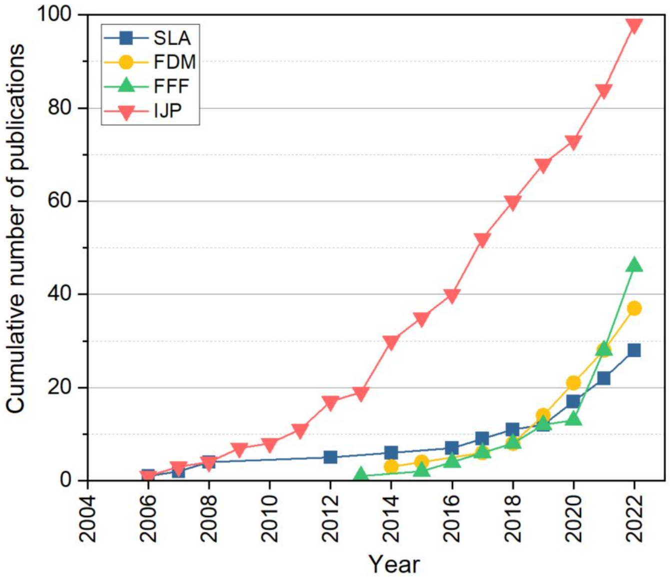

Figure 1.15: Cumulative number of publications devoted to the fabrication of LIBs by SLA, FDM, FFF, and IJP. Analysis was performed using the Scopus database (Elsevier).

FFF, FDM, SLA and IJP were found particularly promising for LIBs manufacturing [23].

The plot in Figure 1.15 shows the cumulative number of publications devoted to the fabrication of LIBs using each of these techniques. The analysis was performed using the Scopus database (Elsevier). Reviews and book chapters were excluded from the search to focus on the experimental research done on the subjects. The interest in AM in the fields of LIBs began at the beginning of the 21st century and since then, has been continuously increasing, particularly in the case of IJP. By 2022, only around 30-50 publications were reported for FFF, FDM, SLA techniques, whereas for IJP, it reached nearly 100. Nevertheless, the overall quantity of published papers throughout the years is not extensive.

Presented below are a few examples of studies using AM for battery production.

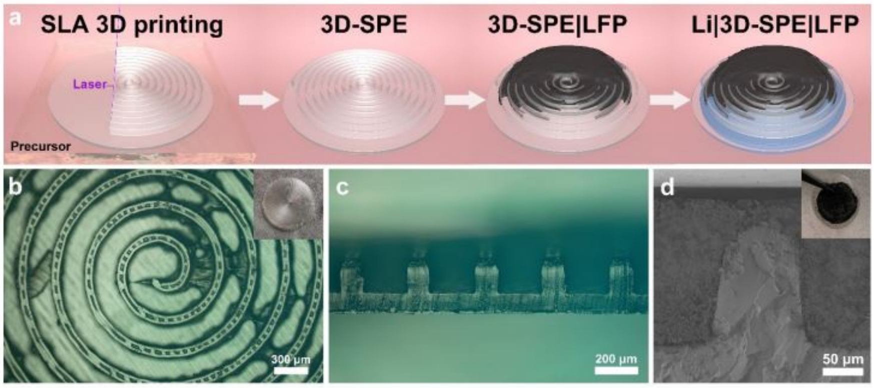

Figure 1.16: 3D-SPE fabricated by stereolithography: a) schematic representation of cell manufacturing process, b) top view of 3D-SPE, c) cross-section of 3D-SPE, d) interface between printed 3D electrolyte and cathode [17].

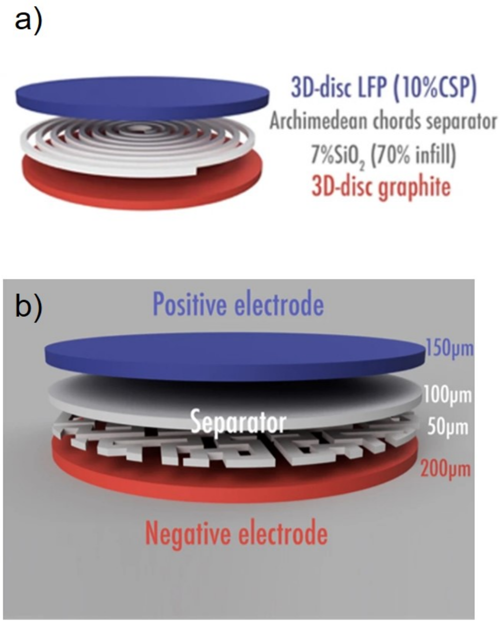

Figure 1.17: Schematic representations of cells manufactured by FDM: a) Archimedean chords as separator layer, b) Hilbert curves pattern as separator layer [16].

He *et al.* [17] fabricated a three-dimensional solid polymer electrolyte 3D-SPE using SLA. Poly(ethylene oxide) (PEO) polymer was used as the electrolyte material. After printing, the cathode slurry with $LiFePO_4$ (LFP) as an active material was tape-casted onto 3D-SPE, and lithium foil was used as an anode. The preparation process of a cell and images of printed electrolyte are presented in Figure 1.16.

For the sake of comparison, cells with structure-free electrolytes were also prepared. The 3D architecture provided high active material mass loading, resulting in a higher specific capacity compared to the layered structure. Moreover, greater capacity retention was achieved. The authors claimed that the enhanced performance was due to a reduced Li-ion transport pathway from the electrolyte to the electrode, and improved interfacial adhesion during cycling.

Maurel *et al.* [16] employed FDM to print in one-shot complete LFP/Graphite battery cells with a 3D separator. They tested different designs, claiming that Archimedean chords and Hilbert curves pattern as separator layers are advantageous in terms of electrochemical performance. Figure 1.17 presents schematic representations of such manufactured cells. Interdigitated battery structures consisting of $Li_4Ti_5O_{12}$ (LTO) anode and LFP cathode (Figure 1.18) were built by FFF, commonly known as Direct Ink Writing (DIW). Excellent performance outcomes were achieved due to high aspect ratios of electrodes with a small area footprint [119].

While the interest in IJP for battery production is the highest among additive manufacturing (AM) techniques, to the best of our knowledge, no previous research has presented 3D structures of LIBs built using this method. IJP, the main subject of this work, is discussed in detail in the following section.

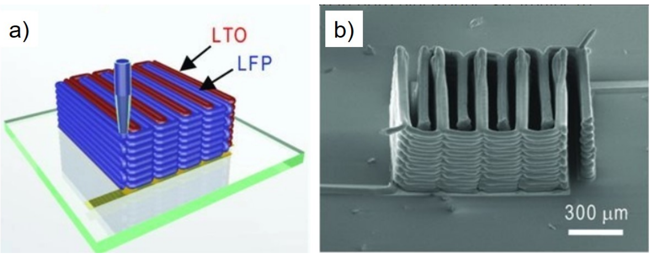

Figure 1.18: a) Schematic representation of 3D interdigitated battery architecture, b) SEM image of printed and annealed interdigitated electrodes [119].

Summary:

- Conventional laminated battery structure experiences a trade-off between energy density and power density. On the contrary, 3D battery architecture allows the electrolyte to penetrate among active components, enhancing the surface-to-volume ratios and resulting in a shorter diffusion path of Li-ions. Therefore, 3D cells might have both a high energy density and a high power density.
- Although there exists a considerable body of literature proving that 3D battery structures are beneficial for electrochemical performance, fabrication techniques are complicated and time-consuming compared to the conventional manufacturing process.
- A step forward in the fabrication of 3D structures for LIBs was the implementation of additive manufacturing technologies.
- Fused filament fabrication, fused deposition modeling, stereolithography, and inkjet printing were found particularly promising for LIBs manufacturing.
- Although the interest of inkjet printing for battery production is the biggest among additive manufacturing techniques, no previous research presented 3D LIBs structures built by this method.

1.4 Inkjet printing

1.4.1 Inkjet printing technology

Inkjet printing is a method of microfabrication that builds objects by the precise deposition of individual, tiny droplets of ink on the specified area of a substrate [120].

The graphic market is doubtlessly the largest application of IJP [121]. However, it was also successfully applied to printed electronic devices, such as thin-film transistors, battery electrodes, supercapacitors, sensors and detectors, solar cells, light-emitting devices [122]–[126]. Over the last decade, owing to numerous advantages, this technology came into prominence in the industrial domain [127]. Since the printed pattern is generated from a digital image, there are limitless design possibilities with the ability of quick modification to another configuration. Consequently, inkjet printing is considered a flexible method with a very low outlay for the design process. The deposited volume of ink is precisely controlled, which decreases the waste of feedstock materials [128]. Moreover, tiny droplets ensure a great resolution of printed objects [129]. Another significant convenience is a noncontact method of deposition. Due to that, there is no limitation when choosing a substrate type. Multi-material and multilayer printing designs are also feasible [130]. However, despite all the advantages, IJP has also some drawbacks.

The major challenge is nozzle clogging caused by insoluble particles of ink. During printing, they often tend to agglomerate, inhibiting the further process. Another difficulty is the complex drying behavior, which influences printed films' uniformity. Consequently, one of the most challenging tasks for researchers is developing a suitable ink [120], and it is discussed in the further part of the work.

Inkjet printing can be divided into two main categories: continuous and drop-on-demand, which are discussed below.

Continuous Inkjet (CIJ) printing

Figure 1.19 schematically represents the continuous inkjet printing system. A high-pressure pump continuously pushes fluid from a reservoir to a nozzle, where a piezoelectric crystal creates an acoustic wave. Under the surface tension forces, the liquid stream breaks into small droplets at regular intervals. Afterward, they are selectively charged by an electrode. The uncharged drops create a pattern on a substrate, while the charged drops are directed into a gutter to be returned to the ink reservoir [131], [132].

The high deposition speed of CIJ printing makes it extremely valuable in industrial applications. Additionally, the continuous flow of liquid in CIJ helps prevent nozzle clogging. However, this method also has drawbacks, such as a decline in resolution due to the fast printing speed.

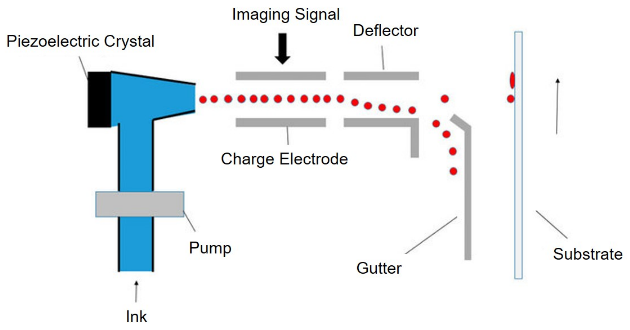

Figure 1.19: Schematic diagram of continuous inkjet printing [133].

The cost of the printer is relatively high due to the need for additional systems for recycling, drop selection, and so on. Furthermore, the CIJ system is not versatile as it can only work with inks that can be electrically charged [134].

Drop on Demand (DOD) inkjet printing

Unlike the CIJ method, the DOD process selectively ejects droplets using pressure pulses only when required. These droplets are propelled in a direct path to precise locations on the substrate. Consequently, the printhead must be positioned as close as possible to the printer's table to achieve high-quality prints [131].

Depending on the mechanism of pressure pulse generation, DOD printing can be divided into four main categories: thermal, piezoelectric, electrostatic, and acoustic [120]. The operating principles of these systems are schematically represented in Figure 1.20.

Thermal inkjet printing system generates drops by heating a resistive element installed in a reservoir containing ink. The temperature of this element reaches 350-400°C, which causes the evaporation of a thin film of ink touching the heater. It promptly creates a bubble and, consecutively, a pressure pulse that pushes a drop of ink through the nozzle. The resulting void is subsequently refilled, and the process repeats [135]. An advantage of thermal inkjet printing is the ability to generate small drop sizes (150 to 200 picoliters) [134]. Nonetheless, this system is limited to thermally stable and vaporizable inks. When evaporation does not occur, fluid can cause a formation of the coating on the resistive element, which consequently deteriorates its efficiency and eventually reduces the lifetime of the printhead.

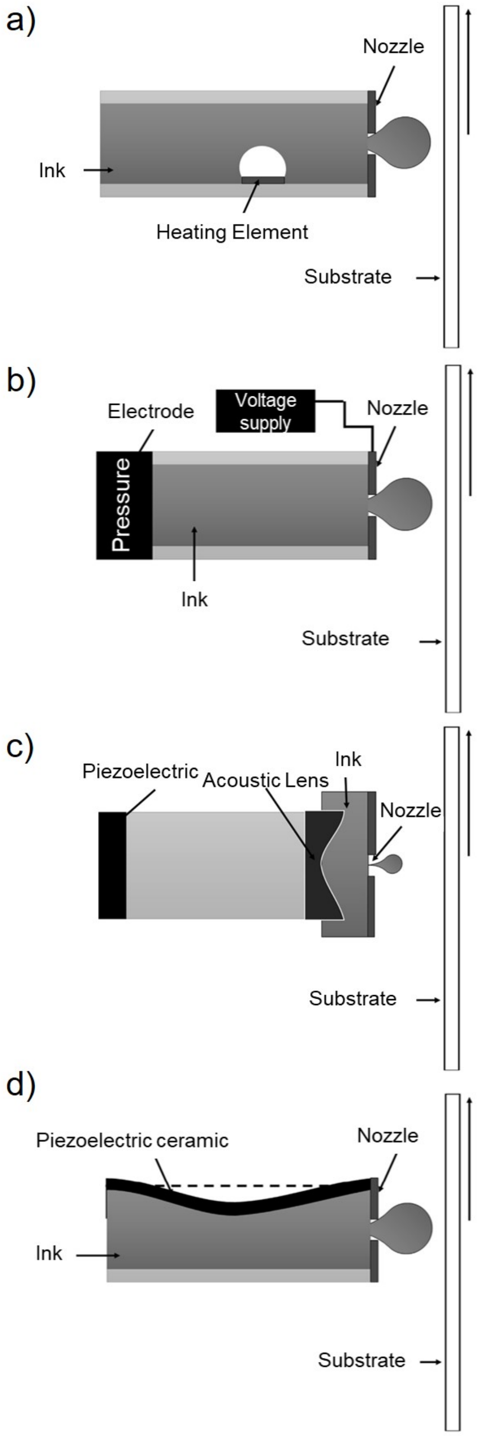

Figure 1.20: Schematic illustration of four main DOD printing systems: a) thermal inkjet printing, b) electrostatic inkjet printing, c) acoustic inkjet printing, d) piezoelectric inkjet printing [120].

The key advantage of **electrostatic inkjet printing** is the high resolution of printed patterns. The ejection of drops is achieved by electrostatic forces applied between the nozzle and an electrode, which attract free charges within the ink, detaching fluid from the printhead in the form of fine droplets. In this method, the size of droplets is not restrained by the nozzle diameter, and more viscous inks can be used. However, only conductive slurries can be employed with this technique [120].

Acoustic inkjet printing uses acoustic energy for droplet generation. The ultrasound beam is focused onto the fluid surface, ejecting drops. This technology has a relatively low risk of nozzle clogging, and the droplet size can be easily controlled with high precision by varying the focal spot diameter. However, the printing speed is limited compared to other technologies [120].

Piezoelectric inkjet printing allows for the deposition of a variety of inks. It is considered the preferred method for most applications in printing functional materials [136]. In this technology, a pressure pulse is created mechanically by distortion of a piezo-crystal when an electric field is applied. This pulse causes the generation of droplets, which have volumes typically in the range of 1-1000 pL, yielding a high resolution of printed patterns [22], [129].

Since the ejection is executed by piezo-ceramic distortion, there is no restriction related to the thermal and electrical properties of inks. Moreover, the drop generation process can be relatively easily controlled by modifying the actuation pulse [137], [138]. A DOD inkjet printer, for instance, can print at a speed of 500 mm/s with a resolution of 5 µm x 5 µm [139]. In our study, the selection of DOD piezoelectric IJP for the fabrication of LIBs' electrodes was based on its numerous advantages over competing technologies. It provides high accuracy and precise control over droplet placement. This is crucial for creating well-defined electrode patterns with intricate designs and fine features. Piezoelectric inkjet printers are compatible with a wide range of inks, including conductive inks and nanoparticle suspensions. This versatility allows for the deposition of various materials, such as electrode active materials, binders, conductive additives, and electrolytes. It enables the fabrication of customized electrode compositions, opening possibilities for novel electrode designs and material combinations to enhance battery performance. Piezoelectric inkjet printers offer scalability for both lab-scale research and large-scale production. Moreover, their high printing speed makes them well-suited for industrial implementation.

1.4.2 Inkjet printing for lithium-ion batteries

Although IJP was highlighted as a promising technology for the fabrication of 3D designs [140], [141] and thin films [142] for LIBs, only a few studies have been done on the subject. Table 1.2 summarizes the publications, highlighting the most pertinent information.

The first reports on the application of the IJP to lithium-ion batteries were published by Shanghai Key Laboratory of Molecular Catalysis and Innovative Materials in 2006 [143], 2008 [144] and 2009 [124]. They described the preparation process of SnO_2, $Li_4Ti_5O_{12}$ and $LiCoO_2$ inks, proposing ball milling and/or ultrasonic bath for homogenizing, all done in the correct sequence. Printing was successfully performed with the Canon BC-03 cartridge, but the authors did not provide any information concerning the ink requirements and properties (viscosity, surface tension, stability, *etc.*).

In 2015, Gu *et al.* [145] used the IJP process to fabricate $LiFePO_4$ cathode thin films. The ink was prepared by bath sonication, and prior to printing, it was centrifuged to eliminate the possible large particles. The viscosity was set to 13 mPa.s, the recommended setting for the Dimatix-2800 printer. The electrochemical performance of inkjet-printed cathode layers was compared to those deposited by the tape casting method, with higher capacities obtained for the latter. However, since the formulation of a paste for doctor blading was different compared to the ink, the results should not be indicative. The same year, Dellanoy *et al.* presented the possibilities of printing $LiFePO_4$ cathode [146] and a silica-based ionogel electrolyte [147]. For the cathode fabrication, they used a piezoelectric inkjet printer specifically designed for R&D with the following ink requirements: viscosity 10-12 mPa.s, surface tension 28-33 mN/m, particle size <200 nm. Three formulations with different additives were tested: with Poly-Acrylic-co-Maleic Acid (PAMA), with Carboxymethyl Cellulose (CMC), with CMC + Triton X-100, prepared by magnetic stirring and ball milling. Basic rheological measurements were performed, verifying viscosity and stability at rest (storage modulus and shear modulus). Printability tests revealed that inks containing CMC could not be ejected.

The ink with PAMA was printable, possibly due to its low viscosity at the high shear rate and high stability. However, it is a probable assumption, and a more thorough examination is needed to understand the link between printability and rheological properties. Furthermore, PAMA has a lower molecular mass than CMC, which may significantly impact ink processability. The inkjet printed electrode exhibits excellent cyclability and very high rate charge/discharge behavior. For the printing of the electrolyte, Dimatix DMP2800 ink-jet printer was used. While the viscosity of the ionogel was measured, no other properties of the ink were provided. The inkjet printed electrolyte was tested with a full lithium-ion cell, demonstrating competitive performance compared to those based on expensive PVD processes.

Lawes used HP Deskjet 2540 inkjet printer for the deposition of TiO_2 [148] and Si [149] anodes. For both materials ink was prepared by sonication, and viscosity was adjusted to 10 mPa.s, which the printer manufacturer recommends. Three kinds of binders were tested for TiO_2 electrode formulation: Polyvinylidene Fluoride (PVDF), Polyvinylpyrrolidone (PVP), and Poly(3,4-ethylenedioxythiophene) Polystyrene Sulfonate (PEDOT:PSS), and only the latter was printable. Slurries prepared with PVDF and PVP were agglomerated and clogged the nozzle. PEDOT:PSS, PVP, CMC, and Na-alginate were used as binders for the preparation of Si anode. It was reported that each ink was sufficiently well dispersed and printable. However, anodes with PEDOT:PSS showed the highest stability due to their electrical conductivity and reversible deformation during electrode cycling.

Maximov *et al.* [150] fabricated NMC cathode using the IJP. Ink was dispersed by an ultrasonic bath, and large agglomerates were eliminated by centrifugation. They used NMP, the most common solvent for cathode fabrication in the battery industry. As for the rheological properties of prepared inks, authors adjusted the viscosity and surface tension according to the printer's requirements, *i.e.*, 8-10 mPa.s, and 28-32 mN/m, respectively. They studied the influence of different additives (ethylene glycol, diethylene glycol, propylene glycol) on the slurry characteristics. The stability was evaluated by the ζ-potential measurement.

Table 1.2: Components of LIBs fabricated by the IJP method. Reproduced from [101].

Active material		Solvent	Additives	Printer	Printed layer thickness	Electrochemical performance of printed structure	Ref.
Cathode	$LiCoO_2$	DI-water	CMC, commercial surfactant solution	Canon BJC-1000sp	1.2 µm (30 layers)	120 mAh/g at 180 $\mu A/cm^2$, 95% capacity retention after 100 cycles	[144]
	$LiFePO_4$	buffer solution (HCl + NaOH)	CMC, TritonX-100, glycerin	Dimatix-2800	20 µm	129.9 mAh/g at 0.1C (Al foil), 151.3 mAh/g at 0.1C (CNT)	[145]
	$LiFePO_4$	DI-water	PAMA	piezoelectric ink-jet printer	4 µm (40 layers)	80mAh/g at 9C, 70mAh/g at 90C	[146]
	LMNCO	NMP	PVDF, surfactant	Dimatix-2831	11.5 µm (25 layers)	240mAh/g at 0.01C	[151]
	1.20 NCM/ 1.25 NCM	NMP	PVDF, ethylene glycol, diethylene glycol, propylene glycol	Dimatix-2831	-	-	[150]
	V_2O_5/MXene	-	-	Dimatix-2800	-	321mAh/g at 1C, 91.8% capacity retention after 680 cycles	[152]
Anode	SnO_2	DI-water/absolute ethanol/diethylene glycol/ triethanolamine/ isopropylalcohol	CMC, CH10B, CH12B	Canon BJC-1000sp	2.3 µm (10 layers)	812.7mAh/g at 33 µA/cm^2	[143]
	$Li_4Ti_5O_{12}$	aqueous solution (LDS+Li-PAA)	PVP	Flat-bed Breva thermal inkjet	3.3 µm (20 layers)	128mAh/g at 0.5C	[153]
	Si	DI-water	PEDOT:PSS, PVP, CMC, sodium alginate	HP Deskjet 2540	1 µm (25 layers)	>1700mAh/g for 100 cycles, capacity retention of over 1000 cycles at 1000mAh/g	[148]
	Graphene	ethanol and terpineol	-	Jetlab-4	268nm (8 layers)	942mAh/g at 0.1C, 87% capacity retention after 100 cycles	[154]
	TiO_2	DI-water	PEDOT:PSS/ PVP/ PVDF	HP Deskjet 2540	3.02 µm (25 layers)	180mAh/g at 0.1C	[149]
	$Li_4Ti_5O_{12}$	DI-water/absolute ethanol/diethylene glycol/	CMC, CH10B, CH12B	Canon 1000SP	1.7-1.8 µm (10 layers)	174mAh/g at 10.4 $\mu A/cm^2$, 88% capacity retention after 300 cycles	[124]
Electrolyte	Ionogel	-	-	Dimatix-2800	5 µm (4 layers)	60mAh/g at 0.1C for $LiFePO_4$/ionogel/$Li_4Ti_5O_{12}$ full cell	[147]

Abbreviations utilized in the table: CMC - carboxymethyl cellulose; CNT - carbon nanotube paper; DI-water – deionized water; LDS - lithium dodecyl sulfate; Li-PAA - lithium polyacrylate; LMNCO - $Li_{1.15}K_{0.05}Mn_{0.54}Ni_{0.13}Co_{0.13}O_2$; 1.20 NCM - $Li_{1.2}Mn_{0.54}Ni_{0.13}Co_{0.13}O_2$; 1.25 NCM - $Li_{1.25}Mn_{0.54}Ni_{0.13}Co_{0.13}O_2$; NMP - N-methyl pyrrolidinone; PAMA - poly-acrylic-co-maleic acid; PEDOT:PSS - poly(3,4-ethylenedioxythiophene) polystyrene sulfonate; PVDF - polyvinylidene fluoride; PVP - polyvinylpyrrolidone.

Although the authors determined the optimal printing conditions, they did not present any results for the inkjet printed layers.

Kolchanov *et al.* [151] formulated NMC-based cathode inks, optimizing the rheological properties for the IJP: viscosity, surface tension, and contact angle. The concentration of dispersing agent was adjusted, and the sedimental stability was studied using centrifugation. Printability tests revealed that a stable drop might be generated, and a cathode thin film was fabricated. Its electrochemical performance was compared with the electrode deposited by the tape casting method, resulting in similar values.

Kushwaha *et al.* [154] showed the possibility of inkjet printing of a graphene film as an anode for lithium-ion batteries. In the article, it is mentioned that the stability and viscosity of ink are critical for printability, but studies on the rheological properties are not comprehensive enough.

Viviani *et al.* [153] investigated the effect of carbon additives on the electrochemical performance of inkjet-printed $Li_4Ti_5O_{12}$ anodes, fabricating them using a thermal inkjet printer. The rheological measurements were performed to confirm the suitability of slurries for the process. Furthermore, the electrodes manufactured with the Carbon Nanotubes (CNTs) as a conductive agent showed the highest specific capacity among all printed films, demonstrating that CNTs improving electrochemical performances may be applied to the IJP method.

Wang *et al.* [152] fabricated V_2O_5/MXene heterostructure cathode for lithium-ion batteries using the IJP. The prepared inks were printable, but the authors did not provide information concerning their properties. Nevertheless, the printed cathode layers exhibited excellent electrochemical performance, offering new possibilities for two-dimensional heterostructures in high-performance batteries.

Although the rheological properties of slurries are crucial in determining the printability of inks, the previous studies present either only basic rheological measurements, or the characteristics of the fluids are completely omitted. Furthermore, inks used to fabricate LIBs are very complex, and their flow behavior greatly impacts processability. Therefore, a more in-depth examination is needed to understand the relationship between rheology and printability. Moreover, the work done on the topic focuses exclusively on the printing of thin films, and as far as we know, no previous research investigated the inkjet printing of 3D structures for LIBs.

Summary:

- Inkjet printing is an advanced printing process in which tiny droplets of functional inks are deposited on a substrate. The key advantage of this technique is the ability of the fabrication of complex patterns with very high precision.
- In this work, DOD piezoelectric IJP was used for the fabrication of LIBs' electrodes, as it offers many advantages over competing technologies, such as high accuracy and precise control over droplet placement, compatibility with a wide range of inks, scalability for both lab-scale research and large-scale production, high printing speed, and many others.
- Although inkjet printing was highlighted as a promising technology for the fabrication of 3D designs and thin films for LIBs, only a few studies have been done on the subject. Moreover, the work done on the topic focuses exclusively on the printing of thin films, and as far as we know, no previous research investigated the inkjet printing of 3D structures for LIBs.
- The rheological properties of slurries are crucial in determining the printability of inks. A more in-depth examination is needed to understand the relationship between rheology and printability.

1.5 Ink formulation

As already mentioned in Section 1.2.3 (page 38), electrodes usually consists of AEM, CA, and a binder. To produce an ink that is stable and suitable for IJP, the incorporation of an appropriate solvent and dispersing agents is necessary [155], [156].

The performance of LIBs is greatly influenced by the distribution of components within the electrode. To achieve the connectivity, AEMs and CAs should be evenly distributed with minimal agglomeration and uniformly covered by a binder. Furthermore, strong adhesion between the electrode and the current collector is necessary [157]. Therefore, slurry preparation is crucial in fabricating composite electrodes [158].

This is especially true in inkjet printing technology, where a variety of factors can influence the drop ejection process. The particular nature of ink dictates the parameters of printing. However, ejection is sometimes impossible for various reasons, including rheological characteristics, particle size, and so on. The subsequent sections address these points and provide further details on the topics.

1.5.1 Ink formulation - requirements

In order to successfully deposit the desired pattern, a stable suspension with defined properties specified for the printer must be formulated. The rheology of the ink is an essential aspect to consider since it determines whether a drop can be ejected, and how the fluid behaves once it exits the nozzle. Wolfgang von Ohnesorge demonstrated the significance of viscosity, surface tension, and fluid inertia in predicting the flow's behavior [159]. Taking into account the Reynolds (Re) (the ratio of inertial forces to viscous forces) and the Weber (We) (the ratio of inertial forces to surface tension forces) numbers, he introduced a new dimensionless group – the Ohnesorge number (Oh) (the ratio of viscous forces to surface tension forces), which defines the boundaries of the various operating regimes for the problem of jet breakup:

$$Re = \frac{\upsilon \rho a}{\eta} \tag{1.1}$$

$$We = \frac{\upsilon^2 \rho a}{\gamma} \tag{1.2}$$

$$Oh = \frac{\sqrt{We}}{Re} \tag{1.3}$$

where υ, ρ and a are the velocity, density and characteristic length respectively, η is the dynamic viscosity and γ is the surface tension.

Fromm [160] identified the variable $Z = 1/Oh$ as a simple method for estimating the printability of ink, assuming that a stable drop is generated when $Z > 2$. Reis and Derby developed this concept via numerical simulations [161] and suggested the range $1 < Z < 10$ for printable ink, which is commonly recognized in most commercial DOD printing systems [21]. However, wider ranges of printability were also reported [162], implying that this criterion is not pertinent.

In general, when Z is too low, the viscous forces prevent the drop generation, whereas, at high values, satellite droplet formation occurs. There are, however, other aspects to consider while ejecting a drop. Duineveld *et al.* [163] claimed that there is a minimum velocity that yields enough energy to overcome the surface tension forces of a liquid to form a drop, and accordingly, printing is possible when the We number is greater than 4. The impact of the drop on the substrate is another important factor to consider. A single isolated droplet should be placed without secondary droplets around. Stowe and Hadfield [164] combined We and Re values and showed that when $We^{1/2}Re^{1/4}$ is larger than 50, splashing occurs. The zone within this parameter space, where stable drops without satellites can be deposited on a substrate without splashing, is represented in Figure 1.21. However, the Ohnesorge number is unambiguously determined for simple Newtonian fluids, for which liquid properties do not depend on flow conditions. The great majority of functional inks used for the fabrication of LIBs display non-Newtonian properties. Shear-thinning behavior occurs in most concentrated suspensions [165], and with the addition of a polymeric binder, viscoelasticity may be observed, changing the drop generation characteristics [166]. The flow behavior of inks is influenced by various factors, such as concentration of solid fraction, particle size and shape, kind of added dispersing agent or lack thereof, type of used solvent, architecture,

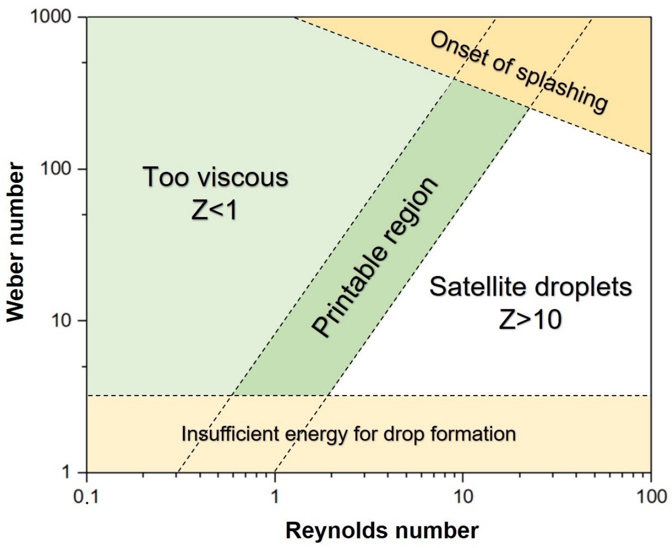

Figure 1.21: A parametric space for successful DOD printing defined by axes of Reynolds and Weber numbers. Reproduced from [137].

molecular weight, and concentration of the binder [167].

Since DOD printing is a precise deposition method, the objective is to optimize the process parameters so that a single drop traveling straight to the substrate is formed (Figure 1.22a). In an ideal scenario of the ejection process, the fluid flows out from the nozzle, forming the main drop with an attached filament. After the filament breaks up, the tail end becomes rounded and speeds up, merging with the main drop into single droplets [168].

Bienia *et al.* [169] demonstrated that despite the similar properties, the drop generation behavior is different for every ink, reflecting the potential impact of their particulate nature. Furthermore, although complex inks are sometimes adapted in terms of viscosity, surface tension, and stability, the ejection is still unsuccessful. For instance, the viscoelastic effect may cause the loss of axisymmetry during the ejection (Figure 1.22b), resulting in poor jetting quality.

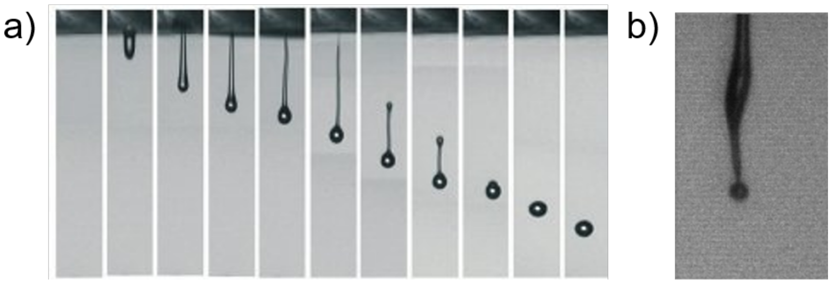

Figure 1.22: a) Ideal scenario of the droplet ejection process [134], b) Image showing the behavior of a viscoelastic ink (PVA, 25 wt% in water) after exiting the nozzle [169].

A universal window that can be used to forecast fluid behavior during printing does not exist, and each formulation should be considered individually.

Another thing to consider is the particle size of constituted powders. Some authors [170], [171] reported that the nozzle diameter should be 50 times greater than the particle size. Others [172], [173] claimed that the ratio between the nozzle diameter and the particle size must be at least 100:1. Otherwise, the nozzle may be clogged, inhibiting the printing process. Since the nozzle orifice for commercial printheads is typically between 22 and 50µm [174], the particle size should be in the sub-micron range. Moreover, the particles must be well dispersed, forming a stable suspension without agglomerates.

1.5.2 Ink stability

Particles that are too large can clog the nozzle, but the agglomeration of particles can also hinder the printing process. Therefore, functional inks should be sufficiently well-dispersed and stable to prevent such issues.

The first step in the fabrication process of electrodes is to mix the powder with a liquid to form a slurry.

Since the behavior of solutions is predominantly governed by surface forces rather than gravitational forces [167], a thorough understanding of colloid and surface science is essential for formulating stable and printable ink.

When a particle is immersed in a solvent, two primary forces that act on its surface are Van der Waals forces and electrostatic forces. Van der Waals forces are attractive and arise due to temporary or induced dipoles in molecules. Electrostatic forces originate from the presence of charged particles or ions on the particle surface and in the solvent. Depending on the charges and their distribution, electrostatic forces can be either attractive or repulsive. They play a significant role in determining the stability and behavior of colloidal particles in a solvent [175].

A perfect stoichiometric compound is neutral, but once its surface oxidizes or hydrolyzes, hydroxyl and other groups can create charges when dispersed in protic solvents [176].

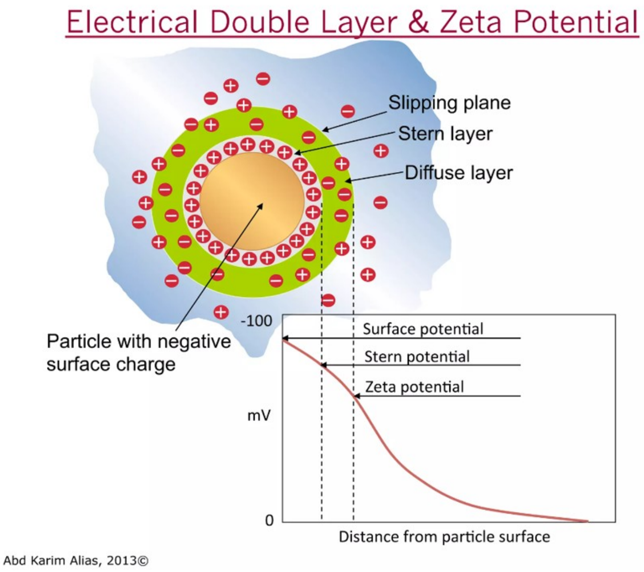

Figure 1.23: Schematic illustration of electrical double layer and zeta potential [177].

When the charges on the particles' surface are formed, a liquid's counterions attract to them, creating a Stern layer, followed by a diffuse second layer via the Coulomb force (Figure 1.23). This second layer is loosely attached. Instead of being firmly fixed, it is formed of free ions that move in the fluid as a result of electric attraction and thermal motion. The boundary of the layer, which remains attached to the particle, is called the shear plane (slipping plane). Zeta potential, a key component of the theory of colloidal particle interaction, is the value of the electric potential measured at this plane [178].

The pH of the slurry strongly influences the zeta potential of ceramic suspensions. Figure 1.24 shows a qualitative representation of the zeta potential as a function of pH for aqueous suspensions. As the pH increases, the value of the electric potential decreases, crossing the abscissa at the Iso-Electric Point (IEP) or the Point of Zero Charge (PZC). This point refers to the pH value, at which the surface net charge of the particles is equal to zero. While pH values outside this domain produce zeta potentials that are normally thought of as stable, the pH around this point, extending out to -30mV and +30mV, is believed to give an unstable colloid [176], [179].

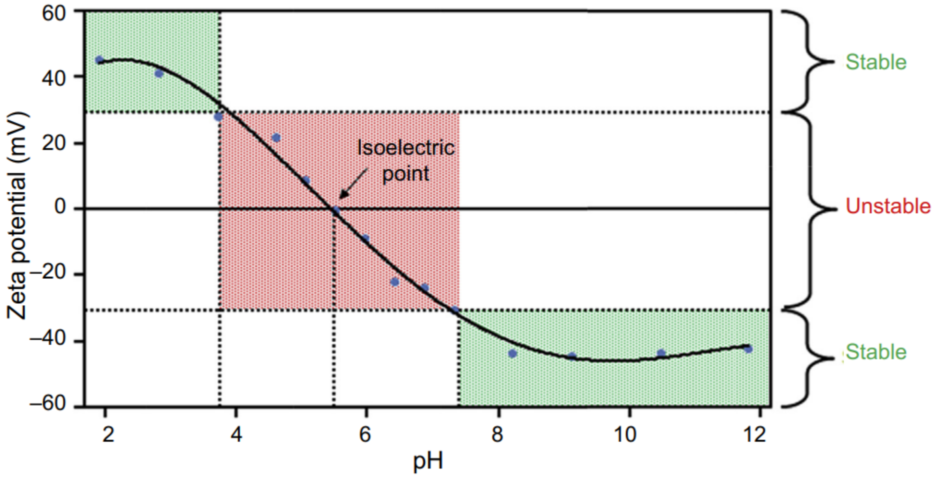

Figure 1.24: Qualitative representation of the zeta potential as a function of pH [179].

In the 1940s, Boris Derjaguin, Lev Landau, Evert Verwey, Theodoor Overbeek combined the attractive van der Waals interaction with the double-layer repulsion and calculated the total forces acting between two particles, giving the foundation of the DLVO theory. According to the DLVO theory, total interaction energy V_T is the sum of attractive potential energy V_A and repulsive potential energy V_R:

$$V_T = V_A + V_R \tag{1.4}$$

A representation of the general case is shown in Figure 1.25. At large distances denoted as a secondary minimum, a weak attraction controls the interaction of the particles (reversible aggregation). At intermediate distances, electrostatic repulsion is dominant, allowing for a stable suspension formulation. At short distances (primary minimum), there is a strong interparticle attraction, causing irreversible aggregation. Generally, the DLVO interaction energy depends on the Hamaker constant, a coefficient accounting for the van der Waals interaction, surface potential, and ionic strength. Suspensions composed of only one kind of particles, may be stabilized by modification of pH or by decreasing the ionic strength so that the range of the double layer repulsion is increased [165].
However, very often, it is not possible to stabilize the suspension simply by modification of pH. Large quantities of acid or base may dissolve the particles or produce an excessively strong ionic strength. In such cases, other methods may be used: steric stabilization, electrosteric stabilization, or depletion stabilization.

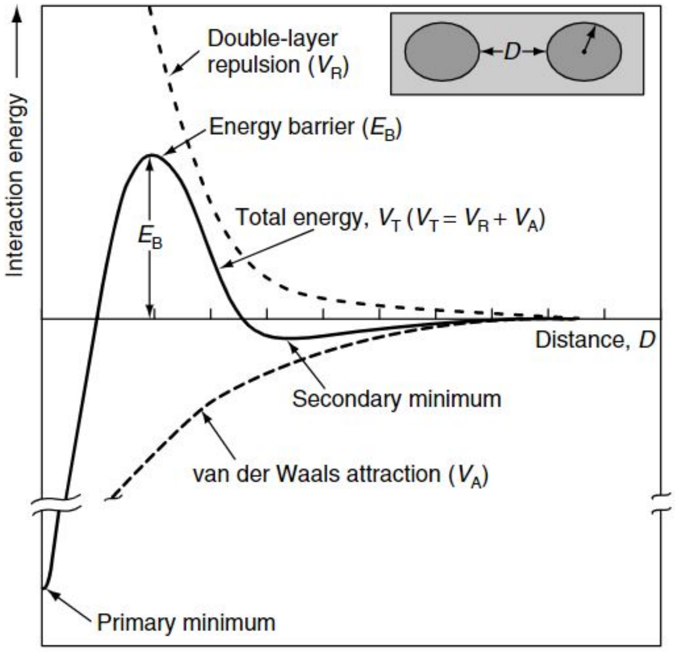

Figure 1.25: Interaction energy between particles as a function of distance between them. The sum of attractive van der Waals force and repulsive electrostatic interaction gives the total interaction energy [165].

Steric stabilization (Figure 1.26a) applies when the polymer without electrostatic charge is adsorbed onto the particles' surface. As a result, such formed layers of two particles approaching each other overlap, preventing their aggregation. When the polymer has an ionic nature, the stabilization is ensured by the combination of electrostatic and steric forces, called electrosteric stabilization (Figure 1.26b). In this case, the repulsion force is stronger due to the charge on the polymer [180]. Lastly, depletion stabilization (Figure 1.26c) refers to when nanoparticles or nonadsorbed, dissolved polymers are placed between the solid particles. This leads to the decrease of attractive forces, improving stability [181].
In nonaqueous systems, the EDL mechanism is a complex topic, and electrostatic interactions between particles are usually of minor importance. Accordingly, steric stabilization is dominant in nonaqueous colloids [182].

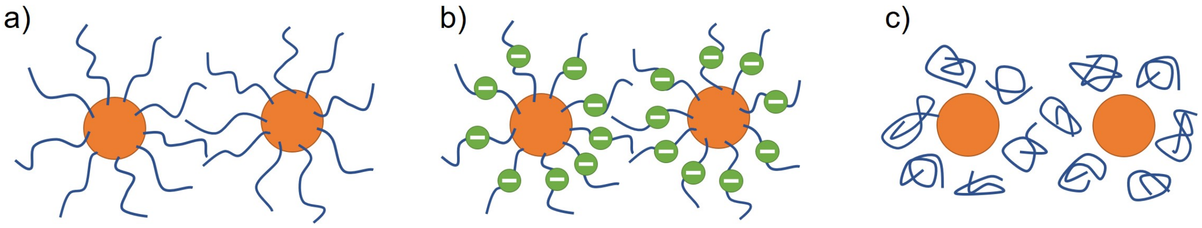

Figure 1.26: Stabilization mechanisms: a) steric stabilization; b) electrosteric stabilization; c) depletion stabilization.

Summary:

- The main requirements for printable inks relate to the viscosity, surface tension, stability, and particle size of powders.
- The Z value (the inverse of the Ohnesorge number) is a simplified assumption for ink printability, commonly used in most commercial DOD printing systems. Generally, when 1<Z<10, ink is considered printable. For Z<1, the viscosity is too high, preventing the ejection. On the other hand, when Z is greater than 10, satellites are formed next to the main drop, resulting in poor printing quality.
- The Ohnesorge number is unambiguously determined for simple Newtonian fluids, but most of the functional inks exhibit non-Newtonian behavior, *e.g.* viscoelasticity, shear-thinning. Therefore, a universal window that can be used to forecast fluid behavior during printing does not exist, and each formulation should be considered individually.
- Particles that are too large can clog the nozzle, and also agglomeration of them can impede the printing. Therefore, functional inks should be sufficiently well-dispersed and stable.
- According to the well-known DLVO theory, the stability of aqueous colloidal dispersions depends largely on interparticle forces, among which van der Waals attraction and electrostatic repulsion play a major role. Balancing them, a well-dispersed system may be obtained, where every particle is separated from one another.
- In nonaqueous systems, electrostatic interactions between particles are usually of minor importance. Accordingly, steric stabilization is dominant in nonaqueous colloids.

2

Materials and methods

Summary

This chapter provides a general overview of materials and methods used for the fabrication and characterization of LIBs' electrodes. More information about the procedures and characterization instruments for each study may be found in the methodology sections of their corresponding chapters.

2.1 Methods

2.1.1 Experimental methods

Powder preparation

In order to meet the criteria for inkjet printing technology regarding particle size, some powders had to be milled. A few grinding techniques were tested and are presented below. The powder was mixed with isopropanol and dispersing agent BYK-9076 to facilitate the process. Zirconia balls of various sizes were used as grinding media. After each milling, the suspension was filtered, and the powder was recovered.

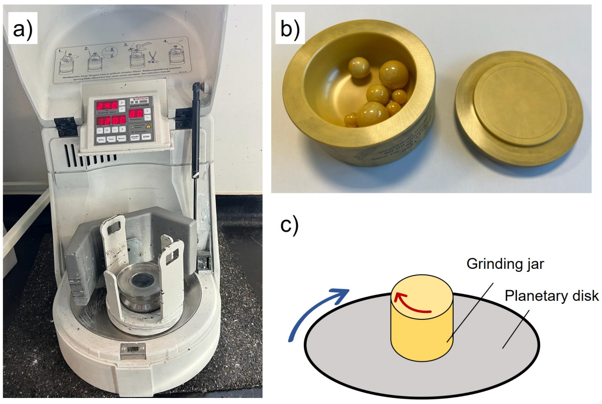

Figure 2.1: a) Planetary ball mill PULVERISETTE 6 Fritsch, b) Zirconium oxide jar, c) schematic configuration of planetary ball mill.

Planetary ball milling using planetary ball mill PULVERISETTE 6 Fritsch (Figure 2.1a). Zirconium oxide jar (Figure 2.1b) containing the powder to be milled, grinding balls, and a solvent, rotates around its own axis, being installed on a disk, which moves in the opposite direction (Figure 2.1c). The maximum rotational speed is 650 rpm.

Attrition milling using attrition mill NETZSCH (Figure 2.2a). Powder, grinding balls, and solvent are introduced to a plastic jar. A stirring shaft with arms placed in the jar (Figure 2.2b) rotates around its axis, agitating the material and media. A schematic representation of the working principle is shown in Figure 2.2c. The maximum rotational speed of the shaft is around 1000 rpm.

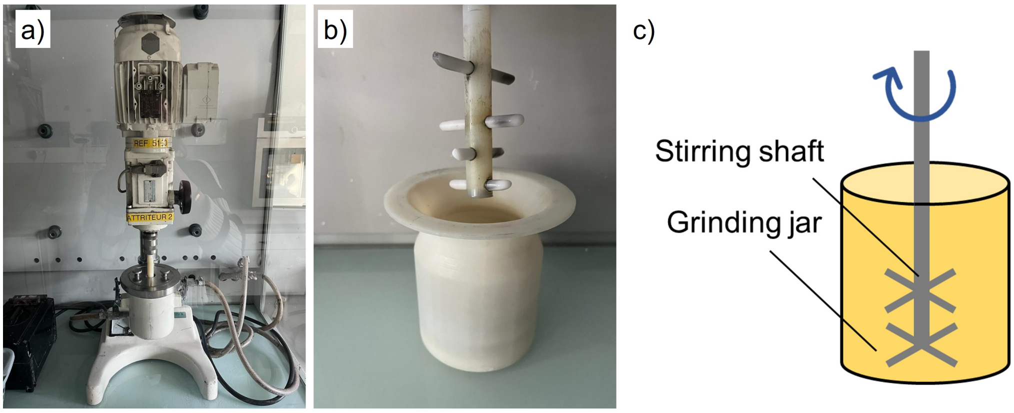

Figure 2.2: a) Attrition mill NETZSCH, b) jar and stirring shaft of attrition mill , c) schematic representation of the working principle of attrition mill.

High energy ball milling using high energy ball mill E$_{MAX}$ Retsch (Figure 2.3a), which features extreme friction, high-frequency impact, and controlled jar movement. Powder, grinding balls, and solvent are introduced to a jar (Figure 2.3b) made of zirconium oxide. The jar is installed on a grinding station, rotating with precise and controlled movement (Figure 2.3c). The maximal speed totals 2000 rpm. The motion of the balls is highly dynamic. They collide with each other and with the sample at high speed, leading to particle size reduction through a combination of impact and friction forces. Additionally, the E$_{MAX}$ is equipped with a cooling system that prevents overheating of the sample, allowing for safe and efficient milling even for heat-sensitive materials.

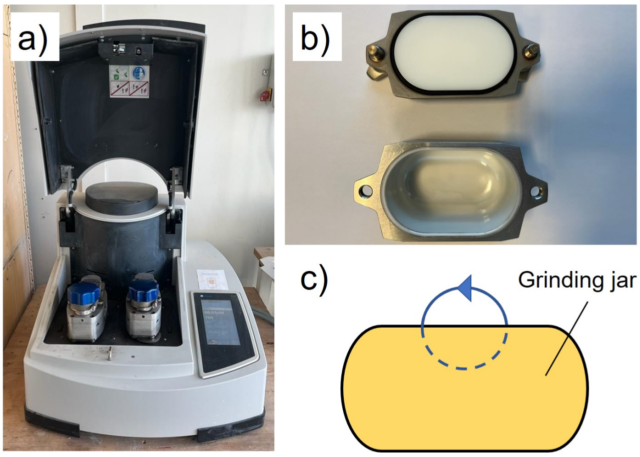

Figure 2.3: a) High energy ball mill E$_{MAX}$ Retsch, b) jar for high energy ball mill, c) schematic representation of the jar movement in high energy ball milling.

Ink preparation

Functional inks for electrode fabrication were formulated with three main components: an active material, a conductive agent, and a binder. All the elements were mixed with a solvent and a dispersing agent. Detailed characteristics of the formulations are presented in the following chapters. This section presents a general overview of the inks preparation procedures. Generally, in the first step, a binder was dissolved, and simultaneously, the powders were combined with a solvent. Subsequently, the two suspensions were merged together. A binder was dissolved in the previously selected solvent via magnetic stirring. Active material and conductive agent were dispersed in the solvent with the optimal quantity of a chosen dispersing agent.

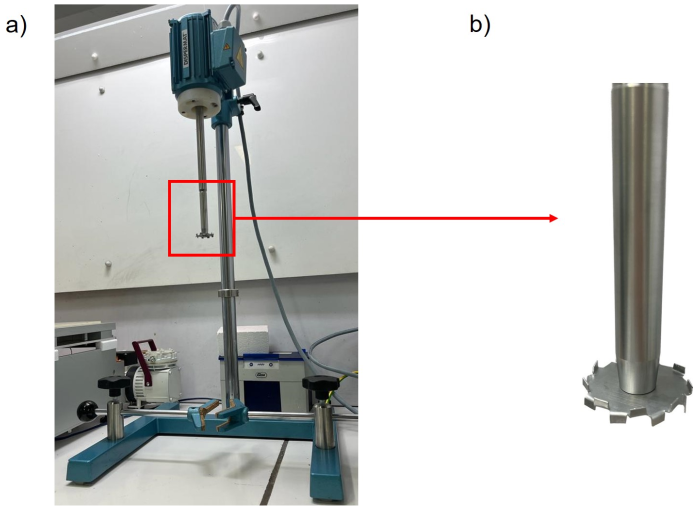

Figure 2.4: a) High-speed disperser Dispermat, b) dissolver disc.

To obtain a well-dispersed suspension, we used a high-speed disperser Dispermat (Figure 2.4a) with a dissolver disc (Figure 2.4b) that can rotate around its axis up to 20000 rpm, mechanically breaking down the agglomerates. Ultrasonic bath was used in some cases to facilitate the dispersion. In the end, the dissolved binder and dispersed powders were mixed together via magnetic stirring. A schematic representation of the mixing procedure is shown in Figure 2.5. Before printing, to eliminate possible big agglomerates, inks were filtered using glass microfiber 1.2 µm or 2 µm filters (Whatman).

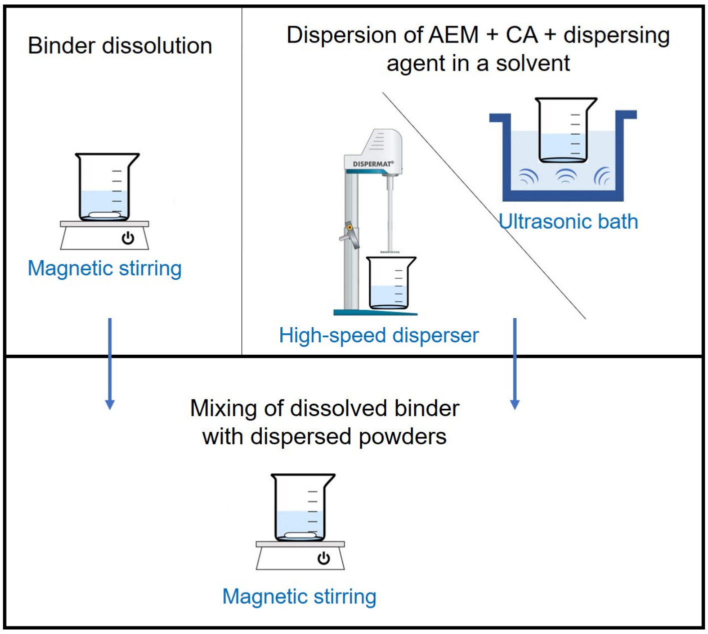

Figure 2.5: Schematic representation of the mixing procedure of electrode ink formulation. AEM - Active Electrode Material, CA - Conductive Agent.

Inkjet printing

Printing and printability tests were performed using piezoelectric drop-on-demand inkjet printer CeraPrinter X-Serie (Ceradrop) with the printhead Dimatix SClass SL (Fujifilm) with 128 nozzles of a nominal droplet volume of 80 pL and the diameter 50 µm.

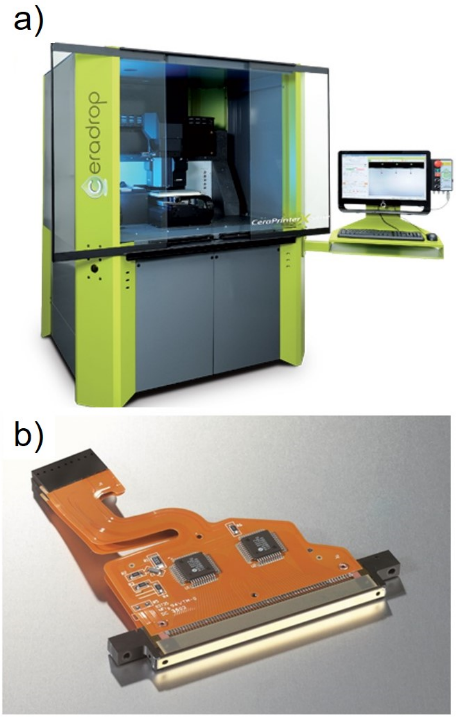

Figure 2.6: Photos of: a) inkjet printer CeraPrinter X-Serie [139], b) printhead Dimatix SClass SL [183].

It is recommended for this printer to formulate inks with a viscosity between 5 and 20 mPa.s, a surface tension from 30 to 35 mN/m, and a particle size lower than 1 µm. Before transferring inks to the cartridge, each was passed through a filter to remove possible big particles. Fabrication was done onto a current collector, with the possibility of heating the substrate holder to $60°C$. The working distance (distance between the nozzle and the substrate) was fixed at 500 µm.

A trapezoidal voltage waveform (see Figure 2.7) including a rise time t_{rise}, peak hold at the maximum voltage V during a dwell time t_{dwell}, and drop to 0 V during a time t_{fall} is supplied to the piezoelectric material to push and eject the liquid. The electric pulse was adjusted separately for each ink through a trial-and-error approach until a stable drop generation process was obtained. Due to printhead limitations, the maximum applied voltage is 120 V, and the total time cannot exceed 15 µs. The behavior of inks exiting the nozzles was registered by a stroboscopic image acquisition system.

In this work, the feasibility of printing thin layers as well as 3D structures is investigated. 3D structure is made up of electrodes' pillars at the microscale, evenly distributed on the current collectors (see Figure 2.8a,b). The design of the full battery cell is shown in Figure 2.8c,d. The anode columns are placed in between the cathode ones and the structure is impregnated by an electrolyte. Another possibility is to

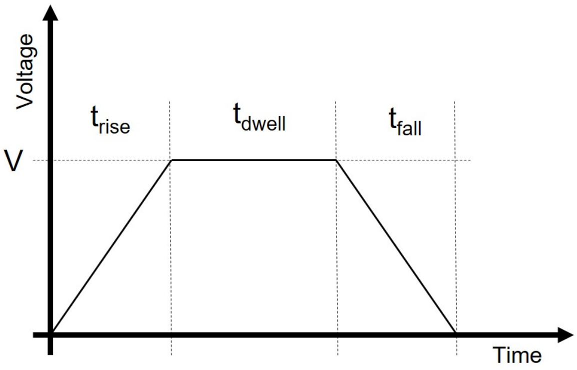

Figure 2.7: Typical trapezoidal voltage waveform for piezoelectric inkjet printhead.

print the cathode, electrolyte, and anode in one step, but in this case, the electrolyte's material must be also included in the electrode's inks. This may change drastically the rheological characteristics of slurry, and consequently the fluid behavior during printing. In this work, we solely discuss the printing of electrodes, and the fabrication of a full battery cell is our future perspective.

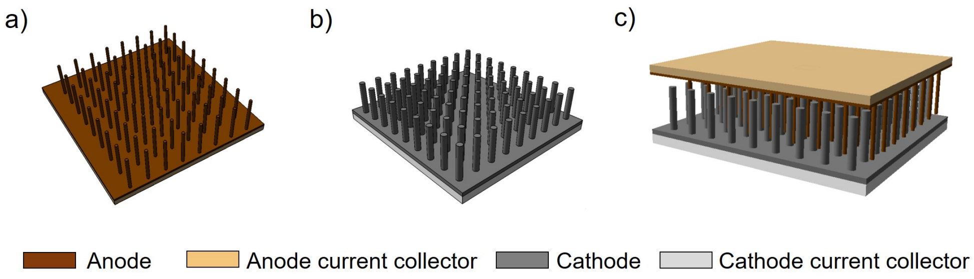

Figure 2.8: The design of 3D battery cell structure: a) pillars of anode, b) pillars of cathode, c) full battery cell.

Tape casting

Reference samples for the electrochemical measurements were fabricated by tape casting using an automatic film applicator Elcometer 4340 (Elcometer) (Figure 2.9a) and doctor blade Elcometer 3580/7 (Figure 2.9b), which allows for the film deposition of the thickness 1-6000 µm.

The applicator is equipped with a perforated vacuum table, which assists in holding the substrate in place and prevents it from slipping during the application process. This helps to ensure the accurate placement of the film and reduces the likelihood of defects or errors in the final product.

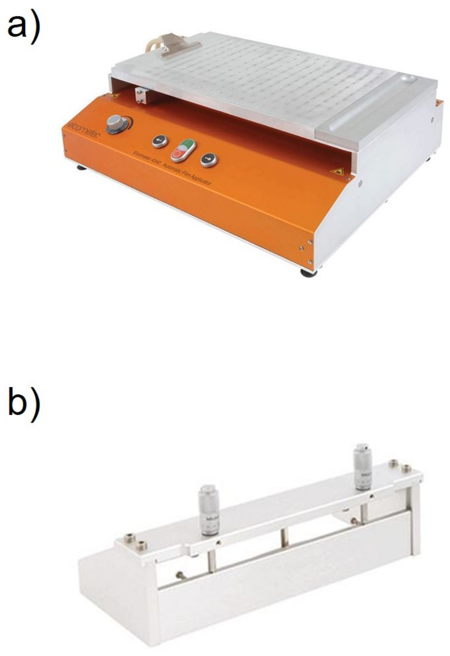

Figure 2.9: Photos of: a) automatic film applicator Elcometer 4340, b) doctor blade Elcometer 3580/7 [184].

2.1.2 Characterization methods

X-ray Diffraction (XRD)

D8 advance diffractometer (Bruker) equipped with LYNXEYE XE detector, which offers a huge advantage in terms of intensity, was used to determine the crystal structure of samples. The anti-cathode is made of copper (X-ray wavelength of 1.5406 Å). The diffractometer uses Bragg-Brentano geometry: the sample is fixed while the detector and the source are in motion. Diffractograms were collected over the angular range of 10-80° with a step size of 0.02°, and a dwell time of 0.9 s per increment.

The recorded diffraction pattern is unique to the crystalline structure of the sample, allowing for the identification of specific crystal phases present. Analyzing the shape and position of peaks may provide information on the changes in the crystal structure.

In our work, the Modified Scherrer formula, Williamson-Hall (W-H) and Size-Strain Plot (SSP) methods were used to estimate the average crystallite size and lattice strains based on the collected diffraction patterns. The details on the analyses are provided in Chapter 3.

Microscopy

Scanning electron microscope LEO 1530PV (Zeiss) was used to observe the morphology of powders and printed patterns. Images of cross-sections of printed structures were performed using Focused Ion Beam Scanning Electron Microscopy (FIB-SEM) Crossbeam 550 (Zeiss). The morphology and size of the nanopowders used in the study were examined using the 2100F transmission electron microscope (TEM) (JEOL).

The 3D view of printed patterns was obtained using the 4K ultra-high accuracy digital microscope (Keyence).

Particle size analysis

The LA-950 Laser Particle Size Analyzer (Horiba) was used to measure the particle sizes of powders. This technique is based on the principle of laser diffraction. In this study, liquid samples containing powders dispersed in a solvent were analyzed. A laser beam is directed through the solution, and the particles scatter the laser light in different directions. The intensity and direction of scattered light at different angles are captured by a detector at various angles. Fraunhofer diffraction theory was used to determine the particle size distribution, but this theory exclusively considers the diffraction phenomena that take place at the contour of the particles. As the particle diameter becomes comparable to the wavelength of the incident light, the effects of refraction and absorption become more prominent and start to influence the scattering patterns. Therefore, this technique was used to analyze the particles in the micrometric range.

To analyze submicron particles, Zetasizer Nano ZS (Malvern Panalytical) instrument was used. This analytical technique is founded on the principle of Dynamic Light Scattering (DLS), where the size of particles is determined by measuring fluctuations in scattered light intensity caused by their Brownian motion. In this method, a laser beam is directed into a diluted suspension of powder in a solvent. The particles scatter the incident laser light in various directions. The intensity fluctuations in the scattered light are then examined, and the particle size is calculated using the Stokes-Einstein relation.

Zeta potential measurement

For the aqueous inks, the zeta potential versus pH was measured for each powder using Zetasizer Nano ZS (Malvern Panalytical). The results helped us understand and improve the colloidal stability discussed in the introduction section. A sample (dispersion of powder in DI-water) is placed in a disposable folded capillary cell (DTS1070) that contains two electrodes. When a voltage is applied, charged particles move in the cell at a rate that is proportional to their zeta potential. The particle velocity is estimated by the Doppler method. A laser beam passes through the cell, and the light is scattered from the particles [185]. The particle speed is measured by a Doppler frequency shift and can be converted into a value of zeta potential using the Henry Equation:

$$U_E = \frac{2\varepsilon Z f(ka)}{3\eta}, \tag{2.1}$$

where U_E is electrophoretic mobility (velocity of particles per field strength), ε, Z, and η are dielectric constant, zeta potential, and viscosity respectively, and f(ka) is Henry's function [186].

The analysis may be done at the full range of pH. First, the system doses acidic or basic solutions to the cell, changing the pH of a sample. After reaching the required acidity/basicity, the measurement is run. In our study, we used NaOH (0.1M) and HCl (0.1M) to adjust pH.

Stability analysis

The stability of formulated inks was evaluated using Turbiscan LAB (Formulaction). The measurement method is based on dynamic light scattering, and a schematic representation of the working principle is shown in Figure 2.10. The analyzed suspension placed in a transparent container is vertically scanned by a head, which emits a near-infrared light beam ($\lambda = 880\,\text{nm}$) toward the specimen. The backscattered and transmitted lights are collected by detectors and plotted as a function of the height of the sample. The resulting data is then analyzed to determine the stability of the ink. This technique can detect the onset of various destabilization mechanisms, including agglomeration and sedimentation. Three commonly recognized zones during the settling, namely supernatant, suspension, and sediment (see Figure 2.11), may be identified. The supernatant contains mainly clear solvent with very few or no solid particles present. The emitted light can be almost fully transmitted without backscattering. On the contrary, the sediment region backscatters the beam, and no transmission is observed. The suspension is the intermediate region where both phenomena can occur to a different extent.

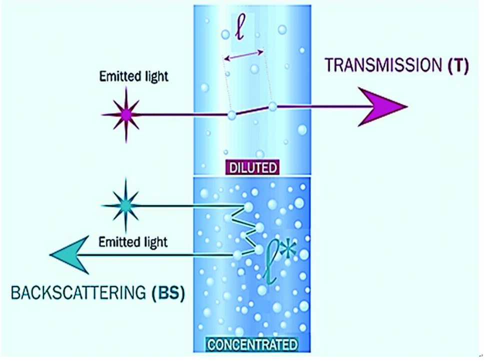

Figure 2.10: Schematic representation of the working principle of Turbiscan LAB [187].

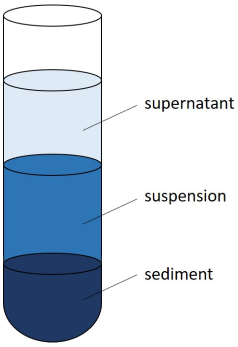

Figure 2.11: Three commonly recognized zones during the settling: supernatant, suspension, and sediment

The stability of inks was also tested by simple sedimentation tests. The samples were filled into test tubes and placed on a steady surface, remaining undisturbed for a predetermined duration. Subsequently, the settling behavior was visually evaluated, with longer settling times indicating greater ink stability.

Spectroscopy

A Nicolet 6700 Fourier-Transform Infrared Spectrometer (FTIR) (Thermofisher) was used to gather information concerning functional groups of powders. The FTIR spectra were recorded within the range of 4000 to 475 cm^{-1} with a resolution of 2 cm^{-1} and using 256 scans. Smart Diffuse Reflectance accessory was used with a double-cup sample holder for measuring a powder sample and background. Potassium Bromide (KBr) was used for the background acquisition.

Inductively Coupled Plasma (ICP)

Inductively Coupled Plasma (ICP) Optical Emission Spectrometer (OES) Optima 8300 was used to detect the elements leached to the solution. Powder was stirred in water for 24h. Subsequently, the resulting mixture was subjected to centrifugation and filtration utilizing a 0.1 µm PTFE syringe filter (Whatman). The resulting solution, devoid of any remaining powder, was used as the sample for ICP analysis.

Viscosity measurements

The viscosity as a function of the shear rate was evaluated using Discovery Hybrid Rheometer HR-2 (TA Instruments) (Figure 2.12a) with double wall concentric cylinders steel geometry (inside cup diameter 40 mm, inner cylinder height 21 mm) (Figure 2.12b). The geometry is rotated at a controlled speed, which induces shear on the sample. The deformation applied depends on the specific rheological property being measured. Sensors in the rheometer measure the response of the sample to the applied deformation, such as the resulting stress, and the data is further analyzed to determine the viscosity.

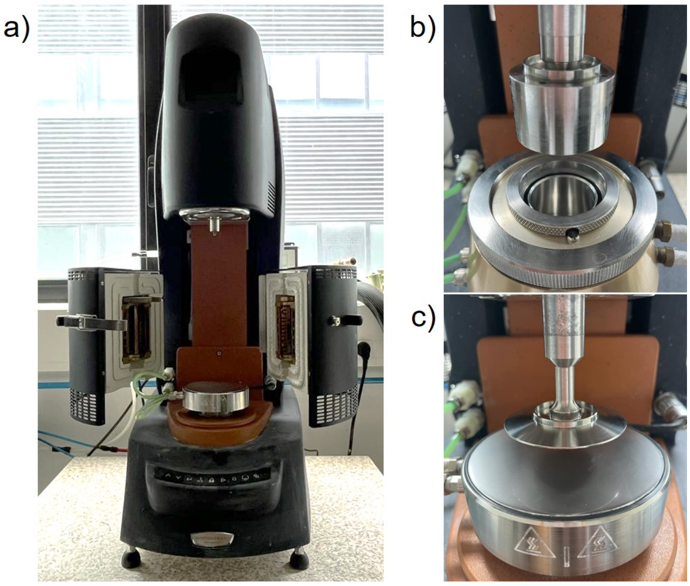

Figure 2.12: Photos of: a) Discovery Hybrid Rheometer HR-2, b) double wall concentric cylinders geometry, c) titanium cone plate geometry.

The Discovery Hybrid Rheometer HR-2 rheometer was also used for viscoelasticity measurements of binders. For this analysis, a titanium cone plate geometry (60 mm in diameter, 1.997° cone angle) (Figure 2.12c) was employed. The geometry is subjected to the specified range of frequencies of oscillatory shear deformation. Sensors in the rheometer measure the response of the sample, such as the resulting shear stress and shear strain. The data is further used to calculate the storage modulus (G') and the loss modulus (G") of a binder as a function of frequency.

To determine the optimal amount of dispersing agent, more precise viscosity measurements were performed using the microfluidic rheometer Fluidicam RHEO (Formulaction). In this technique, a sample and a standard fluid with a known viscosity value

co-flow in a microfluidic chip.
This results in the formation of a visible interface between the two fluids, which is captured in real-time using a high-resolution optical image acquisition system. By comparing the behavior of the two fluids at the interface, the viscosity of the sample can be determined. For all the tests, the temperature was set to 20°C.

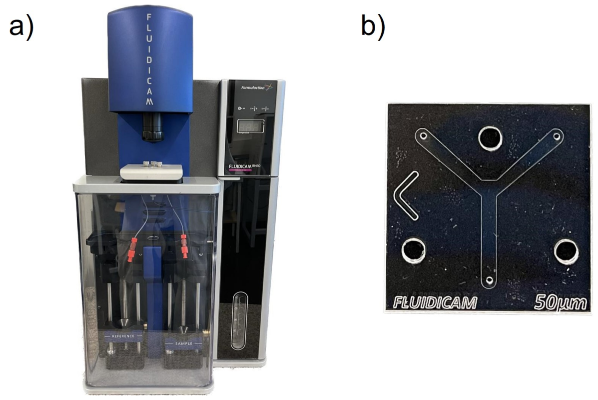

Figure 2.13: Photos of: a) microfluidic rheometer Fluidicam RHEO, b) microfluidic chip.

Surface tension measurements

The surface tension was measured by the tensiometer DCAT21 (Dataphysics) with a platinum Wilhelmy plate. As the Wilhelmy plate is submerged into a liquid, the liquid wets the surface of the plate, causing a meniscus to form at the liquid-air interface along the edges of the plate. When the plate is subsequently withdrawn from the liquid, the force needed to detach the plate from the liquid is measured. This measured force is then used to determine the surface tension of the liquid. The test temperature was set to 20°C.

Electrochemical testing

All the electrochemical measurements were done by partner institutions, at CEA in Bordeaux/France and at Fraunhofer IKTS in Dresden/Germany.
The experiments were carried out using CR2032 coin cells, which have a diameter of 20 mm and a thickness of 3.2 mm. This configuration represents the widely accepted standard for conducting tests and assessments of battery materials.

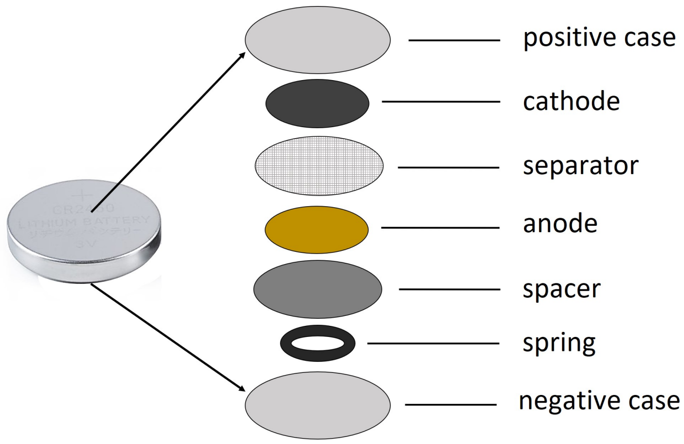

Figure 2.14: Coin cell configuration used for electrochemical testing of battery materials.

The assembly process of the cells took place inside a glove box. It involved stacking a cathode, separator, anode, spacer, and spring together, along with a liquid electrolyte, within a metallic case (refer to Figure 2.14). This metallic case functions as terminals that can be connected to devices or battery holders. The separator, a thin and

porous material, is positioned between the cathode and anode to prevent direct contact and short circuits, while enabling the flow of ions between them.
In a coin cell, the spring has the purpose of exerting consistent pressure on the cell components. This pressure ensures that the various components maintain good electrical contact with each other. The spacer, on the other hand, evenly distributes the force exerted by the spring, maintaining balance and stability within the cell assembly.

Galvanostatic cycling was performed to evaluate the performance and behavior of the battery over multiple charge and discharge cycles. During the charging phase of galvanostatic cycling, a steady current is supplied to the cell, initiating electrochemical reactions at the battery's electrodes. These reactions involve the migration of ions between the positive and negative electrodes, accompanied by the storage or release of electrical energy. Upon reaching the desired state of charge, the cycling transitions to the discharge phase. Here, the battery supplies a constant current back into the external circuit, providing electrical energy for various applications. Throughout the galvanostatic cycling process, the voltage across the battery is continuously monitored and recorded. Detailed analysis of the voltage and current data enables the evaluation of key battery parameters, such as capacity, energy efficiency, power capability, and cycling stability. Additional details regarding the procedures of galvanostatic cycling can be found in the corresponding chapters.

Electrochemical Impedance Spectroscopy (EIS) was used to analyze the electrochemical behavior of cells. It involves the application of small amplitude alternating current (AC) signals across the battery terminals over a wide frequency range and measuring the resulting voltage response. By analyzing the phase and amplitude of the voltage and current signals, the impedance of the system is determined. Impedance is represented as a complex number with a real component (Z') and an imaginary component (Z"). The resulting impedance data is typically presented as a Nyquist plot or a Bode plot.
At high frequencies, the impedance spectrum typically exhibits a semicircular arc in the Nyquist plot. This semicircular arc represents the charge transfer resistance associated with the electrochemical reactions occurring at the electrode-electrolyte interfaces. The diameter of the semicircle is related to the rate of charge transfer and can provide insights into the kinetics of the electrochemical reactions.
At low frequencies, the impedance spectrum shows a linear portion, often referred to

as the Warburg region, which represents diffusion processes within the battery system. The slope of the linear region can provide information about the diffusion coefficients of ions within the electrodes or electrolyte.

A Bode plot, on the other hand, displays the magnitude and phase of the impedance as functions of frequency. The magnitude plot represents the absolute value of the impedance, indicating the overall resistance or impedance of the battery system at different frequencies. The phase plot represents the phase shift between the applied AC signal and the resulting voltage response, providing insights into the time delays and energy storage mechanisms within the battery.

EIS measurements were performed in the frequency range 0.1 Hz to 1 MHz (10 points per decade), with a voltage amplitude of 10 mV at 25°C with 1h30min rest after formation.

Particles emission measurements

In order to assess the potential harm to human health posed by the processes, the emission of particles during ink preparation and inkjet printing was analyzed using two instruments: the Optical Particle Sizer 3330 (TSI) and the NanoScan SMPS Nanoparticle Sizer 3910 (TSI). Optical Particle Sizer 3330 works on the principle of laser light scattering, where a laser beam is directed through a sample of particles in the air. The scattered light is then collected by the instrument's optics and analyzed to determine the size and number of particles in the sample. It is capable of measuring particles in the size range of 0.3 to 10 µm. To detect nanoparticles, NanoScan SMPS Nanoparticle Sizer 3910 was used, which can measure size distributions from 10 to 420nm.

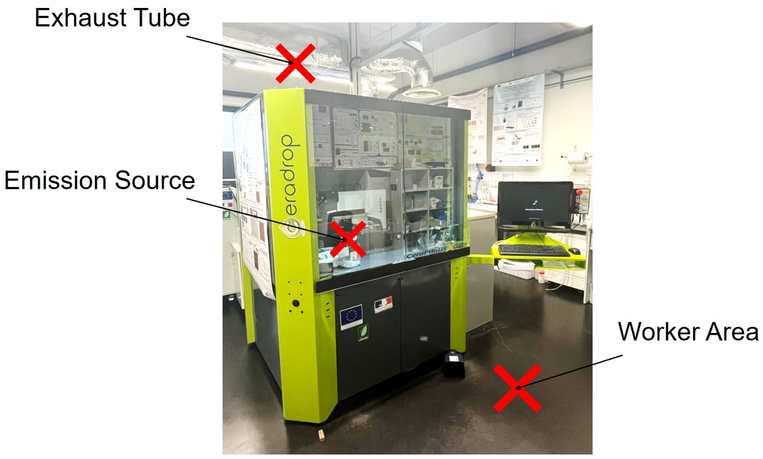

Figure 2.15: Three zones of the emission measurements during inkjet printing: Worker Area (WA), Emission Source (ES), Exhaust Tube (ET).

It works based on a technique called Scanning Mobility Particle Sizing (SMPS), which involves the use of an electrical field to classify particles by their mobility diameter. The instrument operates by drawing a sample of air through a narrow tube, where the particles are electrically charged. The charged particles are then passed through an electrical field, which separates them based on their mobility diameter. The particles are then detected by a condensation particle counter, which counts the number of particles in each size range.

The ink preparation was carried out under fume hoods, with the emission measurement equipment situated in close proximity to the operator. In the first step, the powders were accurately weighed and introduced into a solvent. Subsequently, they were transferred to another fume hood where all the components were mixed together using a high-speed disperser Dispermat.

During the inkjet printing process, emission measurements were performed in three distinct zones: the Worker Area (WA) in close proximity to the operator, the Emission Source (ES) near the printhead within the printing chamber, and the Exhaust Tube (ET) positioned at the top of the inkjet printer (see Figure 2.15).

2.2 Materials

For the formulation of electrodes' inks we used different active materials, conductive agents, binders, additives and solvents, and their different characteristics are presented in Table 2.1. Some materials were provided by partners of ASTRABAT project.

Table 2.1: Overview of materials used in our study.

Material	Function	CAS Number	Supplier
NMC622	Active material	-	Umicore
NMC333	Active material	CAS: 346417-97-8	Sigma Aldrich
SiNp	Active material	-	Nanomakers
Si$\mathit{\Omega}$CNp	Active material	-	Nanomakers
Super P Carbon Black	Conductive agent	CAS: 1333-86-4	AlfaAesar
high M_w binder	Binder	-	DAIKIN
low M_w binder	Binder	-	DAIKIN
CMC $\mathrm{M}_w\sim 90\ 000$	Binder	CAS: 9004-32-4	Sigma Aldrich
CMC $\mathrm{M}_w\sim 700\ 000$	Binder	CAS: 9004-32-4	Sigma Aldrich
PEDOT:PSS	Binder	-	Sigma Aldrich
Triton X-100	Dispersing agent	CAS: 9002-93-1	VWR
BYK 22144	Dispersing agent	-	BYK
acetone	Solvent	-	-
propylene carbonate	Solvent	-	-
DI-water	Solvent	-	-
NaOH	Solvent	-	-

2.2.1 Active materials

Cathode active materials

NMC layered oxides were used as active materials for cathode fabrication. NMC has a hexagonal close-packed crystal structure with space group R-3m and lattice parameters of a ~ 2.8 Å and c ~ 14 Å. Figure 2.16 shows its crystal structure. At the center of oxygen octahedra, the ions of transition metals Ni, Mn, Co are located. These MO_6 octahedra create an edge-shared vertical slab, and in the space between them, Li ions are placed [188].

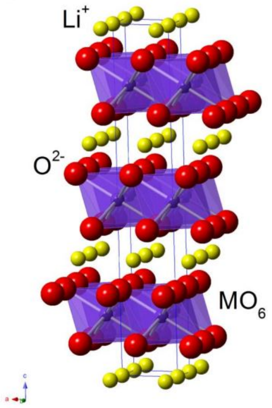

Figure 2.16: Crystal structure of NMC layered oxide [188].

XRD patterns of NMC622 and NMC333 used in our study are presented in Figure 2.17. Both patterns exhibit a well-defined layered structure and no impurity peaks in the detection limit (1% by volume). The (108)/(110) and (006)/(102) doublet peaks showed evident splitting in all the samples, which confirms the high crystallinity of the layered materials [74]. As mentioned in Chapter 1, NMC333 has a lower theoretical capacity compared to NMC622.

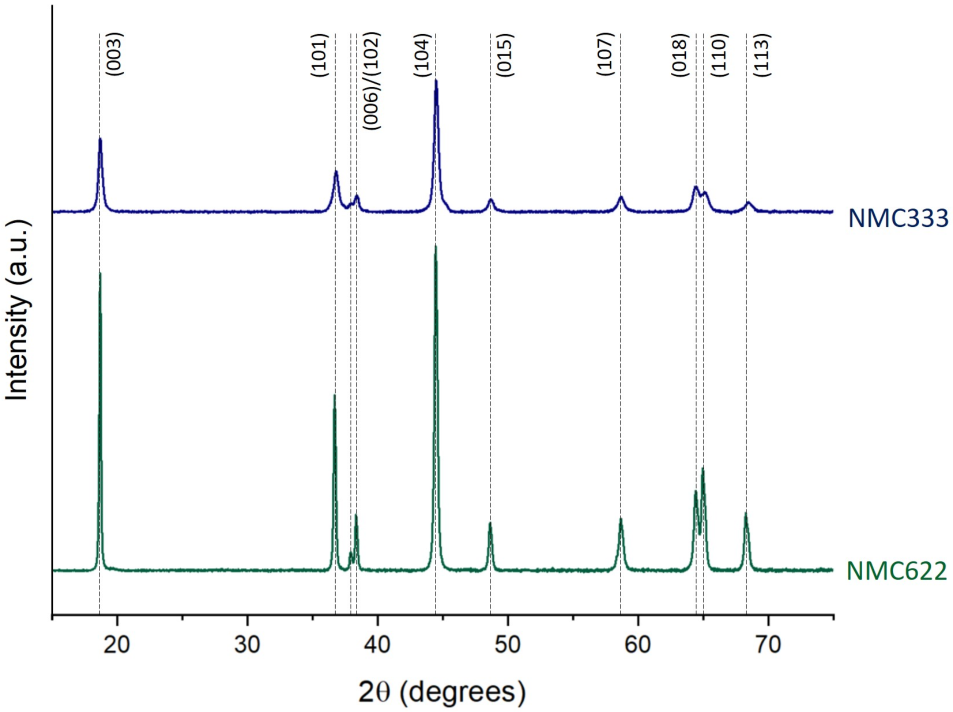

Figure 2.17: XRD patterns of NMC622 and NMC333 powders used in our study.

The morphology of NMC622 powder is shown in Figure 2.18. The powder particles exhibit spherical shapes. When having a closer look, it is observable that a single particle consists of thousands of irregular pieces.

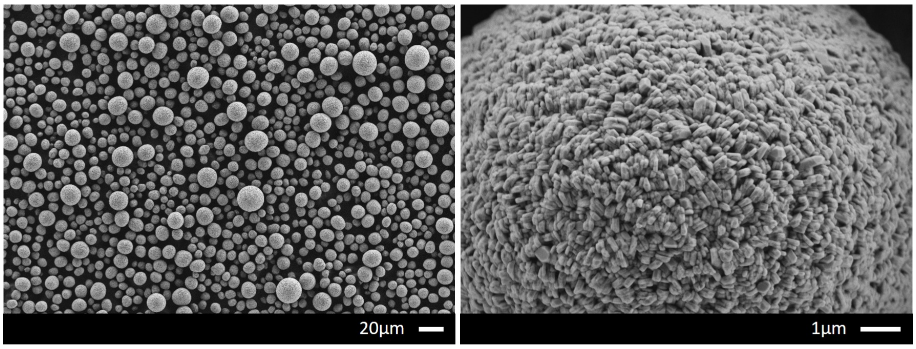

Figure 2.18: SEM images of NMC622 powders provided by Umicore.

Figure 2.19 demonstrates the morphology of NMC333 powder. Primary particles of irregular shapes in sizes below 50 nm create larger agglomerates, which was evidenced by granulometry measurement.

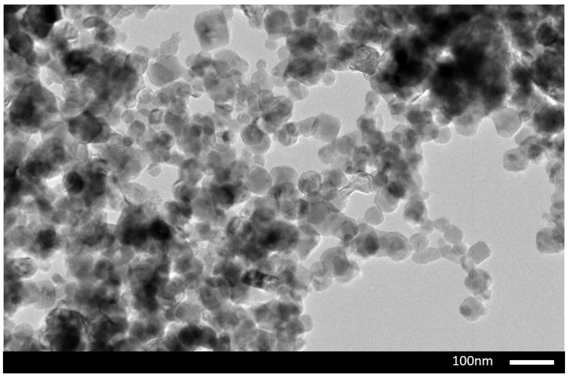

Figure 2.19: TEM image of NMC333 powder purchased from Sigma Aldrich.

Figure 2.20 demonstrates the particle size distribution of NMC powders measured using the laser diffraction method for NMC622, and DLS technique for NMC333. The average size of NMC622 particles is around 10.5 µm, while NMC333 powder is in the sub-micron range. The results of NMC333 present the size of aggregates formed by primary particles.

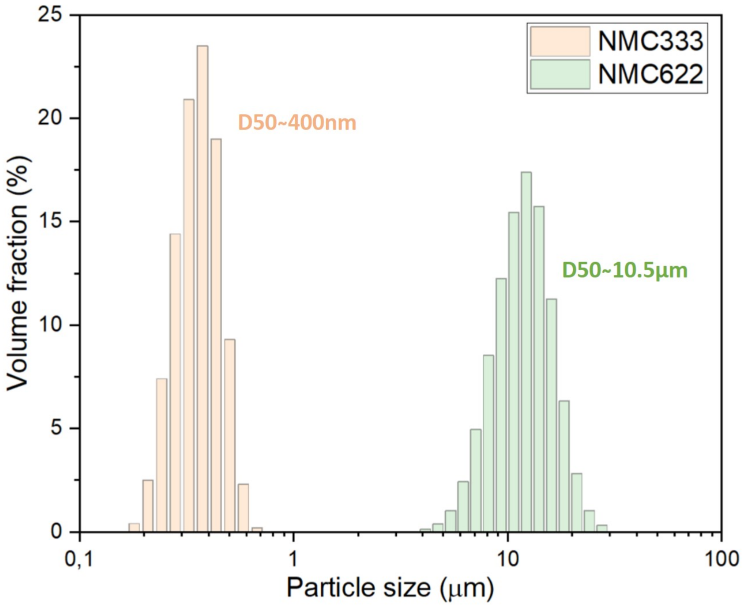

Figure 2.20: Particle size distributions measured using Zetasizer Nano ZS, and LA-950 Laser Particle Size Analyzer for NMC333, and NMC622 powders, respectively.

Anode active materials

For the fabrication of anodes, silicon (Si) and silicon coated by carbon (SiΩC) nanopowders supplied by Nanomakers were used as active materials. BET surface areas are $50\,\mathrm{m^2/g}$ and $60\,\mathrm{m^2/g}$ for Si and SiΩC, respectively.

XRD patterns of both powders are presented in Figure 2.21. Diffractograms are similar, and the peaks (111), (220), (311), (400), and (331) clearly demonstrate silicon phase [189]. The peaks marked with Al correspond to aluminium, which comes from the sample holder.

TEM observations of Si and SiΩC particles (Figure 2.22) do not show a difference between the two powder grades. Primary particles, which are spherical and range in size from 10 to 60 nm, tend to aggregate together, forming string-like structures consisting of a few particles.

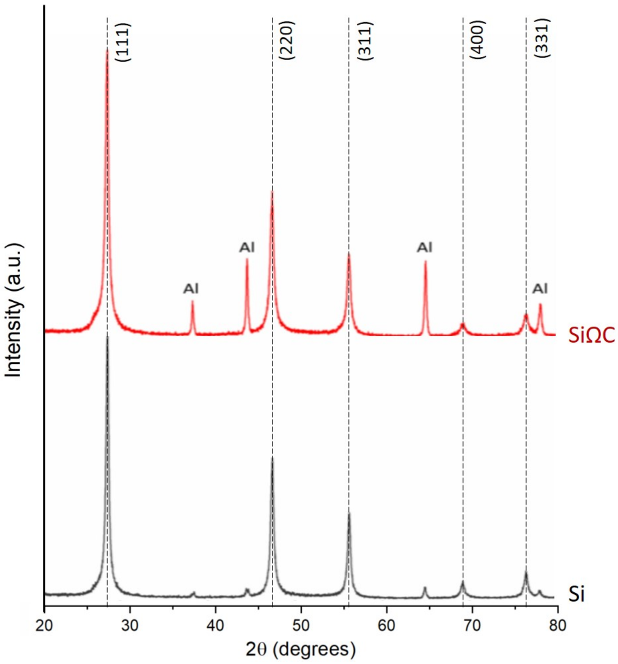

Figure 2.21: XRD patterns of Si and SiΩC nanoparticles.

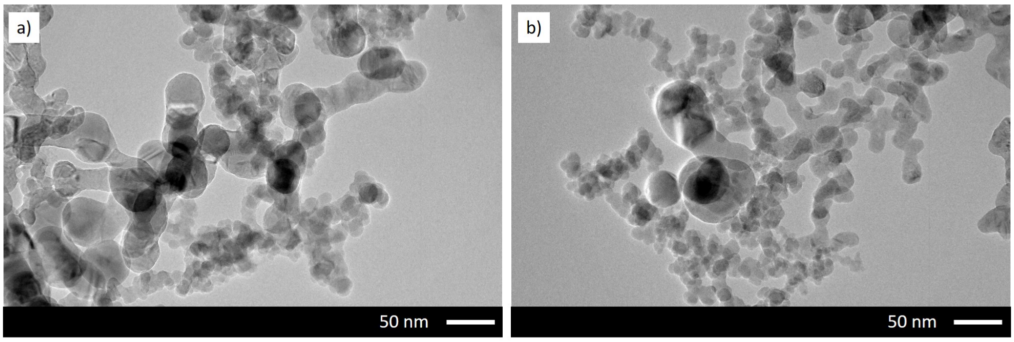

Figure 2.22: TEM observations of: a) Si nanoparticles, b) SiΩC nanoparticles.

Figure 2.23 illustrates the particle size distribution of Si and SiΩC nanoparticles measured using DLS technique. Based on the plots, the average hydrodynamic particle size for both powders is around 200 nm, which corresponds to the aggregation size of primary particles. Although the measurements were performed on well-dispersed and very dilute suspensions (powders in DI-water), Si and SiΩC tend to create strings of a few particles.

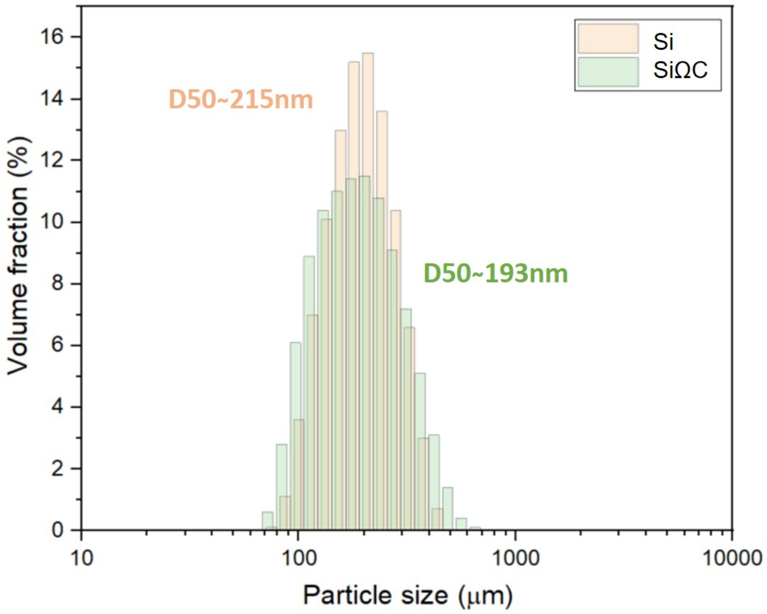

Figure 2.23: Particle size distributions of Si and SiΩC nanoparticles measured using Zetasizer Nano ZS.

2.2.2 Conductive agent

Because of its high electrical conductivity, Super P Carbon Black was used as a conductive agent for the fabrication of electrodes. When added to an electrode material, it increases the number of conductive pathways within the material, thereby reducing the electrical

resistance of the electrode. This, in turn, increases the efficiency of charge transfer within the electrode and improves the overall battery performance [190].
Despite the fact that aggregates are considered the smallest indivisible unit of carbon black, TEM image (Figure 2.24) reveals that they are composed of fused spherical particles of around 40 nm.

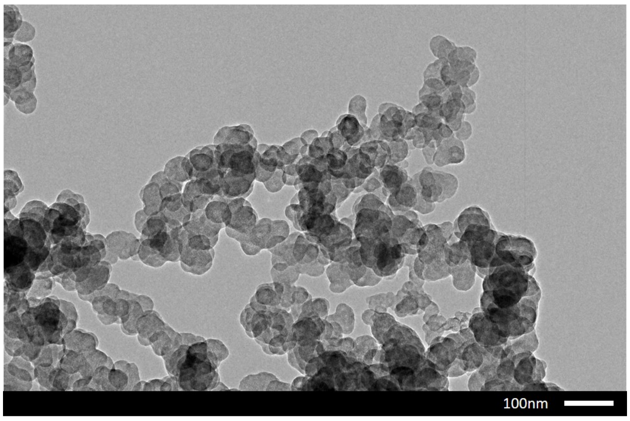

Figure 2.24: TEM observations of Super P Carbon Black.

Result of granulometric measurement (Figure 2.25) displays around 500 nm, as the average particle size, but obviously, it refers to the aggregates. BET surface area of Super P Carbon Black is 57-67 m^2/g.

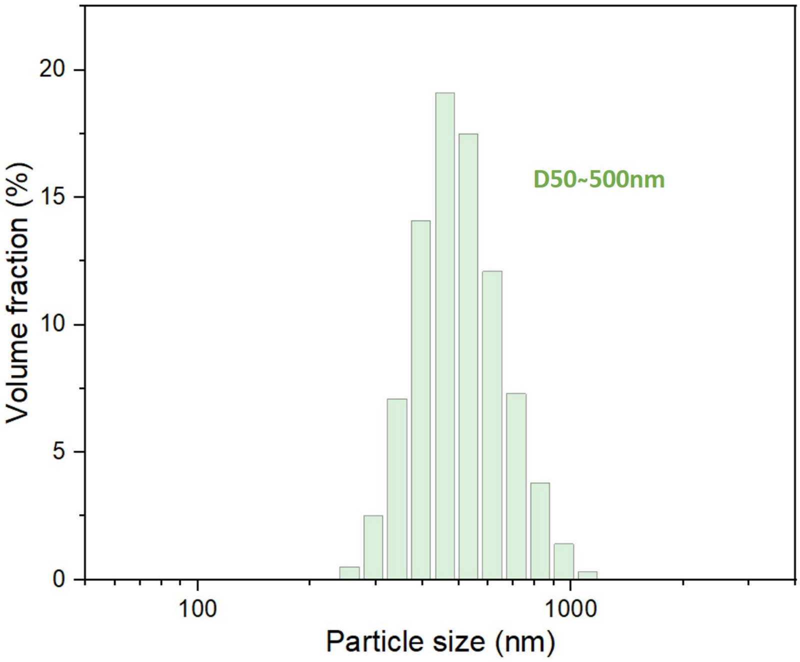

Figure 2.25: Particle size distribution of Super P Carbon Black measured using Zetasizer Nano ZS.

The internal structure of carbon black is not fully understood. However, it has been observed that they contain graphite-like quasicrystalline domains with parallel elementary planes that are angularly distorted. Moreover, the layer spacing is different compared to pure graphite [191].

Biscoe and Warren described this structure as an intermediate type of matter that is noticeably dissimilar from both crystalline and amorphous forms. They have suggested the term 'turbostratic' for this particular type of architecture, consisting of turbostratic groups. Each group is made up of multiple graphite layers stacked together in a somewhat parallel and equidistant manner. However, each layer within the group has a random orientation (see Figure 2.26) [192].

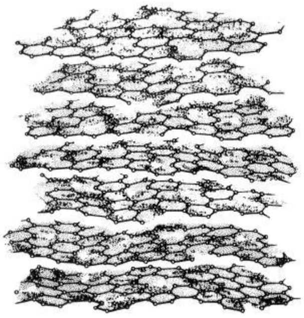

Figure 2.26: Turbostratic structure of carbon black - intermediate type of matter dissimilar from both crystalline and amorphous forms [193].

Figure 2.27 presents XRD pattern of Super P Carbon Black used in our study. Two broad peaks near 25° and 45° can be observed, which correspond to the (002) and (101) reflections, respectively [194]. (002) peak is attributed to graphene and proves the existence of graphene layers. Wide bands, rather than narrow peaks, indicate the structural irregularities [195].

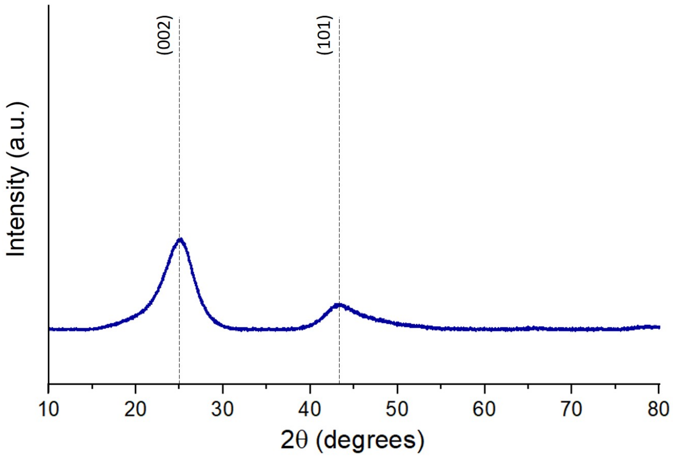

Figure 2.27: XRD pattern of Super P Carbon Black.

2.2.3 Binders

Binders from DAIKIN

DAIKIN - one of our project partners supplied us with a binder (a fluoropolymer) that has been synthesized specifically for use in batteries. This polymer was provided in two molecular weights, and its properties are believed to be beneficial for the cathode performance. The binders are denoted as low M_w binder and high M_w binder for lower and higher molecular mass, respectively. They are soluble in aprotic solvents, such as acetone, acetonitrile, dimethyl sulfoxide (DMSO), and others. Due to confidentiality reasons, more information cannot be provided.

Carboxymethyl cellulose (CMC)

Carboxymethyl cellulose, a water-soluble binder, is extensively utilized in various industries, including food, pharmaceuticals, textiles, detergents, cosmetics, and others [196].
Its monomer structure is schematically represented in Figure 2.28. R denotes –H or –CH_2CO_2Na. The properties of CMC depend greatly on the molecular weight and the Degree of Substitution (DS). DS refers to the average number of carboxymethyl groups that have been substituted per monomer unit and affects the solubility, rheological properties, and other characteristics of CMC, as well as its suitability for various applications [197].

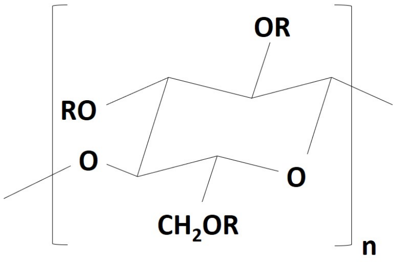

Figure 2.28: Monomer structure of CMC.

CMC is widely used as a binder in the fabrication of electrodes for LIBs, mainly for anodes [144], [198], [199].
In our study, we tested two kinds of CMC, differing in molecular weight, *i.e.* M_w~90 000 g/mol and M_w~700 000 g/mol, as presented in Table 2.1.

PEDOT:PSS

In terms of practical application, PEDOT:PSS is considered to be one of the most successful conducting polymers. With its high electrical conductivity and good physical and chemical stability, it is widely used in energy conversion and storage systems. The structure of PEDOT:PSS is shown in Figure 2.29. It is built of conjugated PEDOT, which is positively charged, and saturated PSS, charged negatively. PSS is a surfactant that assists in the dispersion and stabilization of PEDOT in water, and other solvents [200].

It has been reported in literature, that the use of PEDOT:PSS as a binder for the fabrication of electrodes may significantly improve LIBs' performance [201], [202].

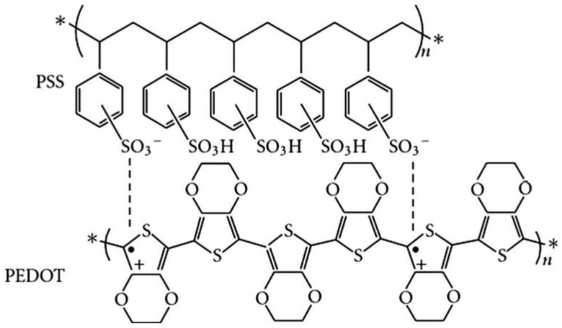

Figure 2.29: Structure of PEDOT:PSS [200].

3

Impact of milling on NMC622 cathode material

Summary

PARTICLE size of powders constituting the ink is a critical requirement for inkjet printing technology. As mentioned in a previous section, the nozzle diameter limits the maximum particle size. NMC622, cathode active material, was supplied in a granulometry range, which was unsuitable for inkjet printing. As a reminder: the particle size of powders should be at least 50 times smaller than the nozzle diameter. Therefore, our goal is to get D90 (the particle size at which 90% of the total sample is smaller than that size) below 1 µm. Information on the particle size distribution and morphology of NMC622 powder are provided in Chapter 2. In order to meet the requirements of IJP process, grinding techniques are employed as a pre-processing step of ink formulation.

First, the effectiveness of three different grinding techniques is analyzed. As the target size is in the submicron range, the study is restricted to wet milling routes [203]. Planetary ball milling, attrition milling, and high energy ball milling, which are frequently mentioned in the literature for similar applications, are compared. The milled NMC622, with a particle size suitable for IJP, is structurally and electrochemically characterized. The structural changes within the materials are compared using XRD analysis. Modified Scherrer formula, Williamson-Hall (W-H), and Size-Strain Plot (SSP) methods are used to estimate the average crystallite size and lattice strain. Finally, the study explores the potential for restoring the initial properties of the milled powders through thermal treatments.

3.1 Comparison of various milling techniques

There are various factors that influence the selection of suitable grinding methods. The foremost consideration is the desired particle size. The final fineness of the powder largely depends on the milling method employed, particularly the impact energy, which denotes the energy transferred from the grinding media to the material being milled [204].

Three milling techniques were tested: planetary ball milling, attrition milling, and high energy ball milling. Chapter 2 provides details regarding the equipment that were used in our study. Among them, the high energy ball mill is the most powerful, while the planetary ball mill is the least efficient. This disparity directly influences the processing time, as a greater energy input shortens the required grinding time. Nevertheless, there is a greater likelihood of powder contamination with higher energy input. Conversely, when the energy input is reduced (such as by using a planetary ball mill), a longer duration is necessary to attain the desired fineness, which can also increase the likelihood of contamination [205]. Therefore, a compromise between the energy input and the impurity risk must be found. In addition, an extended grinding time may create the opposite effect from the one intended, as the particles tend to re-aggregate and re-increase in size rather than decrease. When the grinding time is prolonged, the friction between the powder particles and the grinding media during the process results in the generation of heat. The elevated temperature can cause the powder particles to become adhesive and stick together, leading to the formation of larger clusters or agglomerates [206].

Apart from the type of milling technique and grinding time, there are many other factors that may impact the final particle size, such as the grinding medium (shape, size, material), solvent, the rotation speed, and the ball-to-powder volume ratio The process parameters were optimized for each method, and the most noteworthy outcomes are presented.

Table 3.1: Optimal milling parameters for planetary ball milling, attrition ball milling, and high energy ball milling.

Trial	Technique	Ball size diameter	Total milling time	Rotational speed (rpm)	Ball-to-powder volume ratio
1	Planetary ball milling	10mm	4h	350	2:1
2	Planetary ball milling	800 µm	4h	350	2:1
3	Attrition ball milling	800 µm / 500 µm	8h	1000	4:1
4	Attrition ball milling	3mm / 500 µm	6h	1000	4:1
5	High energy ball milling	800 µm / 100 µm	20min	1700	4:3

Isopropanol was employed as the solvent for all experiments, and BYK-9076 (BYK) was added as a dispersing agent to enhance the milling efficiency. Grinding media comprised zirconium oxide balls of different diameters. At regular time intervals, the particle size is analyzed by laser diffraction. Grinding is stopped when the particle size does not significantly decrease with milling time. Once no further reduction in particle size was apparent, the milling process was stopped. Table 3.1 presents the optimal process parameters for 5 trials, which showed the most satisfactory results.

Starting with planetary ball milling, grinding balls of 10 mm and 800 µm in diameter were tested. In both cases, after 4 h of milling, a further reduction in particle size was not observed. Figure 3.1 shows the particle size distribution of raw and planetary ball-milled NMC622 powders. Finer balls (800 µm) effectively increased the process efficiency, resulting in D90 ∼ 4.4 µm, while larger balls produced D90 ∼ 9.3 µm. None of the performed trials allowed us to achieve the goal (D90 below 1 µm). Therefore, more energetic techniques had to be tested.

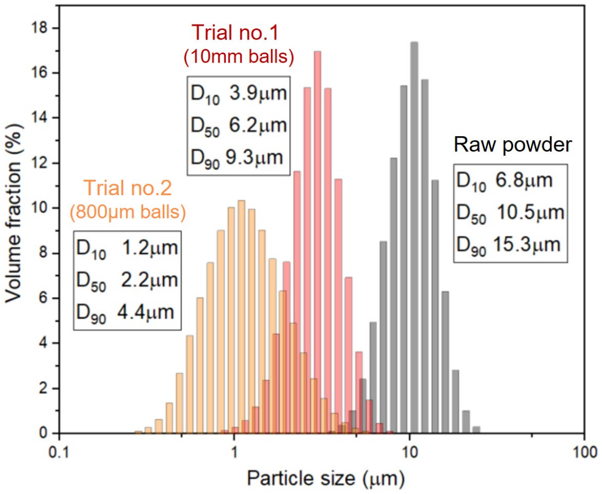

Figure 3.1: Particle size distributions of ball-milled NMC622 powders.

The process of attrition ball milling consisted of two steps, the first involving the use of larger size balls, and the second involving the grinding with smaller size balls. Using two different sizes of grinding balls helps achieve efficient and effective particle size reduction. The larger grinding balls used are more effective at breaking down larger particles, while the smaller balls used in the second stage can then further refine the particle size distribution and break down any remaining larger particles or agglomerates. This cascading effect enhances the overall milling efficiency.

Figure 3.2 shows the particle size distribution of powders milled with 2 configurations: a) 800 µm / 500 µm balls, b) 3 mm / 500 µm balls. The total time of milling was 8 h (4 h with 800 µm balls + 4 h with 500 µm balls), and 6 h (4 h with 3 mm balls + 2 h with 500 µm balls), for trial no. 3 and trial no. 4, respectively. No significant difference was observed in the final D90 between these 2 experiments, but the particle size distribution was much more narrow for trial no. 4. The final values of D90 were still greater than 1 µm.

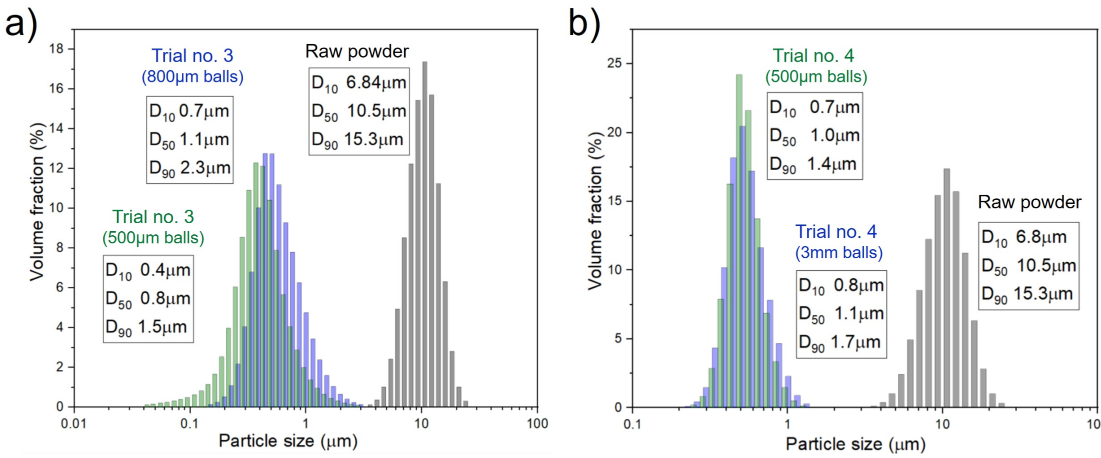

Figure 3.2: Particle size distributions of NMC622 powders after attrition milling: a) 800 µm / 500 µm balls, b) 3mm / 500 µm balls.

High energy ball milling was performed in 2 steps, same as attrition milling trials. The most satisfactory results were obtained using balls of 800 µm (10 min), then 100 µm (10 min). The total grinding time was only 20 minutes. Particle size distributions of milled powders are shown in Figure 3.3. Only after the first milling step, the particles were finer than after the two stages of the attrition process. The second step with 100 µm balls enabled us to achieve the goal. D90 of high energy ball milled NMC622 totaled around 0.8 µm.

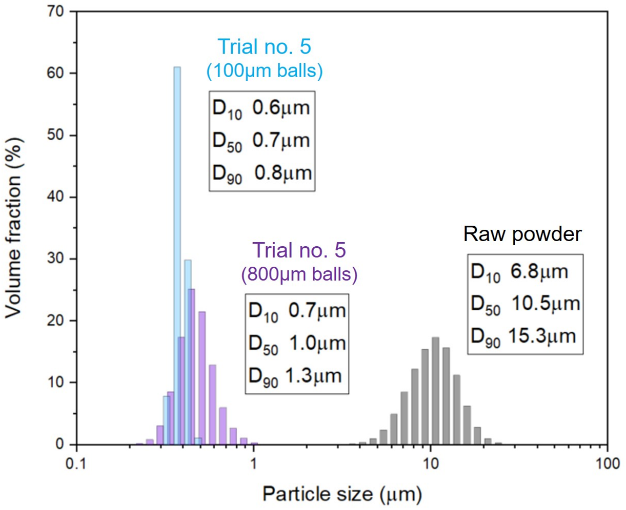

Figure 3.3: Particle size distributions of high energy ball-milled NMC622 powders.

Planetary ball milling tests showed that using smaller grinding balls led to the production of finer particles. This is because they created smaller and more numerous points of contact between the grinding balls and the material being milled. Additionally, smaller grinding balls were able to access smaller spaces between particles, allowing for a complete size reduction of the material being milled.

Attrition milling showed the opposite effect, as larger balls proved to be more efficient in reducing particle size. Nevertheless, it is crucial to take into account the grinding time, as it contributes to the generation of heat. In trial no. 4, despite the utilization of larger balls, finer particles were achieved in comparison to trial no. 3. However, the milling duration was 2 hours shorter. It is reasonable to speculate that the extended duration led to elevated temperatures, which in turn facilitated the re-agglomeration of the powder.

Planetary ball milling and attrition milling could not provide enough kinetic energy of balls to reduce the particles below 1 µm. With high energy ball mill, the goal was achieved. Moreover, the milling process took only 20 minutes, compared to a few hours with other techniques. Therefore, after high energy ball milling, NMC622 powder met the requirements of IJP in terms of particle size. Nevertheless, the contamination of the powder after processing should be verified, for instance, by ICP spectroscopy. Unfortunately, due to confidentiality reasons established by UMICORE, this analysis could not be performed.

The next question we should ask was, "How does milling impact the powder's crystal structure and electrochemical performance?"

3.2 Structural and electrochemical powder properties

3.2.1 Impact of milling

This section focuses solely on the examination of high energy ball-milled NMC622 powder, as it conforms to the required specifications for IJP. For simplicity, in the further part of this Chapter, high energy ball-milled NMC622 powder is denoted simply as milled NMC622.

The morphology of raw and milled NMC622 powders is depicted in Figure 3.4. The originally perfectly spherical particles were transformed into irregular shapes after grinding.

The crystal structure of milled NMC622 was compared to that of raw powder. XRD patterns are presented in Figure 3.5. As a result of the milling, the doublets (108)/(110) and (006)/(102) merged, indicating a loss of the layered structure. Additionally, the I(003)/I(104) ratio varied following the grinding process. This ratio serves as an indirect measure of the degree of cation mixing between Li^+ and Ni^{2+} ions in the lithium layer [207]. The presence of Ni^{2+} ions in the lithium layer leads to a decrease in discharge capacity impeding Li^+ ionic diffusivity. These structural irregularities are widely recognized as the primary cause of deteriorated electrochemical characteristics [74]. The theoretical I(003)/I(104) ratio, which corresponds to a perfect structure without any Li in transition metal sites and vice versa, is influenced by temperature, valence, composition, and other parameters [208].

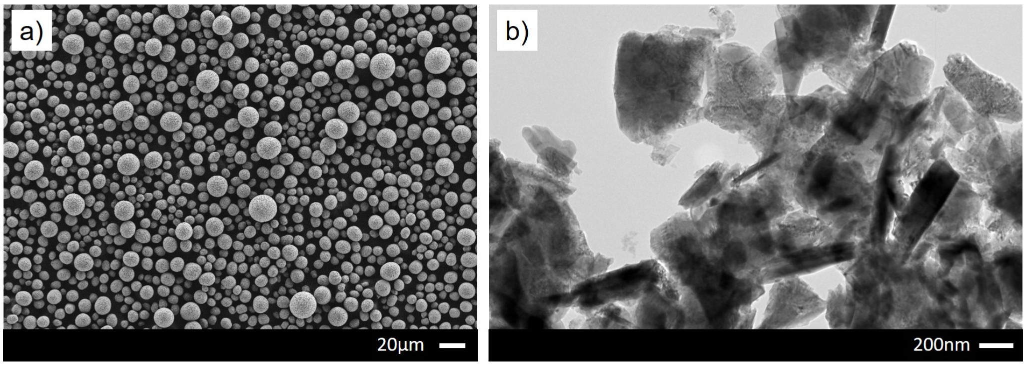

Figure 3.4: a) SEM image of raw NMC622 powder, b) TEM image of high energy ball-milled NMC622 powder.

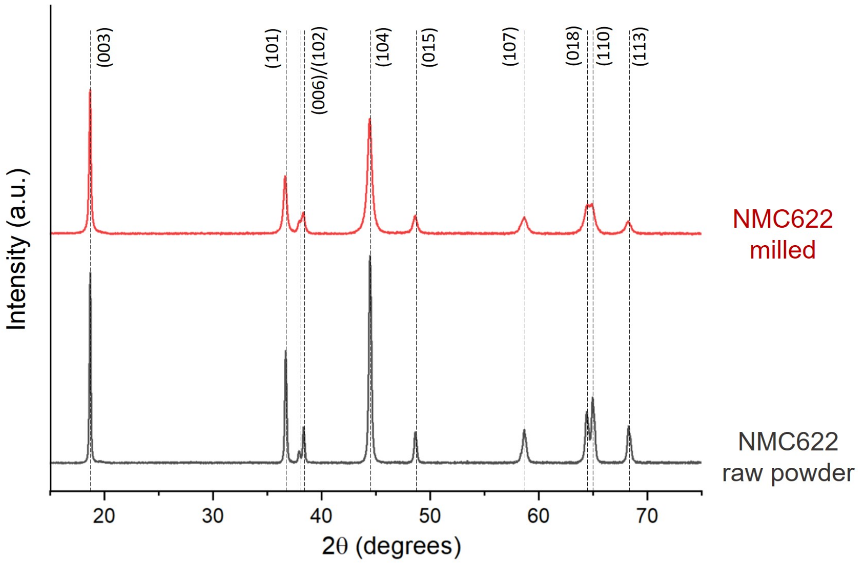

Figure 3.5: XRD patterns of raw and high energy ball-milled NMC622 powders.

In this study, the I(003)/I(104) ratio did not change significantly after milling. Values of raw and milled particles were found around 0.5. This observation suggested that the grinding did not affect so much the degree of cation mixing in the structure. This finding contrasts with the study conducted by Pan *et al.* [207], who demonstrated that ball milling reduced this ratio.

Another qualitative indication of the structural ordering is the R-factor, represented as [I(006)+I(102)]/I(101), which estimates the system's hexagonal ordering. The hexagonal ordering increases as the R-factor decreases [209]. For raw powder, its value was 0.43, while after milling, it reached 0.60.

Therefore, it could be assumed that NMC6222 experienced a crystal structure disorder due to grinding. In the next step, we wanted to verify how these structural changes impacted the electrochemical performance of the powder.

Electrochemical tests were performed with electrodes fabricated by tape casting. The cathode slurry consisted of 80 wt% of active material (raw NMC622 or milled NMC622), 10wt% of carbon black, and 8wt% of PVDF in NMP. Electrodes were deposited on Al foil, punched at a diameter of 14 mm, calendared for 30 s at 10 T, and vacuum dried at 60°C for 48h. The coin cells were assembled in a glovebox with metallic lithium counter electrode, polypropylene separator Celgard 2500, and 150 µL liquid electrolyte (LPX: $LiPF_6$ at 1M in mixture of EC/DMC/EMC [1:1:1]). Cycling tests were conducted at a constant current ranging from 3.0 V to 4.3 V at a temperature of 25°C. The initial two cycles, known as the formation cycles, were performed at a current rate of 0.1C. Following the formation cycles, additional cycles were carried out at a current rate of 1C. Between each cycle, 5 min open circuit voltage was recorded. The C-rates were calculated based on the maximum theoretical NMC622 capacity of 190 mAh/g.

EIS was performed after the two first formation cycles.

Figure 3.6a represents the first charge and discharge curves (formation) for cells based on milled and reference NMC622 powders, using a low C-rate of 0.1C. The cells built of reference NMC622 exhibited similar charge/discharge curves, with a plateau at ∼3.6V, which corresponds to the redox transition of Ni^{2+}/Ni^{4+} [210]. With milled NMC622, the discharge profile was significantly different from the charge curve. It rapidly shifted toward lower potentials, displaying a distinct voltage decrease. Additionally, the charge curve of milled NMC622 demonstrated a plateau at a slightly higher potential when compared to the reference NMC622 profile. The findings indicated that electrodes composed of milled NMC622 display considerable polarization, which might arise from the disorder in the crystal structure.

Figure 3.6b illustrates the discharge capacity of the cells as a function of the cycle number after the formation process performed at 1C. A significant decrease in discharge capacity was observed after the milling, with the reference NMC622 exhibiting a capacity of ∼170 mAh/g, whereas the milled NMC622 demonstrated only ∼72 mAh/g. Moreover, the milled powder suffered from poor capacity retention, with only 44% retained after 100 cycles, while the reference material maintained 94% of its initial capacity.

Given the limitations of the coin cell setup (Li-metal counter electrode, no reference electrode), it was important to consider only approximately 100 cycles for a reliable analysis. This was due to the fact that 1C rate corresponds to a relatively high current density (0.4-0.5 mA/cm^2), which is likely to induce morphological changes in the Li metal electrode and gradually deplete the electrolyte. Notably, the detrimental effects of these phenomena, such as increased polarization and capacity loss, become evident only after a significant number of cycles (typically 50-100 cycles).

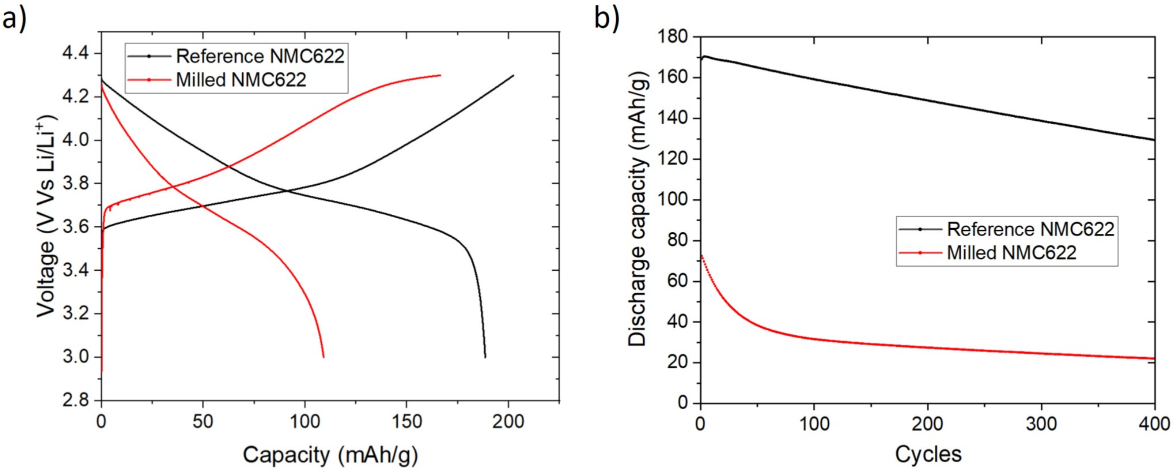

Figure 3.6: a) First charge and discharge curves at 0.1C for cells based on reference and milled NMC622 powders, b) Discharge capacity versus cycle number at 1C for cells built of reference and milled NMC622 powders.

Figure 3.7 shows the impedance spectra of cells built of reference and milled NMC622 powders in the Nyquist plot, and the Bode magnitude plot.

The Nyquist plot consists of a semicircle in the high and middle frequency region, and Warburg tail at low frequency. The semicircle represents the charge transfer resistance of interfaces between the active materials and the electrolyte, while the Warburg tail demonstrates the Li-ion diffusion in the active materials or electrolyte [211], [212].

The milled NMC622 cell exhibited a smaller semicircle diameter in comparison to the reference material, indicating a higher charge transfer resistance for the latter. On the other hand, the milled powder demonstrated a larger slope of the Warburg tails, implying that the grinding process led to increased resistance for Li-ion diffusion.

It might suggest that finer particles shortened the diffusion path length of ions, facilitating the charge transfer. Furthermore, they had a larger surface area per unit volume of the cathode material, resulting in a better contact between the electrode and the electrolyte. Consequently, the electrochemical reactions at the electrode-electrolyte interface can occur more efficiently, reducing charge transfer resistance.

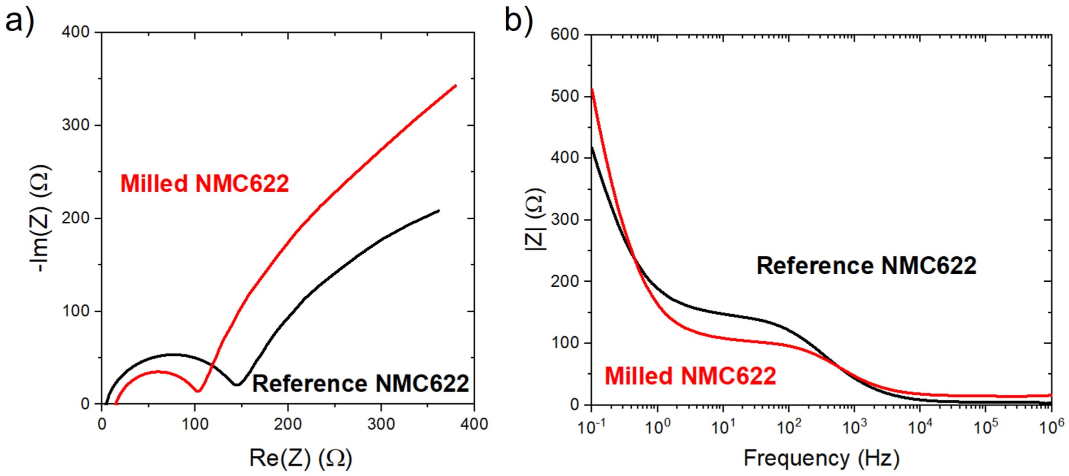

Figure 3.7: Electrochemical impedance spectroscopy (EIS) curves of cells built of reference and milled NMC622 powders: a) Nyquist plot, b) Bode plot. The measurements were performed after the two first formation cycles.

However, the milled NMC622 exhibited higher Li-ion diffusion resistance within the electrodes and electrolyte. This could be attributed to the structural disorder present in the crystal structure, which hampered the movement of Li ions. In a well-ordered crystal structure, the pathways for Li-ion diffusion are clear and well-defined, allowing for efficient and rapid movement of ions during charge and discharge cycles. However, when there is a structural disorder, such as cation mixing, vacancies, or lattice distortions, the diffusion pathways become more convoluted and obstructed.

Therefore, while smaller particle sizes can be advantageous for charge transfer, the presence of structural disorder limits the diffusion of ions within the material.

The findings were confirmed by analyzing the Bode magnitude plot, which illustrates the correlation between the input frequency and the impedance magnitude of the system. At frequencies below 0.5 Hz, corresponding to the region where ion diffusion predominantly takes place, the impedance of the cell containing the milled powder was observed to be higher. In the mid-frequency range of 0.5-1000 Hz, which is associated with charge transfer resistance, the cell with the reference NMC622 material exhibited higher impedance values.

To sum up the section, in agreement with the observations of Pan *et al.* [207], the milling process significantly deteriorated the electrochemical properties of NMC622. The change in crystal structure might be one of the potential reasons for the decline in electrochemical performance. However, changes in the surface groups could also be another contributing factor (formation of $-$OH groups, carbonatation of the surface, anchoring of the dispersing agent at the particle surface...), and it should be studied in the future.

3.2.2 Impact of thermal treatment

To alleviate the effect of these assumptions, thermal treatment of the milled powders was proposed in order to try to recover the initial properties of NMC622. The annealing process was carried out at temperatures of 350°C, 400°C, and 500°C in air atmosphere. Another thermal treatment in O_2 was also conducted at 500°C. These atmospheres were chosen instead of an inert atmosphere because a low partial pressure of oxygen might cause the loss of elements containing oxygen. Zheng *et al.* demonstrated that oxygen non-stoichiometry in Ni-rich NMC materials is destructive to the electrochemical performance. Because Ni could be reduced from Ni^{3+} to Ni^{2+}, higher cationic disorder would be produced, limiting the lithium-ion transport [213].

Figure 3.8 demonstrates XRD patterns of NMC622 powders after thermal treatments compared to those of raw and milled material. No improvement in recovering the layered structure was observed.

The doublets that were observed at $2\theta=38°$ and $2\theta=65°$ for NMC622 without annealing, were no longer visible; instead, there were single broad peaks. An increase in the annealing temperature caused the shift of peaks, which confirms a distortion in the crystal lattice. This effect was observed mainly for the plane (104) and doublets of planes (018)/(110). Generally, the peak shift towards a lower 2θ value is attributed to the expansion of the crystal lattice, which is related to microstructural parameters (crystallize size and lattice strain) [214].

The I(003)/I(104) ratios of NMC622 powders before and after annealing are presented in Table 3.2. The values were lower for powders after thermal treatments. This suggested that there was a potential increase in the Ni ion concentration within the structure, possibly attributable to a loss of lithium.

Table 3.2: I(003)/I(104) ratios of NMC622 powders before and after annealing.

Powder	I(003)/I(104) ratio
Raw powder	0.54
Milled	0.57
Milled + thermally treated (350°C, air)	0.22
Milled + thermally treated (400°C, air)	0.21
Milled + thermally treated (500°C, air)	0.27
Milled + thermally treated (500°C, O_2)	0.39

This hypothesis is supported by the apparition of peaks for 2θ between 20° and 35°, which corresponded to Li_2CO_3 (marked stars). This peak appeared whatever the atmosphere used. The thermal treatment in O_2 did not eliminate the impurity peaks on the XRD pattern (Figure 3.8). Although carbon was eliminated from the annealing environment in

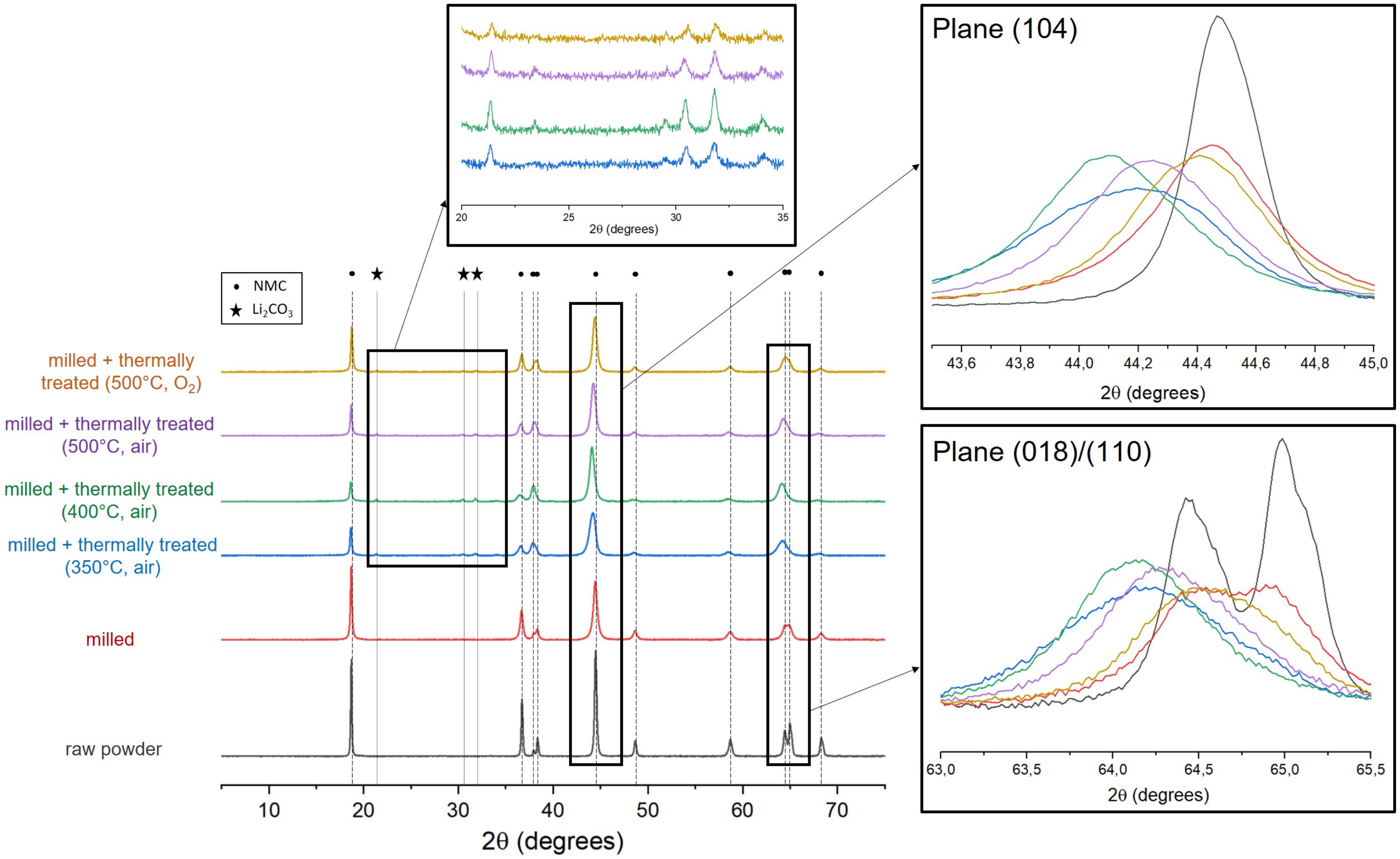

Figure 3.8: XRD patterns of NMC622 powders: raw powder, after milling, and after thermal treatments.

O_2 atmosphere, it could be present on the surface of the particles before the treatment. This phase formation could then be promoted by the dispersant and the solvent used in the grinding process. It was reported that the presence of carbonates and oxides on the surface of NMC materials leads to deteriorated electrochemical performance, as ionic and electronic conductivity decrease and particles become more isolated [215].

Figure 3.9 represents the first charge and discharge curves (formation) for cells built of milled and thermally treated NMC622 powders, using a low C-rate of 0.1C. For powders treated in air atmosphere, the discharge profiles rapidly shifted toward lower potentials, while the curve of NMC622 annealed in O_2 remained relatively stable. Consequently, the powder treated in O_2 demonstrated the lowest polarization. This observation suggested that the annealing process has the potential to partially restore the layered structure of the material.

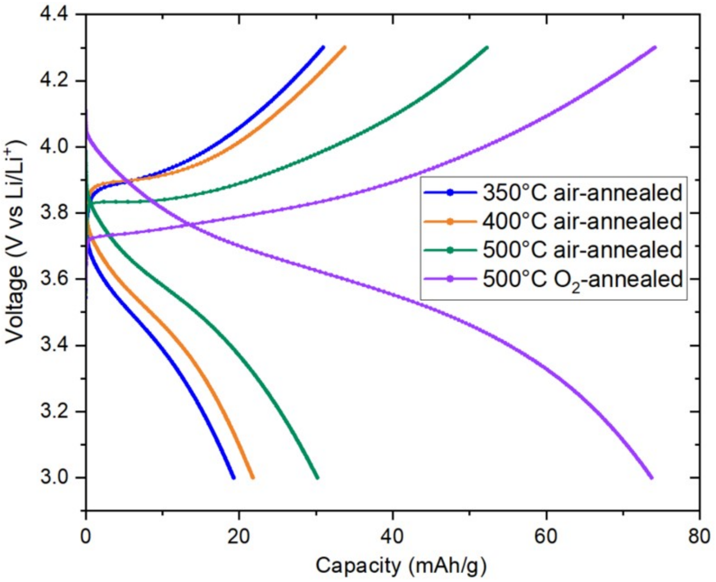

Figure 3.9: First charge and discharge curves at 0.1C for cells built of milled and thermally treated NMC622 powders.

Figure 3.10 shows the discharge capacity versus cycle number for NMC622 powders after milling and thermal treatments. For powders annealed in air atmosphere, the results indicated a significant decline in the performance compared to the milled NMC622 without annealing. At the initial cycle, the discharge capacity of powders annealed at temperatures of 350°C, 400°C, and 500°C reached approximately 20 mAh/g, 20 mAh/g, and 28 mAh/g, respectively.

After 100 cycles, the powders treated at 350°C and 400°C maintained around 52% of the initial capacity, while the one annealed at 500°C showed a capacity retention of only around 39%.

Figure 3.11 illustrates the relationship between discharge capacity and cycle number for the

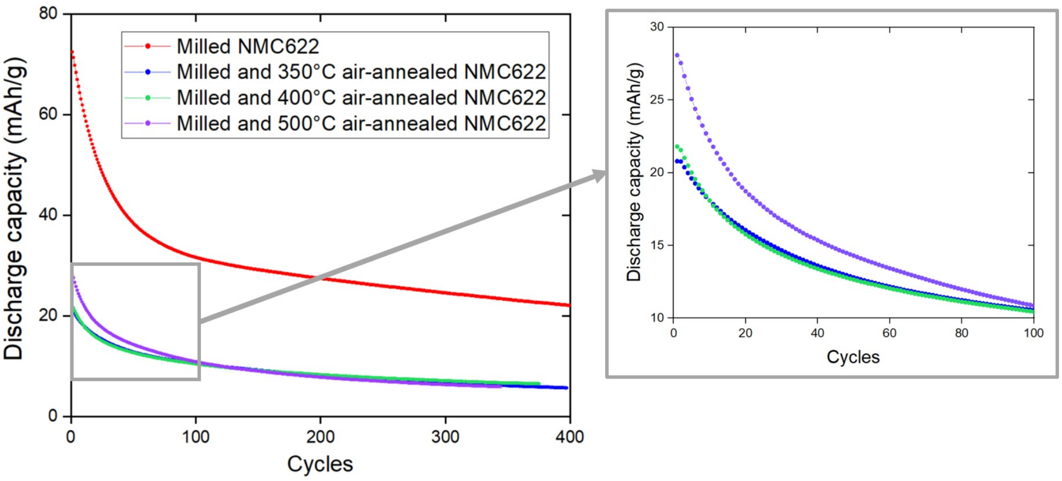

Figure 3.10: Discharge capacity versus cycle number at 1C for cells built of NMC622 powders after milling and thermal treatments in air atmosphere.

powder treated in O_2 at 500°C. During the initial cycle, the capacity reached approximately 72 mAh/g, which was comparable to the discharge capacity of the milled NMC622 without any annealing. After 100 cycles, the powder demonstrated a capacity retention of 50%.

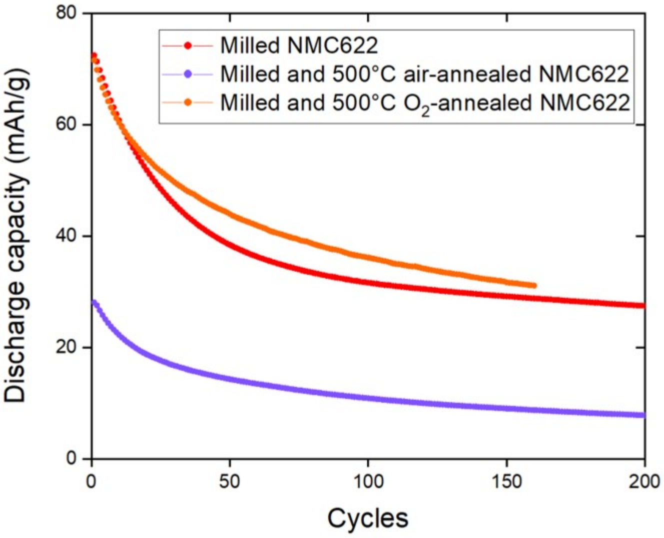

Figure 3.11: Discharge capacity versus cycle number at 1C for cells built of NMC622 powders after milling and thermal treatments in 0_2 atmosphere.

3.2.3 A comparative study of crystallite size and microstrain

To gain a more comprehensive understanding of the changes in the crystal structure, an analysis of XRD peak broadening was performed. XRD peaks can become broadened due to limitations of the equipment, microstrain, and decrease in crystallite size. When the crystallites in a material are small, there are fewer atoms present in each one. Consequently, the intensity of the diffracted X-ray beam decreases, and the beam is scattered over a larger range of angles, leading to broader XRD peaks [216]. Broadening of XRD peaks may also arise from imperfections or irregularities within the crystal lattice. The existence of defects, such as vacancies or dislocations, can disrupt the regularity of the lattice, causing a wider range of diffracted angles. These structural imperfections are directly associated with microstrains [217].

In our study, the average crystallite size and microstrains of powders were estimated by Modified Scherrer equation, W-H analysis, and SSP methods. However, the results should be analyzed prudently, as cation mixing and loss of atoms were observed, impacting the shape of XRD peaks. For ease of calculation, dimensionless shape factor K was taken as 0.9, which is the most common value used when particle morphologies are unknown [218]. A discussion on K may be found in the interesting article of Langford *et al.*[219]. The X-ray wavelength (λ) was 1.5406 Å.

Modified Scherrer Method

The well-known Scherrer formula considers the effect of crystallite size as the only origin of the XRD peak broadening [220] and is given as:

$$D = \frac{K\lambda}{\beta_D \cos\theta} \tag{3.1}$$

where D is the average crystallite size, K is a dimensionless shape factor, λ is the X-ray wavelength, β_D represents Full Width at Half Maximum (FWHM) of a particular peak, and θ is angle of peak position. The equation 3.1 can be rewritten as:

$$\cos\theta = \frac{K\lambda}{D}\left(\frac{1}{\beta_D}\right) \tag{3.2}$$

When plotting $\frac{1}{\beta_D}$ along the x-axis, and $\cos\theta$ along the y-axis, the average crystallite size can be calculated from the slope of the linear fitted curve [221]. However, the Scherrer equation shows an error. With an increase in $\beta_D \cos\theta$, smaller crystallite sizes are obtained, but normally all the peaks should give a similar value. In order to decrease the error, the Modified Scherrer equation was proposed and is discussed in detail in the article [220]. By making logarithm on both sides of the Scherrer equation (Eq. 3.1), the following relation is obtained:

$$\ln \beta_D = \ln \frac{K\lambda}{D} + \ln \frac{1}{\cos\theta} \tag{3.3}$$

After plotting $\ln \beta_D$ on the y-axis, and $\ln \frac{1}{\cos\theta}$ on the x-axis, the average crystallite size can be calculated from the intercept ($\ln \frac{K\lambda}{D}$) of the linear fitted curve [222]. The modified Scherrer plots are presented in Figure 3.12.

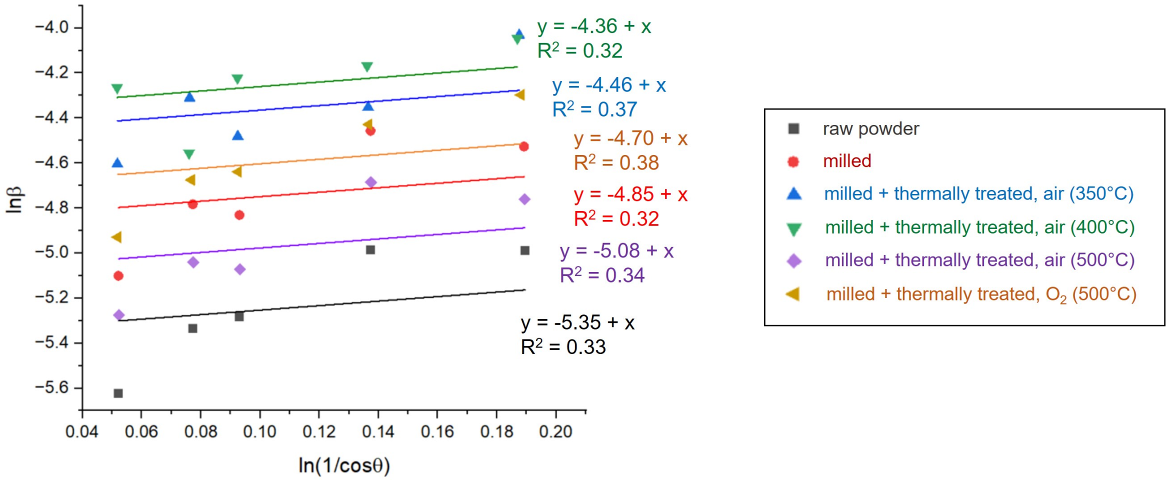

Figure 3.12: Modified Scherrer plots for NMC622 raw, milled and thermally treated powders.

Our data did not fit well with the linear regression model of the Modified Scherrer Method, as indicated by the low values of R-squared (R^2) (R-squared values are in between 0 to 1, with 1 indicating the best fit). The reason for the poor alignment could be due to the fact that this method solely takes into account the crystallite size as the source of peak broadening. However, it appears that other factors also had an impact on the shape of XRD patterns.

Williamson-Hall analysis

Assuming that the strain is being distributed evenly across the entire crystal structure, Williamson-Hall Uniform Deformation Model (UDM) can be used to estimate strain in a lattice structure [223]. The foundation of the theory is the fact that the XRD peak broadening comes from both crystallite size and microstrain [224]. Broadening caused by the crystallite size can be calculated from the Scherrer equation, as presented before, while broadening from the microstrain (β_S) is given by the equation:

$$\beta_S = 4\varepsilon \tan\theta \tag{3.4}$$

where ε is microstrain.
The equation for the sum of broadenings (β) from the crystallite size and microstrain can be written as follows:

$$\beta = \beta_S + \beta_D = \frac{K\lambda}{D\cos\theta} + 4\varepsilon\tan\theta \tag{3.5}$$

and after a simple conversion:

$$(\beta\cos\theta) = \varepsilon(4\sin\theta) + \frac{K\lambda}{D} \tag{3.6}$$

which gives the equation of simple linear regression, where y = β cos θ, x = 4 sin θ, and $\frac{K\lambda}{D}$ is the y-intercept.
Therefore, after plotting 4sin θ on the x-axis, and β cos θ on the y-axis (Figure 3.13), the slope of the line gives the microstrain, while the average crystallite size can be calculated from the y-intercept (β can be expressed as the FWHM of a peak).

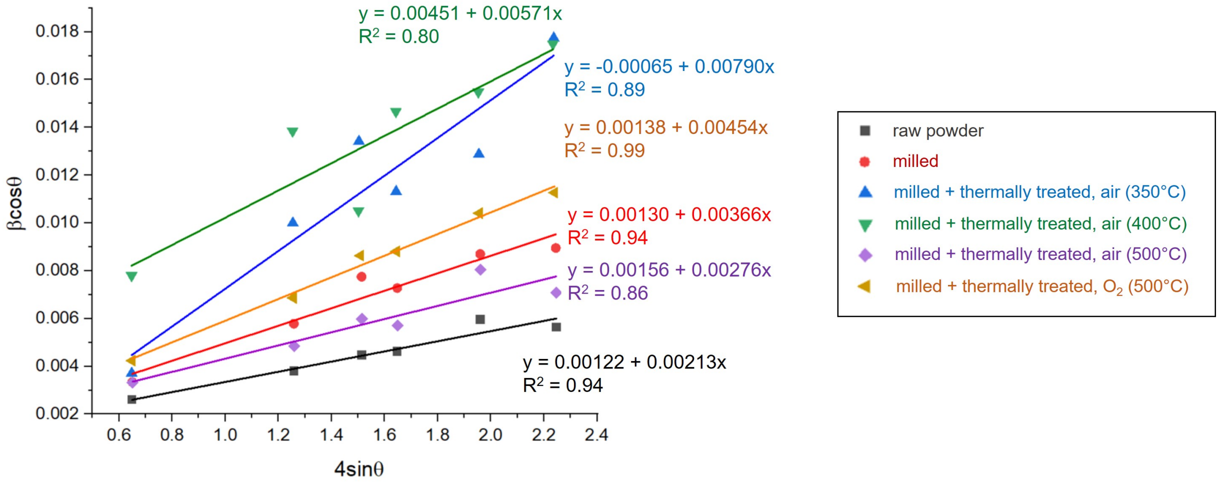

Figure 3.13: Williamson Hall plots for NMC622 raw, milled and thermally treated powders.

Compared to the Modified Scherrer Analysis, the Williamson-Hall method showed significantly better fitting, which is obvious from the relatively high values of R^2 values. Therefore, microstrains present in the crystal structure essentially contributed to peak broadenings.

Size-Strain plot

Size-Strain Plot (SSP) is another method which enables the estimation of microstrain and average crystallite size. Here, less importance is given to the data from high-angle peaks, where the accuracy is usually low [222]. SSP method is based on the following relation:

$$(d_{hkl}\beta\cos\theta)^2 = \left(\frac{K}{D}\right) d_{hkl}^2\beta\cos\theta + \left(\frac{\varepsilon}{2}\right)^2 \tag{3.7}$$

where d_{hkl} is the interplanar distance that can be calculated by the Bragg law. Plotting $(d_{hkl}\beta\cos\theta)^2$ on the y-axis, and $d_{hkl}^2\beta\cos\theta$ on the x-axis (Figure 3.14), the crystallite size can be taken from the slope, and the microstrain may be estimated from the intercept of the linear fitted curve.

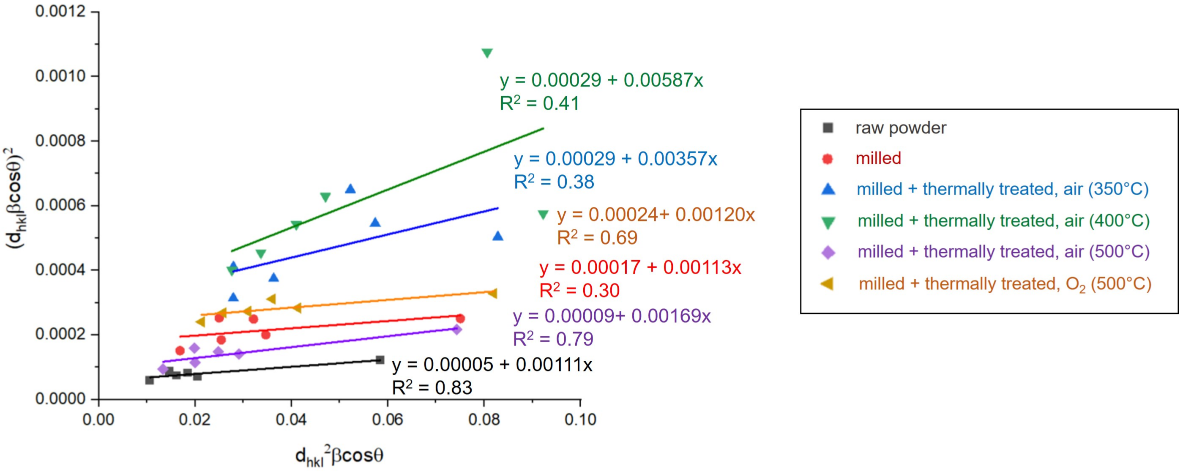

Figure 3.14: Size-Strain plots for NMC622 raw, milled and thermally treated powders.

The fit obtained from SSP method is comparatively poor, despite the fact that this analysis considers both the crystallite size and microstrain as factors contributing to peak broadening. The mathematical formula failed to adequately describe the variations observed in NMC622 powders.

Table 3.3 displays the average crystallite size and microstrain for raw, milled, and thermally treated powders, estimated by the different methods. Because the Modified Scherrer plot only takes into account the size-related broadening, the resulting estimates of crystallite size obtained using this technique tended to be much lower than those obtained using the SSP and W-H analyses. Microstrain together with average crystallite size was estimated by SSP and W-P approaches. As the W-H method showed a negative intercept for the powder treated at 350°C, which is physically meaningless, it was excluded from further discussion.

Table 3.3: Characteristics of NMC622 powders.

Powder	Average crystallite size (nm)			Microstrain	
	Modified Scherrer plot	W-H	SSP	W-H	SSP
Raw powder	29	114	81	2.1	1.5
Milled	18	107	80	3.7	2.6
Milled + thermally treated (350°C, air)	12	-	25	-	3.4
Milled + thermally treated (400°C, air)	10	31	15	5.7	3.4
Milled + thermally treated (500°C, air)	22	89	53	2.8	1.9
Milled + thermally treated (500°C, O_2)	15	100	75	4.5	3.1

The data fit was unsatisfactory, particularly for the Modified Scherrer plot and SSP methods, and there were notable disparities among the results obtained from the three techniques. However, all analyses indicated the same trend, illustrated in Figure 3.15. While the calculated values for crystallite sizes and microstrains should not be regarded as accurate, this study provided insights into the changes in the crystal structure caused by milling and thermal treatment.

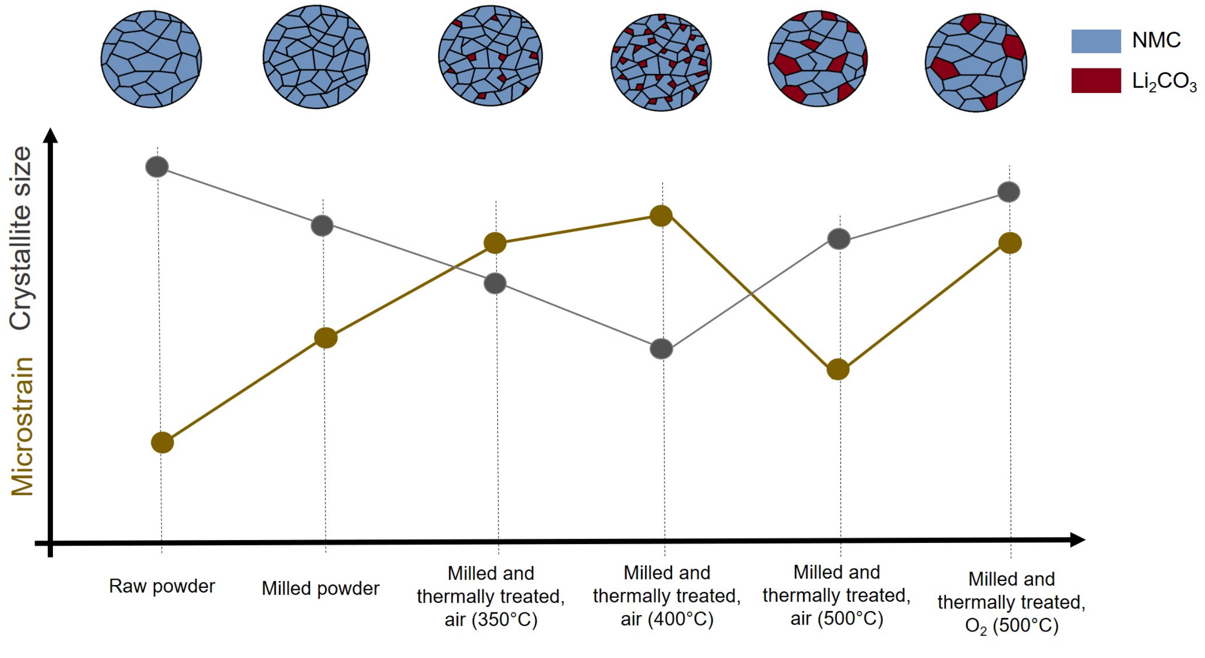

Figure 3.15: Schematic representation of changes in crystal structure induced by high-energy ball milling and thermal treatment.

The raw powder yielded the largest crystallite size and lowest microstrain. After milling, grain refinement and an increase in microstrains were observed. Grinding could introduce microstrain in a material due to the mechanical stress and deformation induced during the process. The high-pressure forces might cause local distortions and misalignments in the crystal lattice and also the creation of new surfaces.

Subjecting the material to a thermal treatment of 350°C resulted in a reduction in size and an increase in microstrain, which can be attributed to the creation of the Li_2CO_3 phase. This led to the formation of small new grains within the NMC phase, resulting in a decrease in the average size of the crystallites. The accumulation of crystal defects could be the reason for the increased microstrain.

The material treated at 400°C exhibited a comparable level of strain but with smaller crystallites. This may suggest the emergence of additional grains containing the Li_2CO_3 phase.

Raising the temperature to 500°C caused a slight increase in crystallite size and a decrease in microstrain. This could be attributed to the acceleration of atomic diffusion, which promoted faster grain growth in both phases and facilitated structural relaxation.

Powder treated at 500°C in oxygen atmosphere showed larger crystallites and higher strain compared to the material treated at the same temperature but under normal air.

This might be due to a limited amount of carbon resulting in the formation of less Li_2CO_3 phase, which in turn led to a larger average crystallite size. As fewer grain boundaries were created, it could be presumed that there was limited defect annihilation at grain boundaries, resulting in a larger number of defects and consequently higher microstrain.

Besides it should be noted that the impact of various annealing atmospheres on the kinetics of phase transformation could also provide an alternative explanation for the observed results. However, this particular topic is beyond the scope of the current study.

3.3 Granulometry of treated powders

The particle size distributions of powders after the thermal treatments were analyzed. The results are presented in Figure 3.16. Elevated temperature caused the growth of the grains but also could promote the bonding of the particles (sintering). An increase in annealing temperature correlated with an increase in particle size. Therefore, even if the thermal treatment would help in recovering the initial crystal structure, the powders would no longer be suitable for IJP process.

3.4 Conclusions

Among the three grinding techniques that were tested, high energy ball milling proved to be the most efficient method for milling NMC622 powder. The particle size D90 was reduced to less than 1 micron in 20 minutes, which was significantly faster than other methods that took several hours and still did not yield satisfactory outcomes.

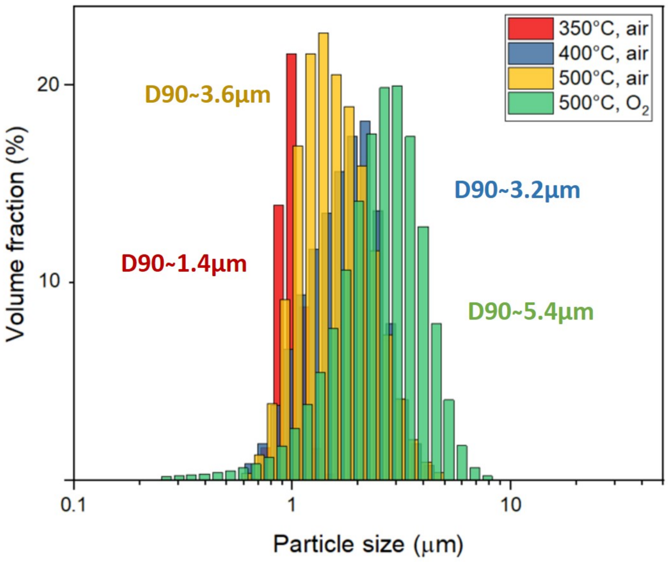

Figure 3.16: Particle size distributions of NMC622 powders after thermal treatments with different temperatures.

However, the grinding step led to the deterioration of the crystal structure of NMC622, resulting in poor electrochemical performance, in agreement with previous obsevations [207]. According to XRD analyses, this could be caused mainly by crystal defects, and consequently induced lattice microstrain in the structure of NMC622.

In order to improve the electrochemical performance of the milled powder, it was proposed to relax microstrains in the structure by different thermal treatments. However, the initial structure of NMC622 was not recovered. Additionally, the new impurity phase Li_2CO_3 appeared. The discharge capacity of annealed powders was significantly reduced compared to that of raw material. However, NMC622 treated at 500°C showed slightly better electrochemical performance than materials annealed at lower temperatures. It might suggest that the thermal process could recover the layered structure to some extent, but total structural reconstruction was impossible. Moreover, Li_2CO_3 impurity might decrease ionic and electronic conductivity, negatively impacting the electrochemical performance. This study confirmed that the grinding of active materials can have a significant impact on electrochemical performance. Specifically, for NMC622, grinding was observed to have a detrimental effect on the electrochemical properties. When nanopowders are required for electrode shaping, as is the case of inkjet printing, it is recommended to purchase NMC raw powders with suitable granulometry to maintain optimal electrochemical performance. Since NMC622 with a smaller particle size, was not commercially available, NMC333 was purchased from SigmaAldrich instead. Despite having a lower capacity, this material had an average particle size of 400 nm and was utilized for further studies.

Moreover, the results highlighted the importance of the choice of suitable mixing methods when preparing the electrode slurry. Particular attention has to be paid to minimize damage to the NMC structure following the grinding process.

Summary:

- High energy ball milling was the most efficient method for milling NMC622 powder, reducing particle size to less than 1 micron in just 20 minutes.
- The grinding of NMC622 resulted in a deterioration of its crystal structure, leading to poor electrochemical performance. XRD analyses revealed a decrease in hexagonal ordering, cation mixing, loss of oxygen and lithium atoms, crystal defects, and lattice microstrain as possible causes.
- Thermal treatments were proposed to try to restore the initial properties of NMC622 powder. The original structure was not fully recovered, and an impurity phase of Li_2CO_3 appeared, potentially impacting conductivity and electrochemical performance.
- To address the challenges associated with grinding and thermal treatments, synthesizing NMC622 powder within the appropriate granulometry range was suggested to eliminate the need for pre-processing.
- As commercially available NMC622 with smaller particle size was not accessible, NMC333 with an average particle size of 400 nm was purchased from SigmaAldrich as an alternative. Despite having a lower capacity, NMC333 was used for further studies due to its smaller particle size.

4

Inkjet printing of anode for LIBs

Summary

FORMULATION of stable water-based anode inks, specifically designed for inkjet printing (IJP), but also adaptable for other wet-processing techniques is covered in detail in this chapter. Silicon and silicon coated by carbon nanoparticles, which can withstand significant deformation strains without the mechanical fracture of the electrode, are used as active materials. This Chapter addresses the difficulties encountered in developing printable anode inks for IJP and assesses the electrochemical performance of these ink formulations. Inks containing carbon-coated silicon nanoparticles and PEDOT:PSS result in electrodes that attain the cutoff lithiation capacity of 2000 mAh g^{-1} with no observed capacity degradation over time. In contrast, anodes composed of pure silicon demonstrate a capacity decay after 75 cycles, proving the advantages of utilizing a Si/Carbon core-shell structure. The printability tests are presented, revealing the instabilities of the drop generation process, and the importance of particle surface chemistry. Furthermore, we present microstructural analyses of the printed patterns. Lastly, we tackle the concern of particle emissions during ink preparation and inkjet printing, demonstrating that these processes pose no harm to human health.

4.1 Ink formulation and characteristics

4.1.1 Anodes composition

Nanopowders of silicon (Si) (BET surface area: 50 m^2/g) and silicon coated by carbon (SiΩC) (BET surface area: 60 m^2/g), both with an average particle size of 40 nm were used as an active material for the formulation of anode functional inks. Super P Carbon Black (CB) (BET surface area: 57-67 m^2/g) of average particle size of 40nm was added as a conductive agent. Sodium carboxymethyl cellulose (CMC) of $M_w \sim 90000$ g/mol, CMC of $\mathrm{M}_w \sim 700000\,\mathrm{g/mol}$, and poly(3,4-ethylenedioxythiophene)-poly(styrenesulfonate) (PEDOT:PSS) were used as binders. An active material, conductive agent, and binder in the ratio of 50:25:25 by weight were dispersed in deionized water (DI-water) with the dispersing agent Triton X-100.

The composition of the slurries for tape-casting was adapted by reducing the solvent content. The ratio of active material to conductive agent to binder was kept fixed. To prevent the cracking of CMC-based anodes, Duramax B-1000 acrylic latex (Rohm and Haas) in the quantity of 9wt% was added to the formulations. PEDOT:PSS was tested at its natural pH of 1.7, as well as at the pH level of 10.

4.1.2 Ink preparation

As mentioned in the introduction section, well-dispersed ink is essential for IJP. In order to avoid nozzle clogging, agglomeration and sedimentation of powders must be effectively limited. Therefore, well-thought-out formulation process is necessary.

In the first step of anode ink preparation, zeta potential versus pH was measured for Si, SiΩC, and CB powders, which enabled establishing which range of pH is the most suitable for the formulation. Plots in Figure 4.1 demonstrate a significant negative zeta potential for all powders when the pH values exceed 6. No significant difference in surface charge was observed between Si and SiΩC powders.

However, it is important to acknowledge the presence and influence of a binder. CMC has a pH $\sim$ 7, which does not significantly affect the surface charge of the powder particles. The pH of the inks prepared with CMC was 6.7. However, using PEDOT:PSS as an alternative binder can pose a problem due to its acidic nature, with a pH of around 1.7. The addition of 25wt% of PEDOT:PSS to the ink resulted in a pH of 3.2, leading to rapid agglomeration and settling of the powder. To address the issue, NaOH (0.1M) was added to the formulation, in order to increase the basicity, and consequently, to improve stability. As a result, the final pH of the inks formulated with PEDOT:PSS reached 10.3.

Although Si and SiΩC exhibited high stability in water, this only applied to highly diluted suspensions (for instance, 0.5wt% of powder in water). When increasing the amount of Si/Si$\varOmega$C, agglomerates were formed, indicating unstable dispersion. In addition, particles can also display hydrophobic characteristics, causing the particles to repel water and agglomerate together [225]. To ensure that particles remain discrete and to help overcome the hydrophobicity, a dispersing agent Triton X-100 was added to the formulation. The surfactant was selected via simple sedimentation experiments. Triton X-100 showed satisfactory results for all powders, Si, Si$\varOmega$C, and CB. Using one kind of dispersant helps

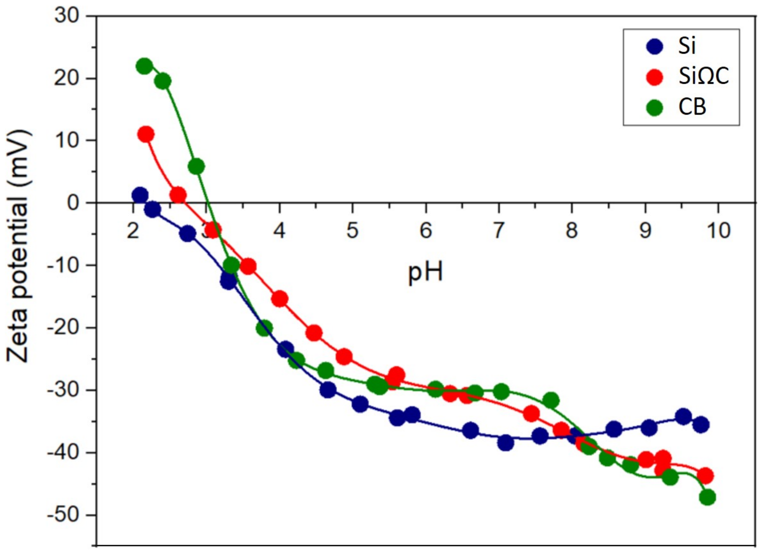

Figure 4.1: Zeta potential as a function of pH for Si, SiΩC, and CB powders measured using Zetasizer Nano ZS.

to avoid the risk of unwanted interactions between ink components.

The optimal amount of the dispersing agent was evaluated by viscosity measurements using microfluidic rheometer Fluidicam RHEO. A set of suspensions (1.5wt% of powder in DI-water) with various concentrations of the dispersant was analyzed The results are presented in Figure 4.2. As the concentration of dispersing agent increases, the viscosity of the dispersion should decrease, indicating better dispersion of powder particles in the water. The concentration at which the viscosity reaches a minimum represents the optimal amount of dispersing agent required to achieve stable dispersion. The optimal concentration values were 10wt%, 30wt%, and 50wt% for SiΩC, Si, and CB, respectively. The use of the high amount of Triton X-100 might be surprising, but it can be rationalized by the need to evenly coat the very large surface area of the nanoparticles in order to prevent clumping. Similar observations have been reported in previous studies [226].

After acquiring the information, all the components were carefully mixed together. Binders were dissolved in DI-water by magnetic stirring. Si/SiΩC and CB were dispersed with DI-water and the optimal amount of Triton X-100 using the high-speed disperser. Afterward, both of the mixtures were combined and put in an ultrasonic bath for a minimum of 1h. The composition of formulated inks is presented in Table 4.1. For ease, in this work, we denote the formulations as shown in the first column, *i.e.* INK_SiΩC_CMC, and INK_SiΩC_PEDOT, INK_Si_CMC, INK_Si_PEDOT. In the study, numerous inks were prepared with various solvent-to-powders ratios, and they were optimized using

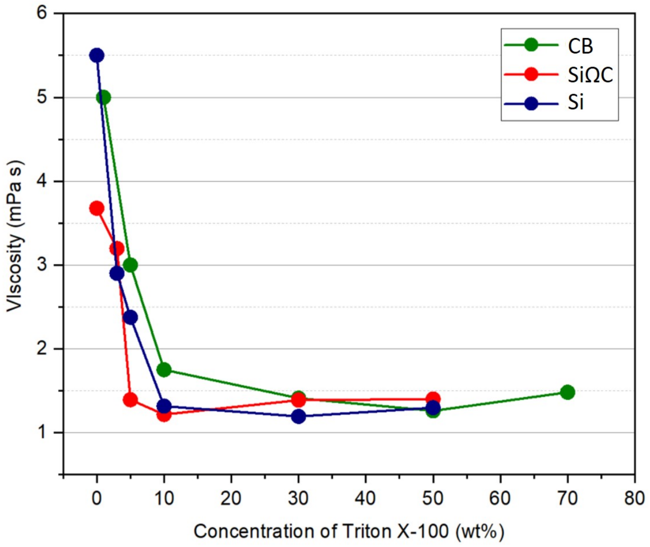

Figure 4.2: Optimization of dispersant concentration: viscosity as a function of Triton X-100 concentration for Si, SiΩC, and CB (1.5wt% of powder in DI-water). The measurements were performed using microfluidic rheometer Fluidicam RHEO.

a trial-and-error method. Here, we present only examples of formulations, which were optimal in terms of stability and printability. It should be noted that inks with CMC of M_w~700 000 were also formulated but their high viscosity made them unsuitable for IJP. Therefore, they were not considered for further analysis in this study.

4.1.3 Inks characterization

To determine the Z values of the formulated inks, the viscosity, surface tension, and density were measured. The viscosity as a function of the shear rate was evaluated using Discovery Hybrid Rheometer HR-2 (TA Instruments) with double wall concentric cylinders geometry. The surface tension was tested by the tensiometer DCAT21 (Dataphysics) with a platinum Wilhelmy plate. To measure the density, a known volume of ink was weighted on a precision scale (Denver). For all the tests, the temperature was set to 20°C. The measured values and calculated Z value are presented in Table 4.1. The given values of viscosity refer to the one at the share rate of 100 s^{-1}, and Figure 4.3 illustrates how the viscosity varies for the range from 10 to 1000 s^{-1}. For each ink, slightly shear thinning behavior was observed, which is the most noticeable for INK_SiΩC_PEDOT. The decrease in viscosity with the shear rate guarantees the ink passing easily through the nozzle during printing.

For the record, the manufacturer of the inkjet printer used in our work recommends formulating inks with a viscosity between 5 and 20 mPa.s, and surface tension from 30 to 35 mN/m. Z value should lie between 1 and 10. Although viscosities of INK_SiΩC_CMC,

Table 4.1: Composition and characteristics of formulated anode inks designed for IJP.

Nomenclature	Composition	Solvent	Surface tension (mN/m)	Viscosity at 100^{-1} (mPa.s)	Density (g/ml)	Z	pH
INK_SiΩC_CMC	SiΩC+CB+CMC	DI-water	32.1	3.3	0.74	~10	6.7
INK_SiΩC_PEDOT	SiΩC+CB+PEDOT:PSS	DI-water+NaOH	32.3	8.2	0.76	~4	10.1
INK_Si_CMC	Si+CB+CMC	DI-water	32.1	3.4	0.72	~10	6.7
INK_Si_PEDOT	Si+CB+PEDOT:PSS	DI-water+NaOH	32.3	4.5	0.75	~8	10.2

INK_Si_CMC, and INK_Si_PEDOT were lower than what is required, Z values of these inks were in the printable range.

The stability of the anode inks was evaluated using Turbiscan LAB and by sedimentation tests. Figure 4.4 shows the profiles of backscattered and transmitted lights as a function of the sample height. The inks were scanned each 10 min for 1 h. The results of the sedimentation tests are presented in the same Figure. Suspensions were photographed at the beginning of the experiment and after 1 and 24 h.

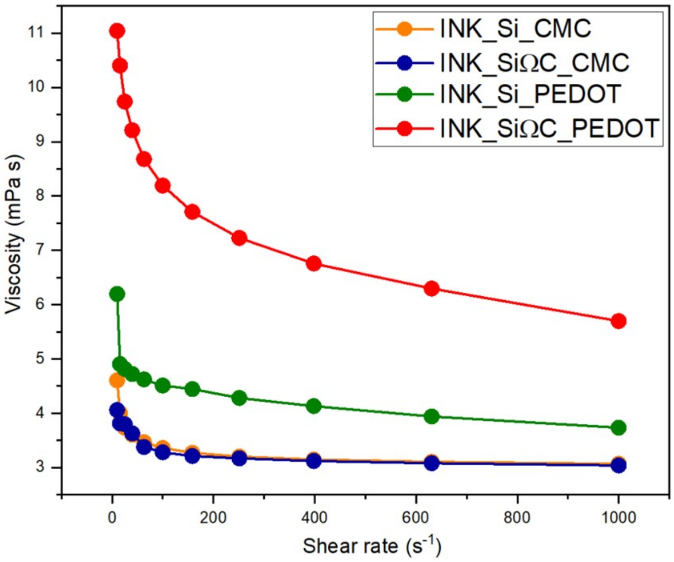

Figure 4.3: Viscosity as a function of shear rate for INK_SiΩC_CMC, INK_SiΩC_PEDOT, INK_Si_CMC, INK_Si_PEDOT. The measurements were performed using Discovery Hybrid Rheometer HR-2.

The transmission profiles demonstrated that for all inks, no supernatant was formed after one hour, which was further verified by sedimentation tests. The decrease of the backscattered lights with time gave evidence for particle agglomeration, even though sediment formation was not apparent. It was particularly observed for INK_Si_CMC, INK_SiΩC_CMC, and INK_Si_PEDOT. INK_SiΩC_PEDOT exhibited very high stability with constant backscatter levels over time.

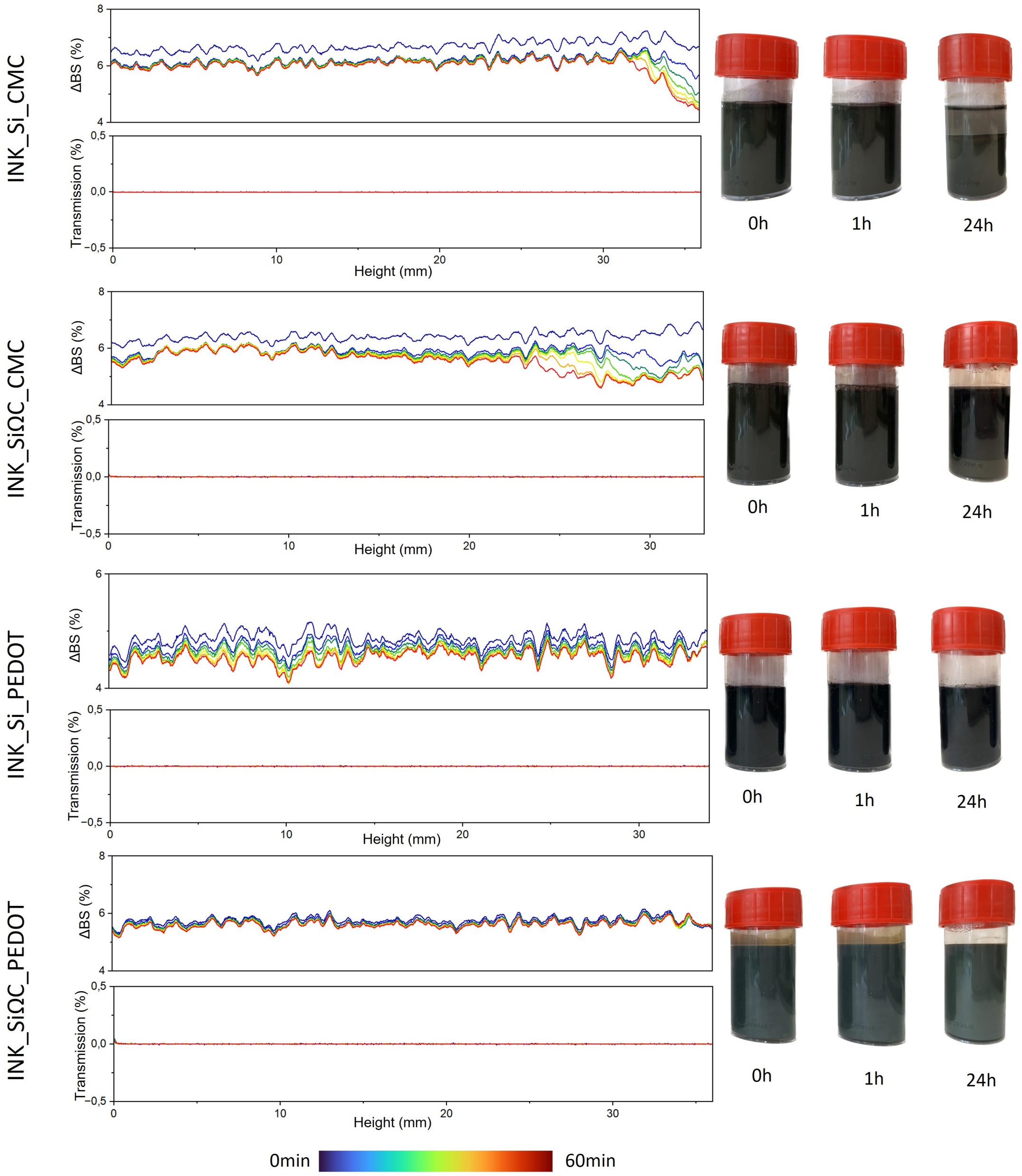

Figure 4.4: Stability analysis of anode ink formulations: the results of Turbiscan analyses (backscattering and transmission profiles measured during 1h with 10 min of intervals), and sedimentation tests for formulated anode inks.

Based on the sedimentation tests, it was obvious that only inks containing PEDOT:PSS remained stable after 24 hours. INK_Si_CMC underwent sedimentation, with the supernatant being observed. Similarly, sedimentation was noticeable in INK_SiΩC_CMC, but only the SiΩC particles settled, while CB remained suspended in the water.

Although the stability of formulated inks after 24h may be considered unsatisfactory, it was sufficient for IJP. Minimal changes were observed in the suspensions during the first hour. Additionally, to prevent excessively large agglomerates during the process, all the inks were filtered through 1.2 µm filters before printing.

4.1.4 Electrochemical characteristics

To evaluate how the ink formulations affect the anode's performance, electrochemical tests were conducted on tape-casted electrodes.

Formulations with a different kind of CMC were developed. In literature, it was demonstrated that higher molecular weight of CMC may result in more favorable electrochemical performance of silicon anode [227], [228]. For IJP, CMC with a relatively low molecular mass of 90 000 g/mol had to be used due to the need for low viscous ink. For the sake of comparison, anodes with CMC of M_w 700 000 g/mol were fabricated and electrochemically tested.

As previously discussed, in order to achieve a stable suspension formulated with PEDOT:PSS as a binder, it was necessary to adjust its pH (see Section 4.1.2, page 108). This modification resulted in different polymer structures. At low pH (natural pH of PEDOT:PSS), the polymer created a connected network, while at the high value (pH $\sim$ 10), separated clusters were observed (Figure 4.5).

These observations might suggest that the modified pH level negatively impacts the electrochemical performance of the anode. The disconnected structure of an electrode could hinder efficient electron and ion transport, contributing to lower capacity, reduced cycling stability, and shorter overall battery lifespan. Therefore, the anode formulated with PEDOT:PSS as a binder, but without the pH adjustment was also tested.

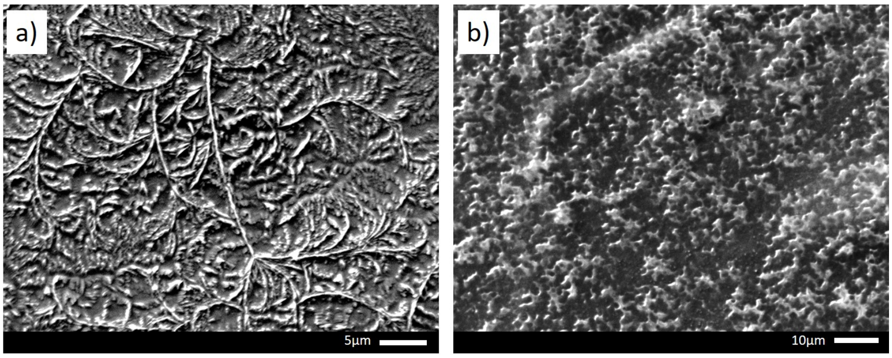

Figure 4.5: SEM images of PEDOT:PSS at different pH levels: a) pH$\sim$1.7 (natural pH of PEDOT:PSS), b) pH$\sim$10.

The compositions of all tested anodes are presented in Table 4.2. In order to minimize the number of tests, a limited quantity of samples was selected for evaluation. The chosen set of electrodes aimed to assess the influence of the binder and active material on the electrochemical performance.

For slurries prepared with PEDOT:PSS, the ratio between active material, conductive agent, and binder was 50:25:25, the same as for inks. Such prepared slurries created uniform layers on the copper foil (see Figure 4.6a).

For the preparation of tape-casted electrodes with CMC, latex Duramax B-1000 had to be added to the formulations. Otherwise, the anodes were cracked after drying, as presented in Figure 4.6b. Latex added to slurries resulted in the formation of uniform layers that were free of any visible flaws (Figure 4.6c).

Figure 4.6: Photographs of tape casted anodes with different compositions: a) SiΩC as active material, PEDOT:PSS as binder, b) SiΩC as active material, CMC of M$_w$ 90 000 as binder, c) SiΩC as active material, CMC of M$_w$ 90 000 as binder + 9wt% of latex Duramax B-1000.

Table 4.2: Compositions of anode slurries used for fabrication of tape-casted electrodes.

Nomenclature	Active material	Binder	Conductive agent	Additives
SiΩC_CMC_90k	45.5 wt% SiΩC	22.75 wt% CMC M$_w$ 90 000	22.75 wt% CB	9 wt% Latex
SiΩC_CMC_700k	45.5 wt% SiΩC	22.75 wt% CMC M$_w$ 700 000	22.75 wt% CB	9 wt% Latex
Si_CMC_700k	45.5 wt% Si	22.75 wt% CMC M$_w$ 700 000	22.75 wt% CB	9 wt% Latex
SiΩC_PEDOT_nat	50 wt% SiΩC	25 wt% PEDOT:PSS (natural pH)	25 wt% CB	-
SiΩC_PEDOT_mod	50 wt% SiΩC	25 wt% PEDOT:PSS (modified pH)	25 wt% CB	-
Si_PEDOT_nat	50 wt% Si	25 wt% PEDOT:PSS (natural pH)	25 wt% CB	-

CB - Super P Carbon Black, Latex - Duramax B-1000 acrylic latex, PEDOT:PSS (natural pH) - PEDOT:PSS at pH of 1.7, PEDOT:PSS (modified pH) - PEDOT:PSS at pH of 10.

Casted silicon anodes were heated at 80 °C for 16 h in vacuum to remove adhesive moisture. Then, three specimens per anode type were die-cut (12 mm diameter) and used for the construction of CR2032 coin cells with metallic lithium counter electrode (14 mm diameter), two borosilicate glass fiber separators, and 150 µL liquid electrolyte (0.9M LiPF$_6$ in 45 vol% ethylene carbonate, 45 vol% dimethyl carbonate, 10 vol% fluoroethylene carbonate). The cells were temperature-equilibrated for 22 h at 30°C before cycling them with a constant current of 0.05C four times (formation) and subsequently 100 times with 0.2C using cutoff voltages of 10 mV (lithiation) and 1.0 V (delithiation) with a BaSyTec cell test system (Basytec GmbH, Asselfingen, Germany). Between each cycle, 5 min open circuit voltage was recorded. The charging rate was calculated assuming a maximum capacity of the silicon active material of 3580 mAh/g, whereas lithiation was stopped at 2000 mAh/g for enhanced reversibility, in case the cutoff voltage criterion was not met.

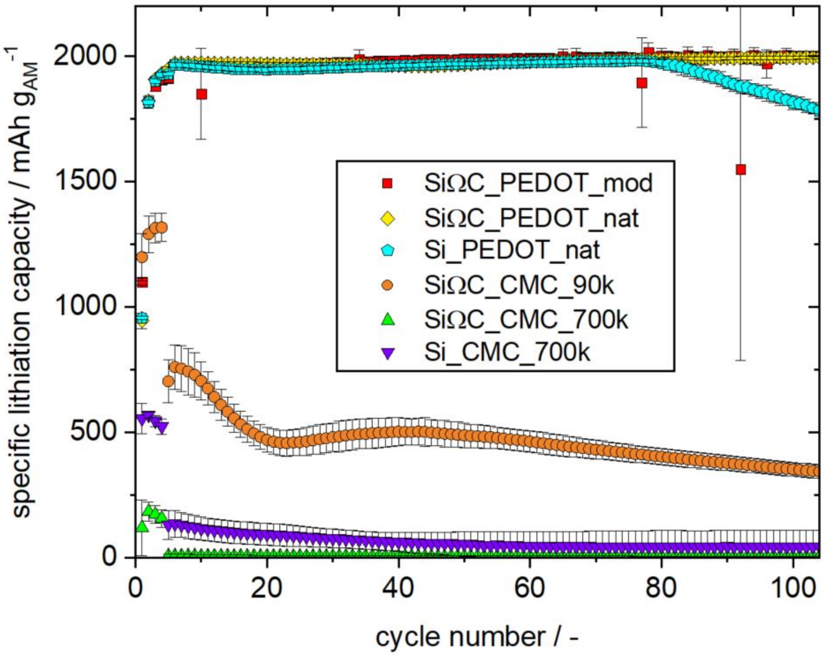

Figure 4.7: Specific discharge capacity versus cycle number at 0.05C (4 initial cycles), and 0.2C (100 cycles) for tape-casted anodes. The measurements were performed at 30°C.

PEDOT:PSS-based samples performed best, attaining the cutoff lithiation capacity of 2000 mAh g^{-1} right after the formation (Figure 4.7). The pH variation of the PEDOT:PSS solution did not significantly affect the results. The carbon-silicon composite active material SiΩC did not show capacity fading, in contrast to the silicon-based specimen, whose capacity declined from the 75th cycle onward by circa 20% at cycle 104. The sudden drop can be attributed to the limitation of cycling to 2000 mAh g^{-1}. During the initial 75 cycles, a portion of the silicon was irreversibly consumed, but it was subsequently replenished with fresh silicon due to a significant unused capacity range between 2000 and 3580 mAh g^{-1}. These observations proved that carbon-coated silicon anodes offer improved stability. The carbon coating acted as a protective layer, mitigating the detrimental effects of volume expansion and improving the stability and structural integrity of the electrode. Furthermore, the carbon coating likely led to the minimized formation of SEI, creating a barrier between the silicon and electrolyte. This allowed for better electrolyte penetration

and improved cycling stability [229].
CMC/Latex-based samples exhibited much lower lithiation capacities, whereas the low molecular weight CMC reached higher values. This might result from a diffusion limitation due to the encapsulation of active material in the lowly lithium-ion conducting binder or latex matrix, which is evidenced by the capacity loss upon the increase of the lithiation rate. Moreover, it is important to take into account the presence of the high amount of Triton X-100, which could also contribute to the reduction of lithium ion diffusion. However, it should be acknowledged that these electrodes were fabricated only for comparison purposes between different ink formulations designed for IJP. When appropriately tailored, CMC-based anodes built of Si or SiΩC nanopowders from Nanomakers can provide satisfactory electrochemical properties [230].

4.2 Printability tests

Although the cycling performance of electrodes formulated with CMC was poor, the ink formulations corresponding to these electrodes were considered in the subsequent part of the study. It has been mentioned earlier that the unsatisfactory electrochemical results could be attributed to the presence of latex, which can be excluded from the ink compositions designed for inkjet printing applications. In IJP technique, the material is deposited in the form of small droplets placed adjacent to each other. Consequently, the drying conditions for the printed structure differ from those of tape-casted electrodes. This controlled approach gives sufficient time for the ink to dry and reduces the build-up of stress within the deposited layers, minimizing the likelihood of cracking. Therefore, the addition of latex may be unnecessary for the inks tailored for IJP, and the printability tests were conducted on all the formulated inks (see Table 4.1).

4.2.1 Inks with SiΩC

Figure 4.8 presents the results of printability tests for INK_SiΩC_CMC. The optimal electric pulse design ensuring a stable drop generation process includes $t_{rise} = 2\,\mu s$, $t_{dwell} = 5\,\mu s$, $t_{fall} = 2\,\mu s$, and $V = 75\,V$ (Figure 4.8a). Below the value of 75 V, the ejection was not possible. As a result of an increase in the rising and falling time or the dwelling time, the droplet splits into two (Figure 4.8b,c). The same behavior was recorded when increasing the voltage up to 100V (Figure 4.8d,e,f). At the maximal value of 120V, jetting was unstable, with many irregular drops ejected at the same time (Figure 4.8g). All the tests were performed with a jetting frequency of 100 Hz.

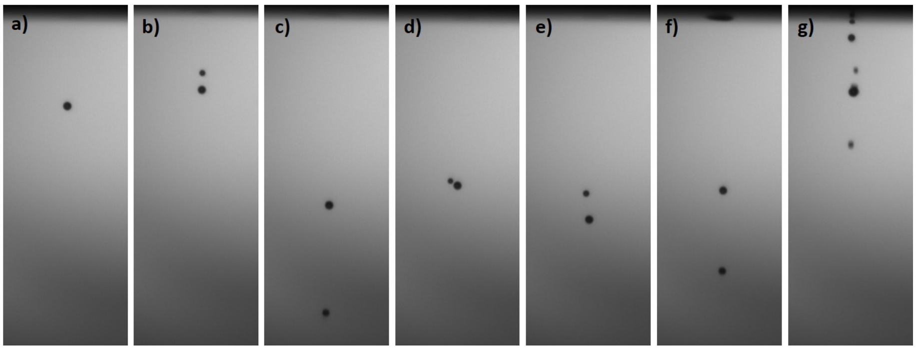

Figure 4.8: Printability test results for INK_SiΩC_CMC. The behavior of ink's droplets after exiting the nozzle for the following electric pulse designs (t$_{rise}$, t$_{dwell}$, t$_{fall}$, V): a) 2 µs, 5 µs, 2 µs, 75V; b) 5 µs, 5 µs, 5 µs, 75V; c) 2 µs, 10 µs, 2 µs, 75V; d) 2 µs, 5 µs, 2 µs, 80V; e) 2 µs, 5 µs, 2 µs, 85V; f) 2 µs, 5 µs, 2 µs, 100V; g) 2 µs, 5 µs, 2 µs, 120V.

The behaviors of INK_SiΩC_PEDOT after exiting the nozzle for different electric pulse designs are presented in Figure 4.9. All the experiments were performed at 100 Hz. Two sets of values were found as optimal, forming a stable drop: t$_{rise}$ = 1 µs, t$_{dwell}$ = 13 µs, t$_{fall}$ = 1 µs, V = 50 V (Figure 4.9a), and t$_{rise}$ = 5 µs, t$_{dwell}$ = 0 µs, t$_{fall}$ = 5 µs, V = 50 V (Figure 4.9b). Below 50 V, no ejection was observable. The modification of the values of time (Figure 4.9 c,d,e) or increase in the voltage (Figure 4.9 f,g,h,i) resulted in unstable jetting behaviors.

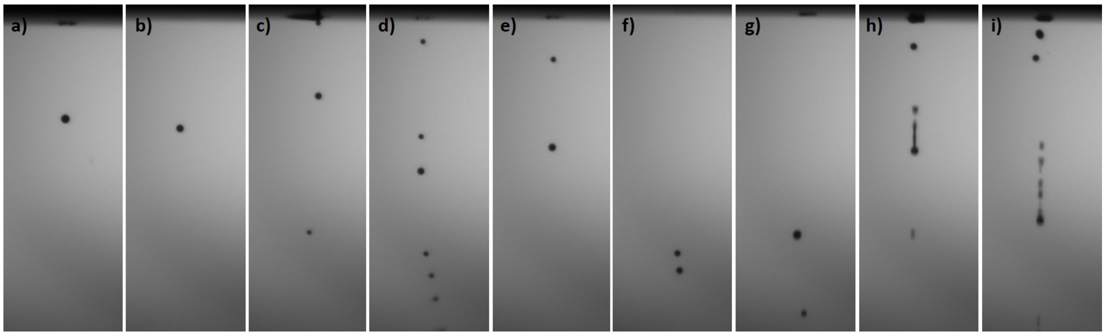

Figure 4.9: Printability test results for INK_SiΩC_PEDOT. The behavior of ink's droplets after exiting the nozzle for the following electric pulse designs (t$_{rise}$, t$_{dwell}$, t$_{fall}$, V): a) 1 µs, 13 µs, 1 µs, 50V; b) 5 µs, 0 µs, 5 µs, 50V; c) 5 µs, 1 µs, 5 µs, 50V; d) 5 µs, 2 µs, 5 µs, 50V; e) 5 µs, 5 µs, 5 µs, 50V; f) 5 µs, 0 µs, 5 µs, 60V; g) 5 µs, 0 µs, 5 µs, 80V; h) 5 µs, 0 µs, 5 µs, 100V; i) 5 µs, 0 µs, 5 µs, 120V.

The drop generation process with optimal parameters was registered as a function of time for INK_SiΩC_CMC (Figure 4.10a) and INK_SiΩC_PEDOT (Figure 4.10b). In both cases, the liquid flowed out from the nozzle, creating the main droplet with an attached filament. Subsequently, the filament was detached, and its tail end formed a second drop, which speeded up, and the two merged together.

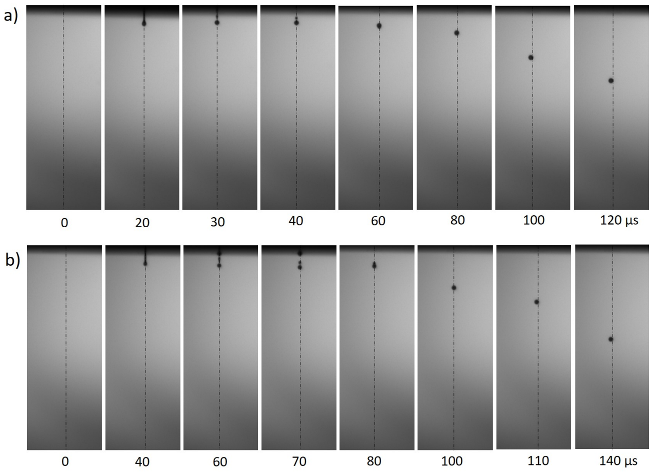

Figure 4.10: Drop generation process with optimal parameters registered as a function of time for:
a) INK_SiΩC_CMC; b) INK_SiΩC_PEDOT.

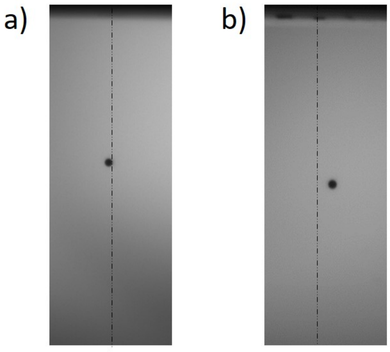

Figure 4.11: Deviation of INK_SiΩC_PEDOT droplet: a) at the beginning of ejection, b) after 5min of ejection.

Although jetting was achieved, there was a slight deviation of the drop trajectory from the nozzle axis (marked by dotted lines), which might result in poor printing quality. In addition, the deviation was not predictable. The droplets were subjected to shift in both directions to a different extent. The deflection presented in Figure 4.10 was not significant, but it worsened with printing time. For instance, figure 4.11 shows the deviation of INK_SiΩC_PEDOT droplet at the beginning and after 5min of ejection. It should be noted that apart from the extent, the direction of deflection was also changed.

The optimization of jetting frequency revealed the link between the jetting frequency value and the problem of nozzles' clogging. Figure 4.12 represents the INK_SiΩC_CMC ejection process as a function of time, with the optimal electric pulse when increasing the frequency. In the beginning (0 µs), 100 Hz was applied and immediately raised up to 1000 Hz. The jetting became instantly unstable, and after 5 s, the ink could not be ejected anymore. The test with INK_SiΩC_PEDOT showed the same phenomenon, only with a shorter ejection time. In this case, the nozzle was clogged after only 3 s.

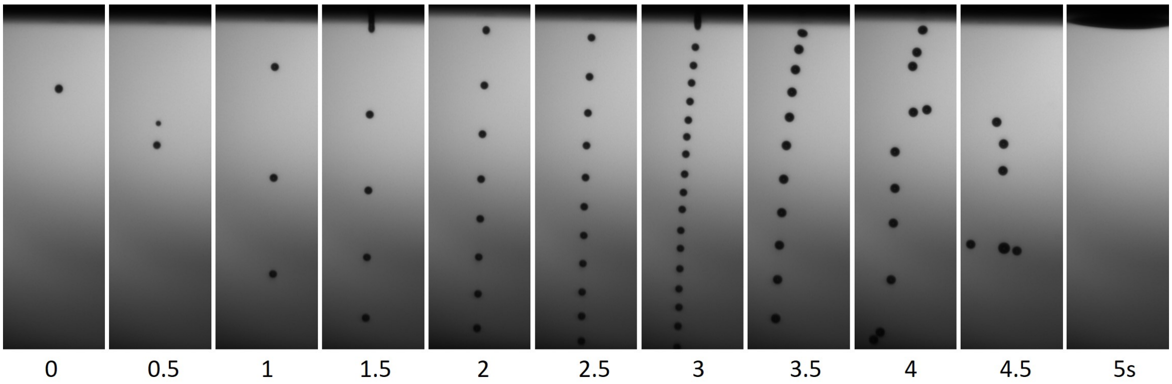

Figure 4.12: Ejection process as a function of time for anode ink INK_SiΩC_CMC when increasing jetting frequency from 100Hz to 1000Hz.

The percentage of clogged nozzles after 30 and 60s of ejection as a function of jetting frequency was calculated for INK_SiΩC_CMC and INK_SiΩC_PEDOT. The results are presented in Figure 4.13.

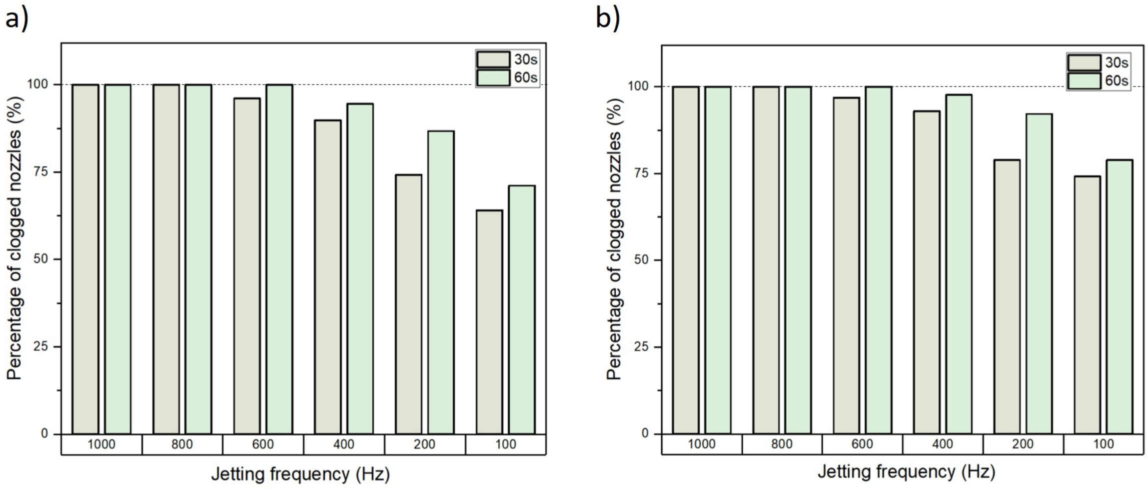

Figure 4.13: The percentage of clogged nozzles after 30 and 60s of ejection as a function of jetting frequency for anode inks: a) INK_SiΩC_CMC; b) INK_SiΩC_PEDOT.

It is obvious that high jetting frequency promotes nozzle clogging. When applying more than 800 Hz, all 128 nozzles were blocked, after only 30 s of the ejection, for both inks, with CMC and PEDOT:PSS. With a decrease in the frequency, more nozzles were opened. Operating with 100 Hz, after 60 s of the ejection, around 25% of the orifices were active. Therefore, in our study, we choose 100 Hz as an optimal frequency, but even with such a low value, the nozzles might be clogged after some time of printing. Then, the printheads had to be cleaned to continue.

Applying low values of the jetting frequency allowed for the deposition, although the ejection time was limited. Additionally, this significantly impacts the processing time. To give an idea, considering the deposition of a single layer of 10x10 mm, a decrease in the frequency from 1000 to 100 Hz causes an increase in the printing time from 5 to 50 min. Therefore, IJP loses its advantage of being a fast deposition method.

To summarize this section, the ejection of anode inks formulated with SiΩC was possible, but the drop generation process was not stable. Several assumptions were made to explain the origins of the instabilities:

- Large agglomeration of powder particles, fully or partially clogging the nozzles. Agglomerates are a barrier to fluid flow, blocking it or deviating the drop trajectory.
- Progressive deposition of a thin multilayer of ink on the surface of the nozzles. Initially, ejection is possible, but with time, orifices get smaller, until they are fully clogged. When the deposited material is not homogeneously distributed on the nozzles plate, non-symmetric jetting may be observed. Moreover, a part of the layer can be detached and displaced during the process, blocking the nozzles. This explanation has been proposed by Li *et al.* [231]. It is likely that high jetting frequency promoted the detachment of the deposited materials, leading to subsequent blockage of the orifices.
- Air bubbles entrapment. The deposited material can alter the shape of the meniscus formed by the ink and air. This can lead to the entrapment of air and encourage air bubbles to stick to the inside surfaces of the printhead. As a result, the ejection can be disrupted or blocked, which is also promoted by high jetting frequency [232].
- Viscoelasticity may be another reason for the drop trajectory's unpredictable deviation. All tested inks contain a polymeric binder. Therefore, the behavior of polymers during jetting should be considered. Figure 4.14 schematically represents the behavior of a binder at the molecular level. Before printing, when no stress is applied, polymeric chains are in a coiled state. As ink leaves the nozzle, they transform into a stretched state, and subsequently, after drop detachment, they come back to a coiled state. Therefore, inside a droplet, polymeric chains reorganize their structure, possibly disrupting the trajectory.

4.2.2 Inks with Si

Although the inks prepared with pure Si exhibited satisfactory stability, their ejection was impossible, even when applying the jetting frequency of 1 Hz. All the nozzles became clogged immediately after starting the printing. As the only difference between these inks and those prepared with SiΩC was the type of active material, it was assumed that Si

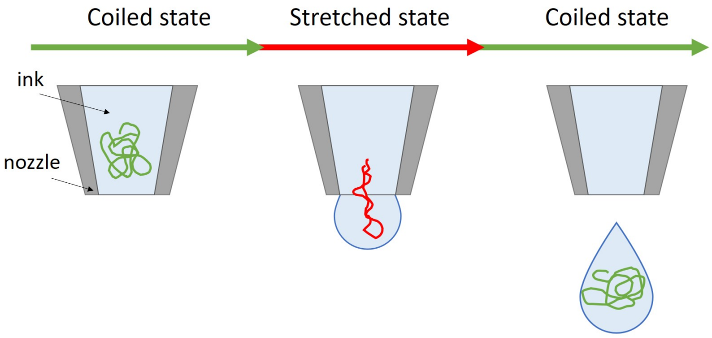

Figure 4.14: Schematic representation of polymer behavior at the molecular level during jetting.

nanoparticles were the main responsible for this issue. To confirm that, another ink with 50% less silicon powder than the initial ink was tested, and its behavior was registered as a function of time, which is presented in Figure 4.15.

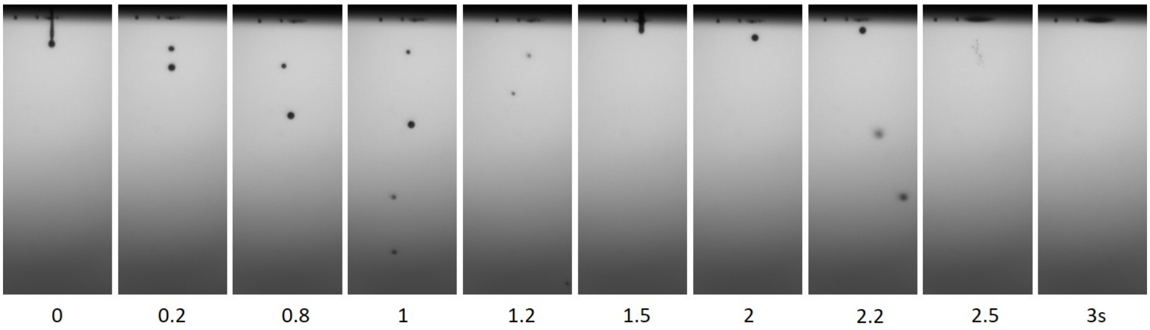

Figure 4.15: The ejection process of anode ink formulated with CMC and decreased amount of Si particles, as a function of time.

Initially, ejection was possible, but the drop generation process was unstable. After only 3 s, all the nozzles were clogged. Therefore, a lower amount of the active material in ink reduced the clogging problem, but printing was still impossible. These outcomes confirmed that the issues were attributed to the presence of pure silicon nanoparticles.

One hypothesis that could explain the clogging problem was the formation of air bubbles directly inside the printheads, preventing fluid flow. Si nanoparticles react with water to produce silicon dioxide, and hydrogen gas [233]. Generated gas entrapped inside the printheads could hinder the ejection. To verify it, printability tests were performed with the same ink that had been stored for a period of 2 months. Although after this time, the reaction kinetic should be much lower, the same behavior was observed. All the nozzles were immediately clogged, and the ejection was impossible.

To further investigate the origin of the problem, the surface chemistry of both Si and SiΩC powders was compared by FTIR analysis. FTIR spectra are presented in Figure 4.16.

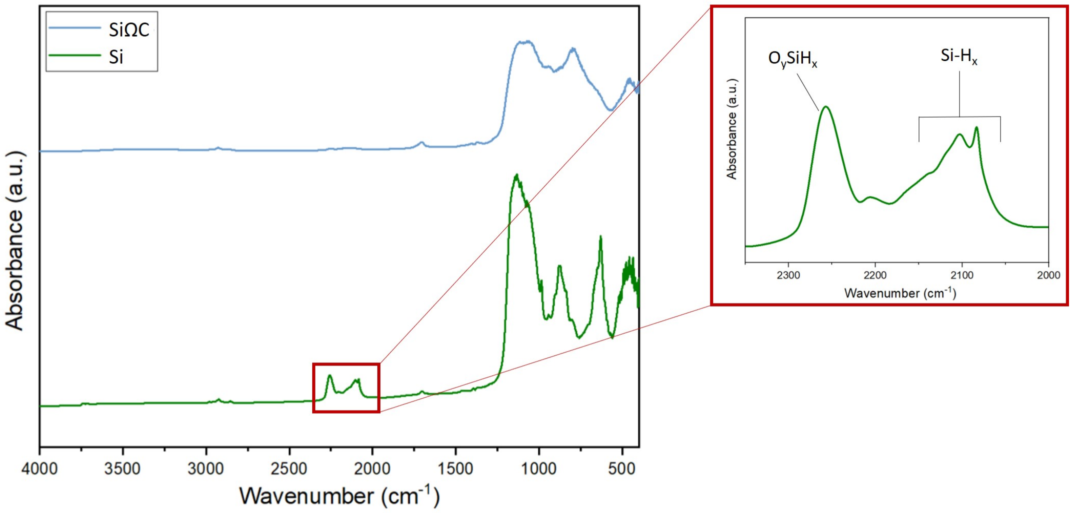

Figure 4.16: FTIR spectra of Si and SiΩC powders.

The absorbance bands between 2000 and 2200 $\mathrm{cm^{-1}}$ correspond to SiH_x stretching modes, and the peak at 2256 $\mathrm{cm^{-1}}$ is attributed to O_ySiH_x species [234]. These groups were observed only for pure Si and are the evidence of partial surface oxidation, the formation of the native SiO_2 layer. Carbon on the Si surface, a well-known reducing media, most likely converts the SiO_2 layer into Si or SiO_x layer (with $x < 2$) [230]. It is possible that these functional groups could create chemical bonds with the material comprising the nozzle. Nevertheless, due to the limited information available about the nozzle's design, only a rough assumption can be made. All that was specified is that it is made of a metallic material. Therefore, the likely cause of the ejection issue is the formation of hydrogen bonds between the O_ySiH_x species and hydroxyl groups present on the metal surface. A schematic representation of the bonding is shown in Figure 4.17.

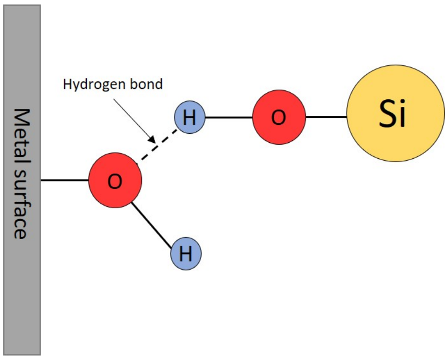

Figure 4.17: Schematic representation of hydrogen bond between Si particle and metal surface possibly causing the ejection issue.

4.3 Microstructural characterization of printed patterns

Despite the unstable ejection process, which posed a challenge to printing efficiency, the deposition of anode inks was demonstrated. Because of unstable jetting conditions and not reproducible results, as shown in the previous section, inkjet printing was performed using only one nozzle. Although both INK_SiΩC_CMC and INK_SiΩC_PEDOT inks were tested, only the structures created with the former are presented since the results were analogous. Depositions of anode inks were performed on the copper foil.

4.3.1 Printing of thin layers

To successfully print thin layers, the spacing between deposited droplets and the temperature of the substrate holder had to be optimized. The diameter of a single splat deposited on the foil was around 50 µm. Squares of 1x1cm were printed as trials.
Initially, a pattern without any space between adjacent drops was analyzed (see Figure 4.18a), and no heating was applied to the substrate. The resulting layer was not homogeneous, as depicted in Figure 4.19a. The ink distribution was uneven due to insufficient drying time for the drops to create a well-defined structure. Instead, the droplets spread on the copper foil and fused with one another. Some regions exhibited an accumulation of material, whereas other areas were empty.

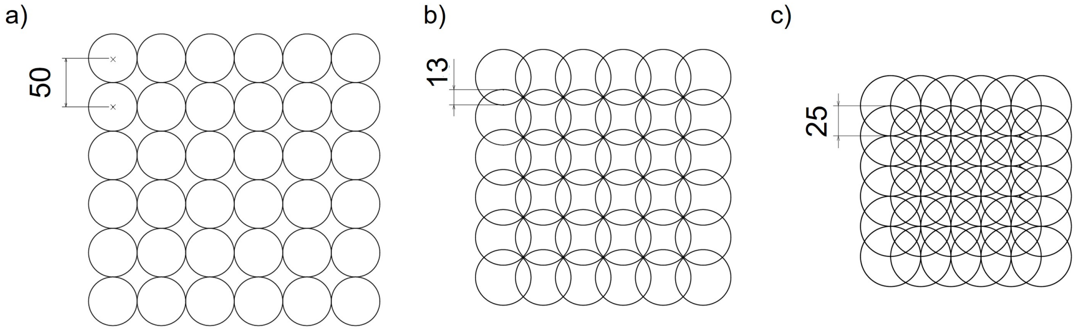

Figure 4.18: Printing pattern configurations used for the deposition of electrode layers: a) no overlapping of adjacent droplets, b) droplets overlap by 13 µm, c) droplets overlap by 25 µm.

In order to prevent this phenomenon, additional tests were conducted involving the heating of the substrate. Figure 4.19b shows the same pattern (no spacing between droplets) printed with the heating of the substrate holder (50°C). With the increased temperature, the deposited droplets could be dried before the following ones were ejected. The ink was homogeneously distributed on the foil, but low loading of powders was observed.

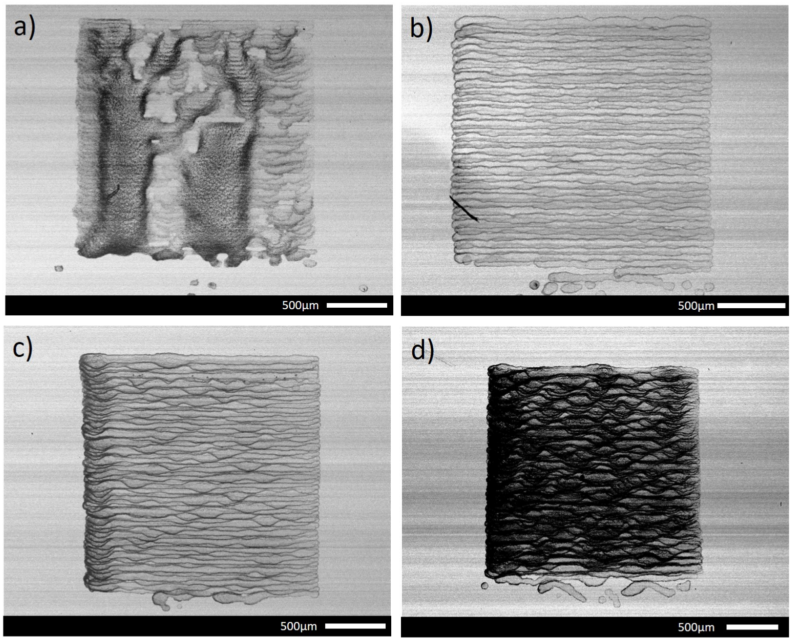

Figure 4.19: SEM images of anode layers printed using INK_SiΩC_CMC with different configurations: a) no overlapping of adjacent droplets, no heating of the substrate, b) no overlapping of adjacent droplets, substrate temperature 50°C, c) overlapping of droplets by 13 µm, substrate temperature 50°C, d) overlapping of droplets by 25 µm, substrate temperature 50°C.

To increase that, the spacing between drops was decreased so that they overlapped by 13 or 25 µm (see Figures 4.18b,c). Figures 4.19c and d show the resulting layers, where denser films were achieved with larger overlapping as more material was ejected. By repeating the pattern multiple times, more homogeneous structures could be obtained. However, the nozzles became clogged during the printing process, which limited the printing time.
Although the printing of thin layers was possible, it was challenging to fabricate samples, which could be electrochemically characterized. The process was not reproducible, with the issue of nozzle clogging repeatedly appearing.
It is noteworthy that the deposition of anode layers containing CMC using IJP was accomplished without experiencing cracking issues. The incorporation of latex, which was suspected to have a detrimental impact on electrochemical performance, proved unnecessary for ink formulation designed for IJP.

4.3.2 Printing of 3D structures

For printing anode pillars, the pattern, where the spacing between adjacent droplets was set to 50 µm (see Figure 4.20) was used. A single drop was ejected for one layer of a pillar. By repeating this sequence, 3D structure consisting of anode columns could be built.

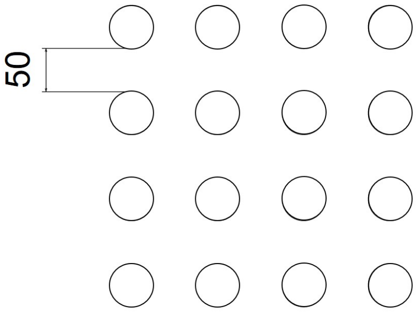

Figure 4.20: Printing pattern configuration used for the fabrication of anode pillars.

Figure 4.21a presents single splats of INK_SiΩC_CMC ink deposited without heating of the substrate, while Figure 4.21b shows the same pattern printed with the substrate temperature of 50°C. The elevated temperature decreased drying time, resulting in a more homogeneous structure with powders uniformly distributed within splats. When no heating was applied, more material was loaded on the edges. This phenomenon is called the coffee-ring effect, and it is an issue that frequently arises during the drying of particle-laden droplets. The non-uniform evaporation flux at the air-liquid interface of the sessile droplet, which is observed to be larger along the three-phase contact line, is what drives this ubiquitous process. The larger liquid loss at the edges is replenished by the fluid from the drop center. The particles are then driven to the contact line by an evaporation-induced flow, and as the solvent completely evaporates, a pattern in the shape of a ring emerges [235]. Additionally, some of the splats fused with each other, leading to a disordered arrangement. Therefore, heating the substrate is beneficial for printing well-defined structures.

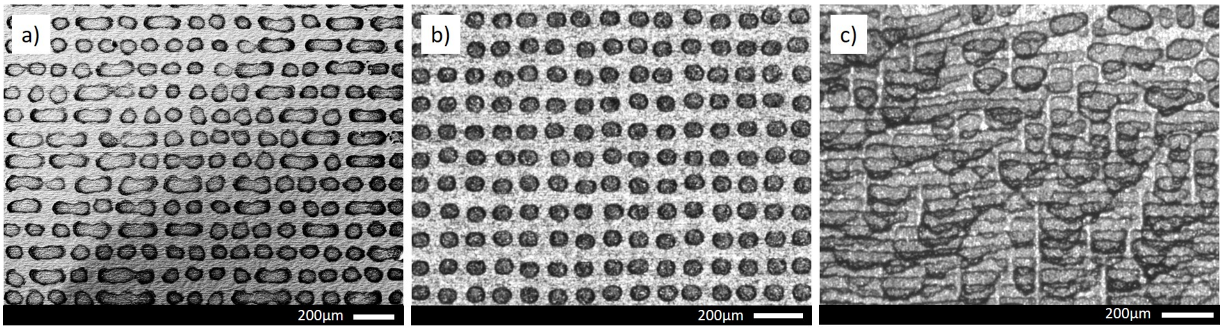

Figure 4.21: Single splats of INK_SiΩC_CMC: a) without heating of the substrate, b) with the substrate temperature of 50°C, c) after 3 passes of printing with the substrate temperature of 50°C.

Figure 4.21c shows the same pattern repeated 3 times with the heating of the substrate. The accuracy of the drop positioning was insufficient to build the intended 3D shape. The possible explanations of the deviation of droplet trajectory were discussed in Section 4.2.1.

4.4 Emission measurements

To evaluate the potential risks to human health associated with ink formulation and inkjet printing of anode inks, the emission of particles was examined using the Optical Particle Sizer 3330 and the NanoScan SMPS Nanoparticle Sizer 3910, which are represented in Section 2.1.2.

The analyses were performed on ink samples that included CMC as a binder, *i.e.* INK_Si_CMC, and INK_SiΩC_CMC. The inks were prepared under a fume hood, according to the procedure presented in Section 5.1.3. This process took place under a fume hood. Throughout the entire procedure, the emission measurement equipment was situated in close proximity to the operator. During the inkjet printing process, emission measurements were performed in three distinct zones: the Worker Area (WA), the Emission Source (ES), and the Exhaust Tube (ET) (see Section 2.1.2).

Prior to ink formulation and inkjet printing, the particle number concentration was evaluated in order to establish the background for analyzing the results.

The particle number concentrations during ink formulation for nanoparticles and microparticles are presented in Figure 4.22a, and Figure 4.22b, respectively.

For both nanoparticles and microparticles, the background particle number concentration was found to be higher than during the ink formulation process, although this discrepancy lacks physical or practical significance. This difference could be attributed to measurement accuracy.

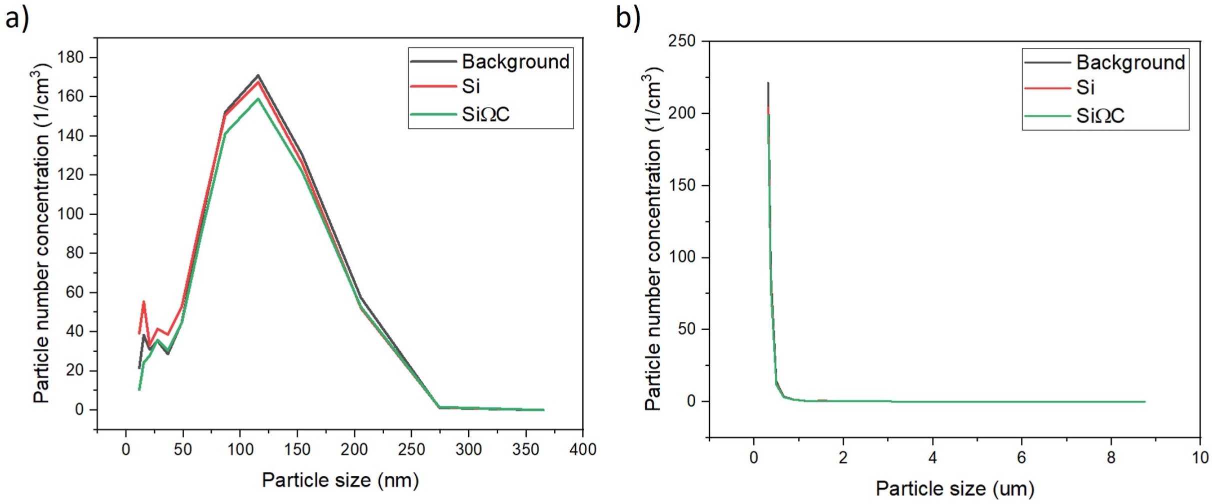

Figure 4.22: The particle number concentrations per cm^3 during anode ink formulation for: a) nanoparticles, b) microparticles.

The particle number concentrations during inkjet printing of anode inks for nanoparticles and microparticles are presented in Figure 4.23.

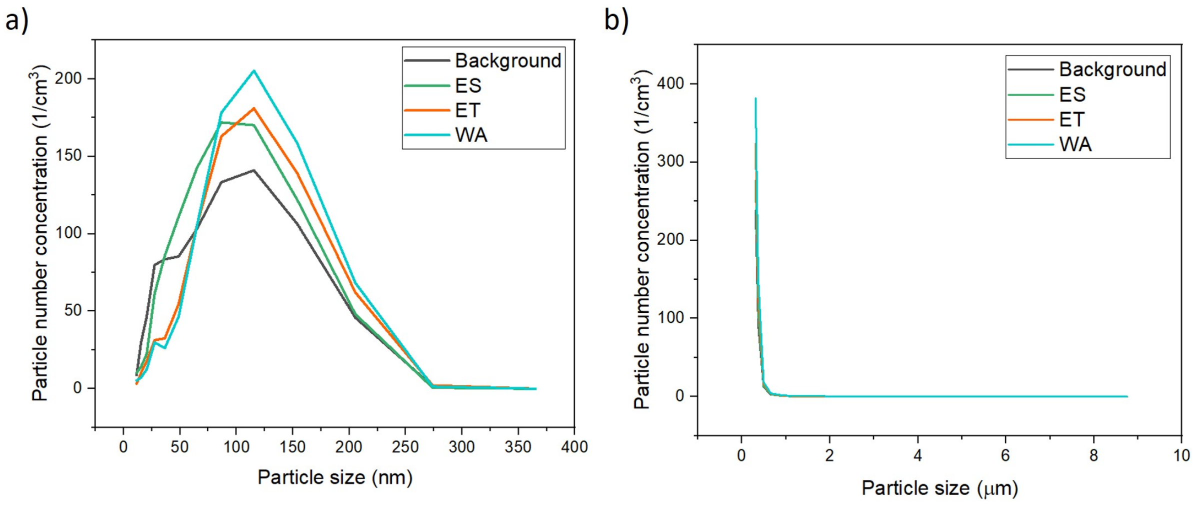

Figure 4.23: The particle number concentrations per cm^3 during inkjet printing of anode inks for: a) nanoparticles, b) microparticles. ES - Emission Source, ET - Exhaust Tube, WA - Worker Area.

Upon analyzing the release of nanoparticles throughout the procedure, it was determined that the particle number concentration, when considering the background, is insignificant. The greatest recorded value was observed within the vicinity of the worker, where approximately 60 particles measuring 115nm were found per cubic centimeter. However, it is important to note that this value could potentially be attributed to measurement error. Regarding the emission of microparticles, there was no observed release.

Based on the results, it can be concluded that both ink formulation and inkjet printing processes exhibit minimal particle release, thus resulting in negligible effects on potential inhalation exposure.

4.5 Conclusions

In conclusion, we presented the formulation of stable water-based anode inks, specifically designed for IJP, but also adaptable for other wet-processing techniques. The measurements of the particle emission during anode ink formulation and inkjet printing process showed that the procedures do not pose any risks to human health.

Anodes fabricated with PEDOT:PSS binder exhibited excellent performance. The electrodes containing carbon-coated silicon nanoparticles and PEDOT:PSS achieved a cutoff lithiation capacity of 2000 mAh g^{-1} with no observed capacity degradation over time. In contrast, anodes composed of pure silicon demonstrate a capacity decay after 75 cycles, proving the advantages of utilizing silicon/carbon core-shell structure.

Printability tests revealed the instabilities of the drop generation process and the importance of particle surface chemistry. While inks formulated with SiΩC were capable of being ejected, the printing process itself proved to be unstable. This instability could be attributed to various factors such as the accumulation of large agglomerations of powder particles leading to nozzle clogging, the gradual buildup of a thin multilayer of ink on the nozzle's surface, entrapment of air bubbles, or the viscoelastic nature of the inks. Furthermore, our findings demonstrated a direct correlation between the jetting frequency value and the occurrence of nozzle clogging. Higher jetting frequencies were found to promote nozzle clogging. Consequently, the deposition of anode inks became feasible by utilizing lower jetting frequencies, but this came at the expense of losing the advantage of fast deposition associated with IJP.

While exhibiting satisfactory stability, inks formulated with pure silicon were unable to be ejected, even at extremely low jetting frequencies. Two possible explanations for this issue were the generation of air bubbles within the printheads, or the chemical bonding between the surface of silicon nanoparticles and the hydroxyl groups on the metallic surface of the nozzle.

Despite facing challenges with the ejection process, we successfully achieved the deposition of anode inks formulated with SiΩC. By optimizing the printing parameters, we were able to obtain uniform thin layers.

It is noteworthy that the deposition of anode layers containing CMC using IJP was accomplished without experiencing cracking issues, contrary to the tape-casted electrodes. Therefore, the addition of latex, which was suspected to have a detrimental impact on electrochemical performance, proved unnecessary for ink formulation designed for IJP.

However, when attempting to build 3D structures, we encountered limitations in the accuracy of drop positioning, which hindered the desired outcome. To address these issues, further refinement and optimization of the technology are necessary, particularly in mitigating nozzle clogging.

One potential solution is the application of non-adsorbing coatings on the surface of the nozzles. This could help minimize the formation of hydrogen bonds between the ink particles and the nozzle surface, thereby reducing clogging. Additionally, the implementation of a cleaning unit designed to unblock the nozzles during the printing process could contribute to a more stable and reliable process. Furthermore, the issue of nozzle clogging can be addressed by exploring alternative DOD technologies, such as the acoustic inkjet printer. Overall, further optimization efforts are essential to enhance printing accuracy and stability, allowing for the successful fabrication of 3D structures using silicon anode inks.

Summary:

- Stable water-based silicon anode inks, specifically designed for IJP, but also adaptable for other wet-processing techniques, were successfully formulated, and the particle emission measurements confirmed that the preparation procedure and inkjet printing pose no risks to human health.
- Electrochemical analyses revealed that PEDOT:PSS-based samples performed best, attaining the cutoff lithiation capacity of 2000 mAh/g right after the formation. CMC/Latex-based samples exhibited much lower lithiation capacities, whereas the low molecular weight CMC reached higher values.
- Inks containing SiΩC were successfully ejected, but the printing process exhibited instability. Nevertheless, it was possible to deposit thin layers successfully. However, when attempting to create 3D structures, the accuracy of drop positioning posed limitations and hindered the desired results.
- The ejection of inks formulated with pure silicon proved to be unsuccessful, highlighting the significance of surface chemistry in the process. The formation of hydrogen bonds between the silicon particles' surface and the hydroxyl groups on the metal surface of the printing nozzles likely caused this ejection issue.
- Optimization of the technology is necessary to enhance printing accuracy and stability of the process, allowing for the successful fabrication of 3D structures using silicon anode inks.

5

Inkjet printing of cathode for LIBs

Summary

THIS chapter presents the development of stable ink formulations for the production of cathodes in modern lithium-ion batteries (LIBs). NMC, one of the most common cathode materials for electric vehicles' batteries is used as active material. The preparation process is detailed for both water-based and organic solvent-based inks, with step-by-step demonstrations. The effects of water exposure on the properties of NMC cathode material are assessed, indicating that aqueous processing could be a viable option for electrode fabrication. The electrochemical properties of inkjet printable inks are analyzed to assess the effect of ink compositions. The printability tests are presented, revealing the strain hardening phenomenon, which may hinder the ejection. The structural characterizations of printed patterns are presented. Finally, we address the issue of particle emissions during ink preparation and inkjet printing, and present measurements showing that the processes are safe for human health.

5.1 Ink formulation and characteristics

5.1.1 Cathodes composition

Inks were formulated by mixing $LiNi_{0.333}Mn_{0.333}Co_{0.333}O_2$ (NMC333) (Sigma Aldrich), polymeric binder and Super P Carbon Black (CB) (Alfa Aesar) in the ratio of 70:26:4 by weight, which was recommended by one of the project's partner. Four kinds of binders were tested: high M_w binder (HB) (DAIKIN), low M_w binder (LB) (DAIKIN), carboxymethyl cellulose (CMC) of $M_w \sim 90000\,\mathrm{g/mol}$ (Sigma Aldrich), poly(3,4-ethylenedioxythiophene)-poly(styrenesulfonate) (PEDOT:PSS) (Sigma Aldrich). Depending on the used binder, deionized water (DI-water) or acetone + propylene carbonate were used as solvents. The dispersing agent BYK-22144 was added to the formulation.

To achieve a suitable viscosity for shaping, the slurries used for tape-casting were modified by decreasing the amount of solvent. The ratio of active material to conductive agent to binder remained constant. 8wt% of Duramax B-1000 acrylic latex (Rohm and Haas) was incorporated into the formulations of CMC-based anodes in order to prevent cracking.

5.1.2 Effect of water exposure on NMC properties

Upon adding NMC333 to water, the pH of the suspensions rapidly increased as illustrated in Figure 5.1. The measurements were performed with a sample representing actual ink concentrations, i.e. around 1wt% of NMC in water.

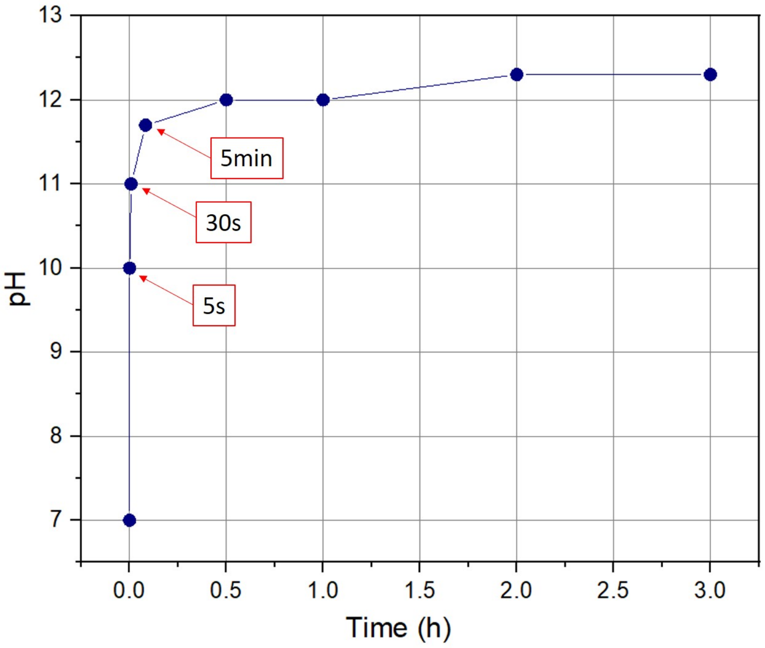

Figure 5.1: pH as a function of time after introducing NMC333 in water.

The solution became basic very quickly, indicating a strong driving force behind the reaction between NMC and water. Moreover, it was observed that longer exposure times did not lead to significant changes. Beyond 2 hours, no further increase in pH was detected. The exchange of Li^+/H^+ ions between NMC and water is the most likely cause of the observed pH changes. Water acts as a source of H^+ ions, which react with NMC to form OH^- ions, increasing the pH of the solution. The exchanged Li^+ ions then combine with the OH^- ions to form LiOH. Subsequently, the LiOH reacts with CO_2 in the atmosphere, giving rise to the formation of Li_2CO_3, as indicated in the following reactions [236]:

$$Li^+ + H_2O \rightarrow H^+ + LiOH$$

$$LiOH + CO_2 \rightarrow LiHCO_3$$

$$LiOH + LiHCO_3 \rightarrow H_2O + Li_2CO_3$$

To observe the changes within NMC333 crystal structure after water exposure, XRD analysis was performed. 1wt% of NMC333 was stirred in water for 24h. Afterward, the powder was dried and examined. Figure 5.2 displays the XRD patterns of raw NMC333 and NMC333 after water exposure. No significant difference was observed between the spectra. As mentioned in Chapter 3 the I(003)/I(104) ratio serves as an indirect measure of the degree of cation mixing between Li^+ and Ni^{2+} ions in the lithium layer. The I(003)/I(104) ratio for raw powder was 0.55, while after water exposure 0.51. The observed change was minimal and suggested that the material's overall structure remained intact. Additionally, the distinct separation between the (108) and (110) peaks in the spectrum indicated that the layered structure was not impacted by exposure to water [237].

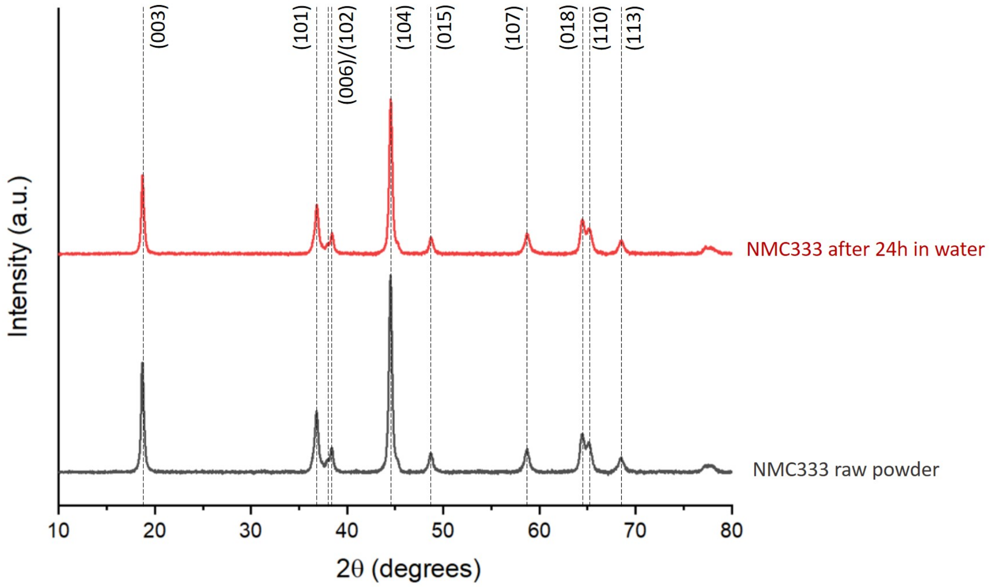

Figure 5.2: XRD patterns of raw NMC333 and NMC333 after 24h of water exposure.

In order to gain a deeper understanding of the impact of water exposure on the NMC material, the ICP technique was employed to quantify the extent of leaching of Li, Ni, Mn, and Co ions into the solution during the mixing process. 1wt% of NMC333 was stirred in water for 24h. Afterward, the suspension was centrifuged and filtered using a 0.1 µm PTFE syringe filter (Whatman). The resulting solution was then analyzed. No measurable quantities of Ni, Mn, and Co ions were detected, whereas an approximate amount of

0.4wt% of Li was found to have leached into the water. The extent of dissolution observed was minimal and could potentially come from a combination of LiOH and Li_2CO_3, as suggested in the article of Wood et al [238]. Therefore, water exposure did not cause any structural changes and led to only minimal Li leaching, which suggested that aqueous processing may be feasible for NMC333 powder.

5.1.3 Ink preparation

The compositions of the different inks formulated here are given in Table 5.1. For simplicity, in this Chapter, we denote the tested inks as follows: INK_HB - ink prepared with high M_w binder from DAIKIN, INK_LB - ink prepared with low M_w binder from DAIKIN, INK_CMC - ink prepared with CMC, INK_PEDOT - ink prepared with PEDOT:PSS. Because HB and LB binders could be dispersed only in aprotic solvents, acetone was used for the formulation of INK_HB and INK_LB. DI-water was used to prepare INK_CMC and INK_PEDOT, and zeta potential as a function of pH measurements were carried out to evaluate the stability of CB and NMC333 when mixed with water.

In the study, numerous inks were prepared with various solvent-to-powders ratios, and they were optimized using a trial-and-error method. Here, we present only examples of formulations, which were optimal in terms of stability and printability.

Water-based inks - stability

Figure 5.3 shows zeta potential as a function of pH for NMC333 and CB powders.

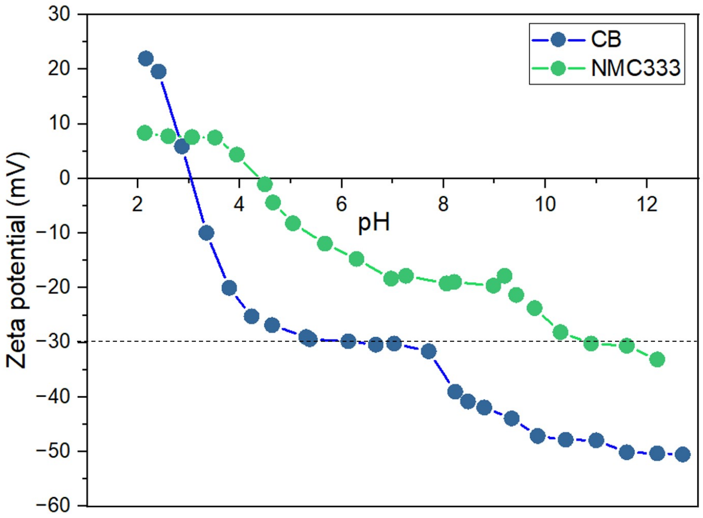

Figure 5.3: Zeta potential as a function of pH for NMC333 and CB powders measured by Zetasizer Nano ZS.

The values were highly negative at pH values above 6 for CB, and above 10 for NMC333. It suggested that electrostatic charges present on the particle surface at high pH levels could separate them from each other, creating a stable suspension. Consequently, it was recommended to prepare aqueous inks with a high pH level, preferably above pH 10, to promote particle separation and achieve a stable suspension.

It is noteworthy that the addition of a base to the inks was unnecessary, as the pH of the suspensions rapidly increased upon the introduction of NMC333.

Considering the zeta potential measurements, it could be inferred that NMC333 exhibits stability at a pH of approximately 12, corresponding to the basicity of water after the introduction of the powder (refer to Figure 5.1). However, it is important to note that the negative charge on the particle surface alone may not always guarantee stability. Therefore, the influence of a dispersing agent on the stability of NMC333 in water was investigated. A dispersing agent was also necessary to mitigate the hydrophobic nature of CB.

The selection of the surfactant was based on straightforward sedimentation experiments, with BYK-22144 yielding desirable outcomes for both powders, CB and NMC. The use of a single type of dispersant helps prevent the possibility of undesirable interactions between the various components of the ink. The optimal amount of the dispersing agent was evaluated by viscosity measurements. The results are presented in Figure 5.4 and 5.5 for NMC333 and CB, respectively.

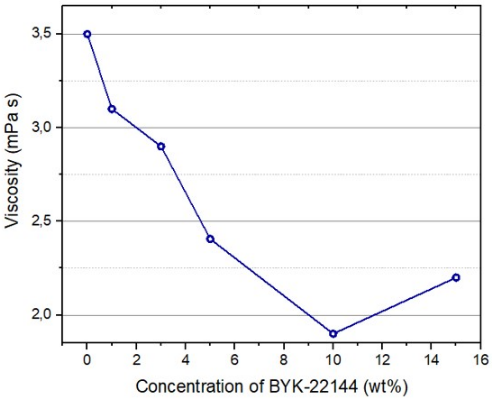

Figure 5.4: Viscosity as a function of BYK-22144 concentration for NMC333 powder.

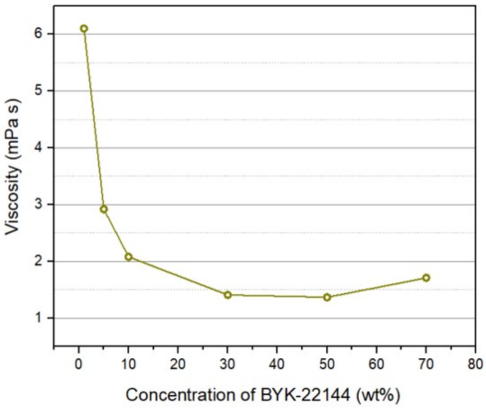

Figure 5.5: Viscosity as a function of BYK-22144 concentration for CB powder.

The concentration at which the viscosity reaches a minimum represents the optimal amount of dispersing agent required to achieve stable dispersion.

Without the dispersing agent, the suspension exhibited relatively high viscosity, indicating the beneficial effect of adding BYK-22144. The optimal amount of BYK-22144 for NMC333 was determined to be 10wt%. It was found that electrostatic interactions alone were insufficient to achieve high stability.

As for CB powder, the optimal quantity of the dispersing agent totaled to 50wt%. The high amount can be rationalized by the need to evenly coat the very high surface area of the nanoparticles in order to prevent clumping, as already discussed in Chapter 4 (Section 4.1.2).

Organic solvent-based inks - stability

The selection of a suitable dispersing agent for organic solvent-based inks was based on sedimentation tests. BYK-22144 exhibited favorable results when used with NMC333 powder. However, when dispersing CB in acetone, the addition of a dispersant had a negative impact on stability, and the best outcomes were achieved without its inclusion. As the viscosity of acetone is relatively low, the results obtained using rheometers were not accurate enough to estimate the optimal concentration of BYK-22144 for NMC333 dispersed in the solvent. Therefore, sets of suspensions with different amounts of the dispersant were prepared, and their behavior was evaluated by sedimentation tests. The sample with the longest settling time was chosen as the optimal.

The sedimentation experiments conducted on NMC333 with varying quantities of BYK-22144 are illustrated in Figure 5.6.

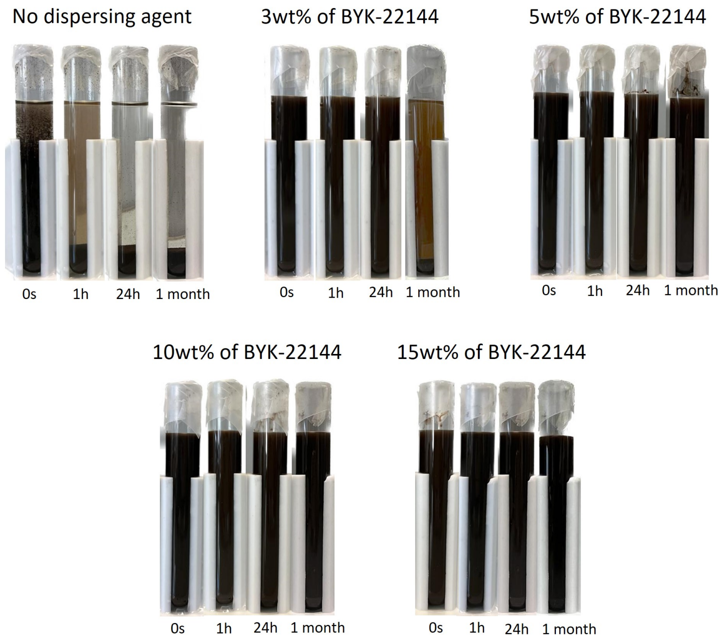

Figure 5.6: The sedimentation experiments conducted on NMC333 powder with varying concentrations of BYK-22144.

When no dispersant was added, the powder exhibited immediate settling. With the inclusion of 3wt% of BYK-22144, the stability improved, although sedimentation still occurred after one month. However, using higher amounts of the dispersant, specifically 5, 10, and 15wt%, resulted in exceptional stability, with no settling observed even after one month. To prevent the degradation of electrode electrochemical properties caused by excessive amounts of organic materials, the optimal concentration of BYK-22144 was identified as 5wt%, representing the minimum required amount.

To demonstrate that the inclusion of a dispersant does not contribute to the stability of CB in acetone, sedimentation tests were performed with varying concentrations of BYK-22144 (see Figure 5.7). As the amount of dispersant increased, the settling time decreased. Consequently, it was concluded that CB should be dispersed in acetone without the use of the dispersing agent.

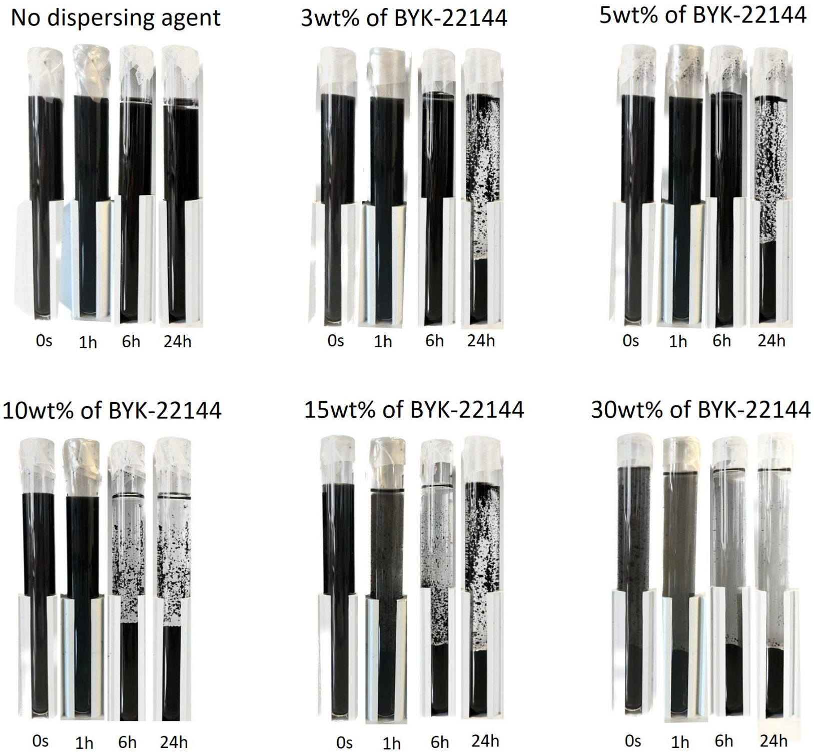

Figure 5.7: The sedimentation experiments conducted on CB powder with varying quantities of BYK-22144.

Mixing procedure

The schematic representation of the ink preparation procedure for all inks is illustrated in Figure 5.8.

For acetone-based inks (INK_HB and INK_LB) (Figure 5.8a), the binders were dissolved in acetone through magnetic stirring, and NMC333 and CB powders were mixed in acetone using a high-speed disperser at 1000 rpm for 10 minutes, with and without the addition of a dispersing agent, respectively. Subsequently, both suspensions were combined and stirred together using the high-speed disperser for another 10 minutes at 1000 rpm. The final step involved the inclusion of propylene carbonate (10 wt%) as a co-solvent, and all the components were mixed using magnetic stirring. The purpose of the co-solvent was to reduce the evaporation rate of the formulated slurries, preventing the inks from drying in the nozzle before printing.

The preparation process for water-based inks (INK_CMC and INK_PEDOT) (Figure 5.8b) involved the dissolution of binder in water through magnetic stirring, separately dispersing NMC333 and CB powders in water with the addition of dispersing agent (using a high-speed disperser at 1000 rpm for 10 minutes), and finally mixing all the components together (using a high-speed disperser at 1000 rpm for 10 minutes).

Additionally, to prevent excessively large agglomerates, all the inks were filtered through 2 µm filters before printing.

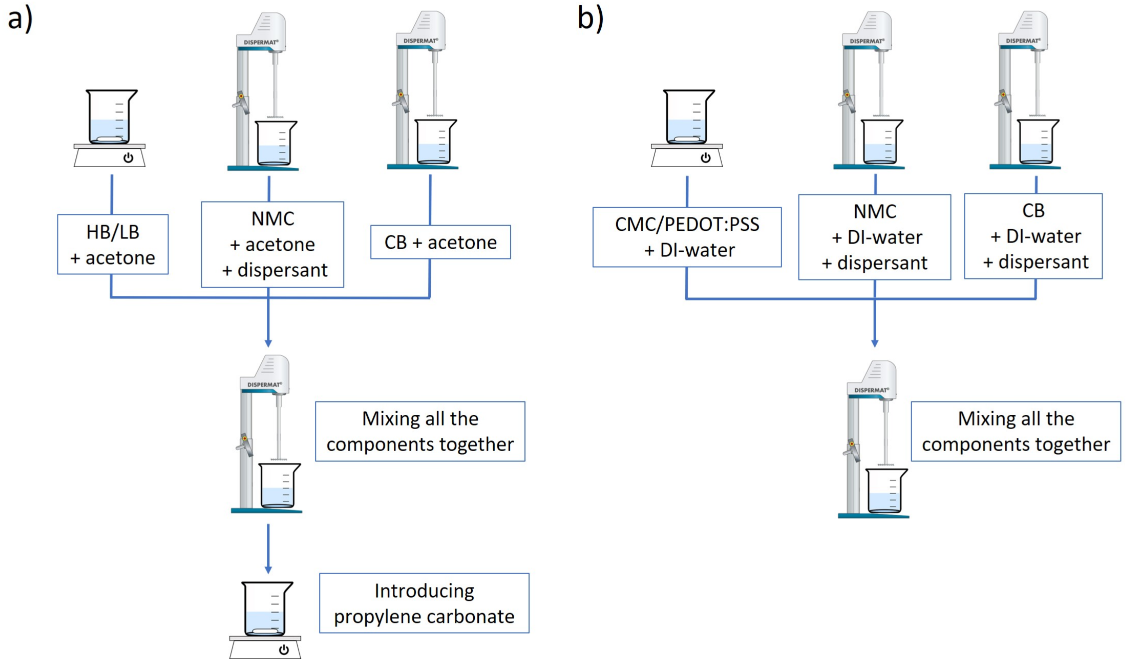

Figure 5.8: Schematic representation of preparation procedure for: a) INK_HB and INK_LB (acetone-based cathode inks), b) INK_CMC and INK_PEDOT (water-based cathode inks).

5.1.4 Ink characteristics

The viscosity, surface tension, and density were measured for each formulation, and the resulting values, together with the Z number, are presented in Table 5.1.

Table 5.1: Composition and characteristics of cathode inks designed for IJP.

Ink	Composition	Solvent	Surface tension (mN/m)	Viscosity (mPa.s)	Density (g/ml)	Z
INK_HB	NMC333+CB+HB	90wt% acetone + 10wt% propylene carbonate	23.6	7.6	0.67	~4
INK_LB	NMC333+CB+LB	90wt% acetone + 10wt% propylene carbonate	23.4	5.1	0.65	~5
INK_CMC	NMC333+CB+CMC	DI-water	41.3	4.4	0.87	~10
INK_PEDOT	NMC622+CB+PEDOT:PSS	DI-water	43.7	4.5	0.74	~9

Viscosity values were determined at a shear rate of $100\,s^{-1}$, and were adjusted by altering the amount of solvent. According to the printer's manufacturer, these values fall within the recommended range for all inks. Figure 5.9 illustrates how the viscosity varies as a function of shear rate.

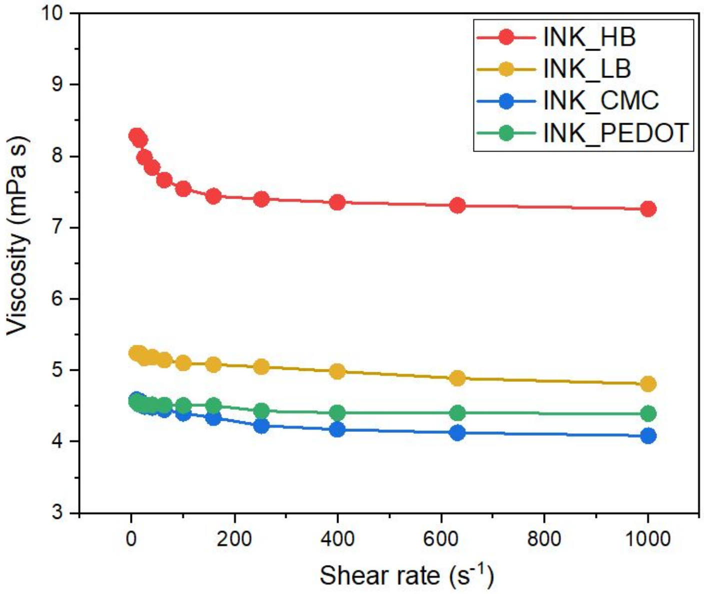

Figure 5.9: Viscosity as a function of shear rate for INK_HB, INK_LB, INK_CMC, and INK_PEDOT.

Although INK_HB and INK_LB showed remarkably low surface tensions, while INK_CMC and INK_PEDOT exhibited notably high surface tensions, the Z number for each ink was within the appropriate range for printing (1<Z<10).

The formulated inks exhibited remarkable stability, as evidenced by the sedimentation tests (see Figure 5.10). Even after a month, there was no indication of any settling. Further analysis using Turbiscan also showed that there were no mechanisms that could destabilize the inks (see Figure 5.11). The backscattered and transmitted light profiles of all the inks remained constant throughout the test period (1 h).

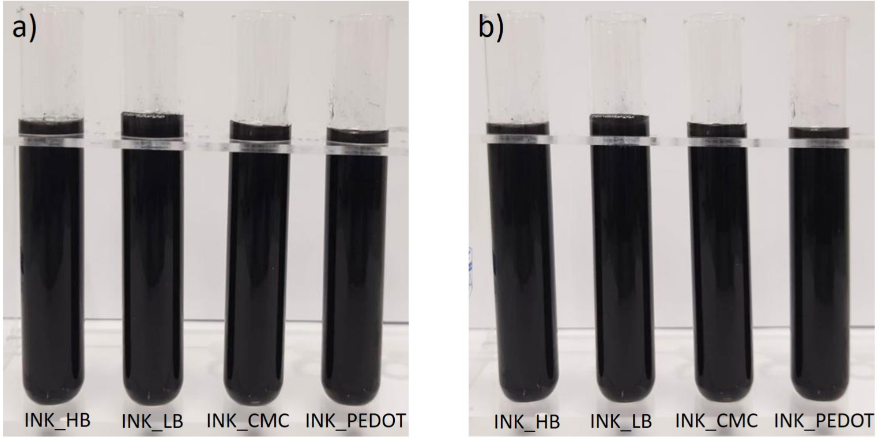

Figure 5.10: Photographs of sedimentation tests for cathode inks as a function of time: a) inks at the beginning of the test, b) inks after one month from the beginning of the settling test.

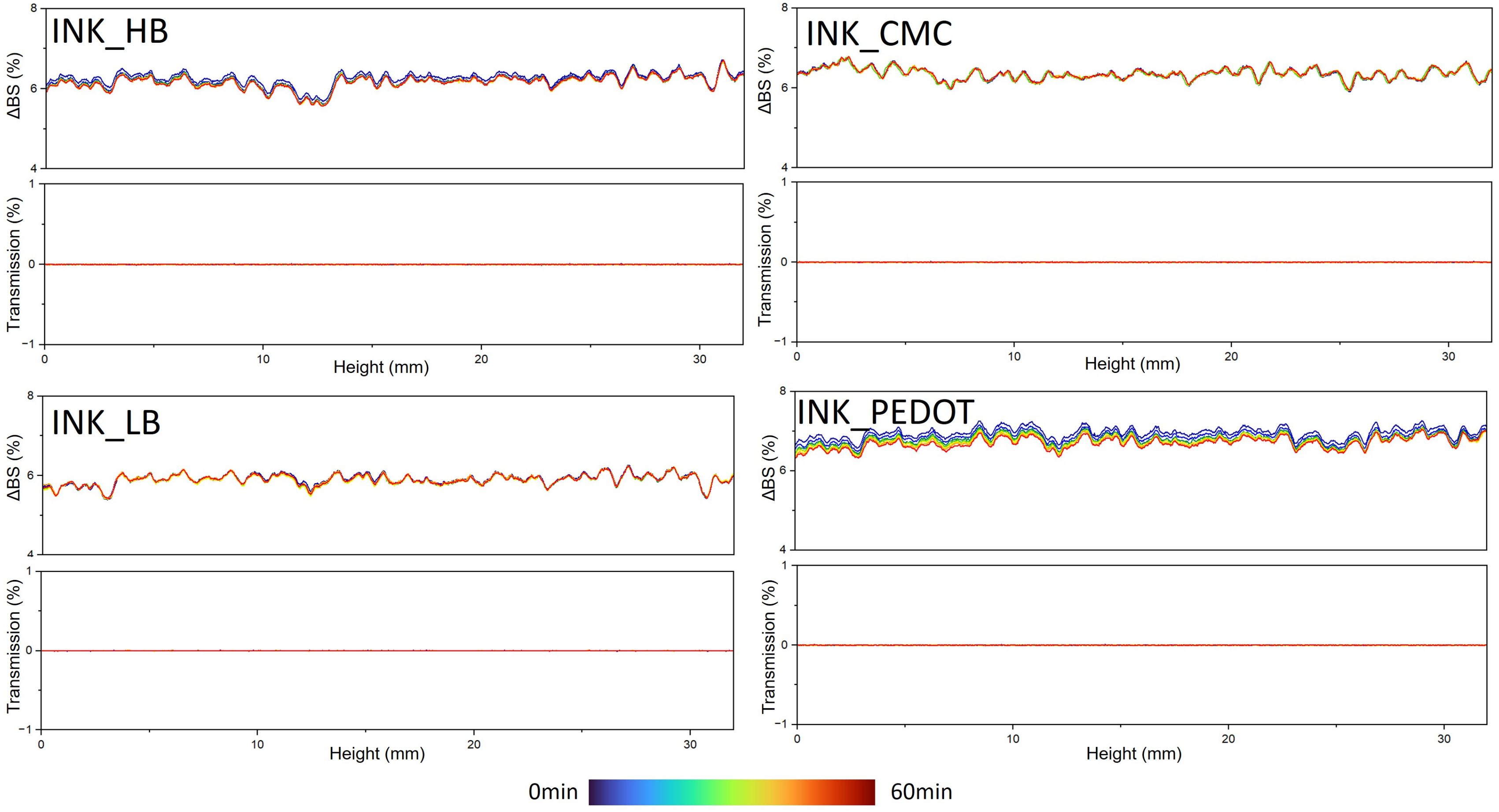

Figure 5.11: Backscattering and transmission profiles of formulated cathode inks by Turbiscan Lab stability analysis measured during 1 h with 10 min of intervals.

5.1.5 Electrochemical characteristics

To evaluate how the ink formulations affect the cathode's performance, electrochemical tests were conducted on tape-casted electrodes.
The compositions of tested cathode slurries are presented in Table 5.2.

Table 5.2: Compositions of cathode slurries used for fabrication of tape-casted electrodes.

Nomenclature	Active material	Binder	Conductive agent	Solvent	Additives
CATHODE_HB	70wt% NMC333	26wt% HB	4wt% CB	acetone + propylene carbonate	-
CATHODE_LB	70wt% NMC333	26wt% LB	4wt% CB	acetone + propylene carbonate	-
CATHODE_CMC	65wt% NMC333	24wt% CMC	3wt% CB	DI-water	8wt% Latex

HB - high M_w binder (DAIKIN), LB - low M_w binder (DAIKIN), CMC - carboxymethyl cellulose of $M_w \sim 90000$, CB - Super P Carbon Black, Latex - Duramax B-1000 acrylic latex.

Figure 5.12 shows SEM images of the top views of CATHODE_HB and CATHODE_LB deposited on the aluminum foil after drying. Due to its higher molecular weight, HB led to the formation of a consistent cathode layer (Figure 5.12a), whereas the utilization of LB led to the development of cracks within the electrode (Figure 5.12b), potentially leading to poor electrochemical performance. It was assumed that shorter polymeric chains of LB were not able to establish a cohesive network among the components of the slurry.

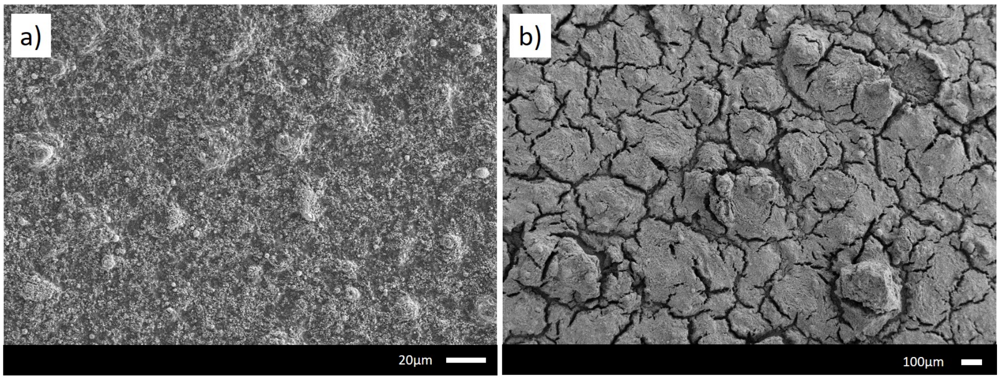

Figure 5.12: SEM images of cathode layers deposited by tape casting with: a) CATHODE_HB, b) CATHODE_LB.

For the preparation of electrodes with CMC, latex in the quantity of 8wt% had to be added to the formulations. Otherwise, the cathodes were cracked after drying.
Due to the poor wettability of the cathode slurry fabricated with PEDOT:PSS as a binder, this formulation was not electrochemically tested.

The tape-casted films were cut and assembled into CR-2030 coin cells, where lithium metal foil served as the counter electrode. This assembly process took place in an argon-filled glove box to maintain controlled conditions. LP40 ($LiPF_6$ at 1M in a mixture of EC:DEC [1:1]) was used as an electrolyte.

Cycling tests were conducted at a constant current ranging from 3.0 V to 4.3 V at a temperature of 25°C. The initial three cycles, known as the formation cycles, were performed at a current rate of 0.1C. Following the formation cycles, 100 additional cycles were carried out at a current rate of 1C.

Figure 5.13 shows the specific capacity vs cycle number of tape-casted cathodes. The electrodes fabricated with CMC as a binder were unable to store any electrical charge or deliver any energy. In the initial cycle, the specific capacity was measured at 0mAh/g. This could be attributed to either the influence of CMC itself or the presence of latex. Both CMC and latex act as insulating materials, potentially creating a barrier between the active material and the current collector, consequently diminishing the overall electrical conductivity.

Furthermore, due to its relatively high viscosity, CMC could lead to the formation of a thicker electrode layer with reduced porosity. This thicker layer hinders the diffusion of lithium ions within the cathode structure, resulting in slower ion transport kinetics.

Cathodes formulated with HB and LB displayed pronounced aging. The capacity of the electrodes consistently decreased as the number of cycles increased, with a noticeable decline occurring after three formation cycles. For CATHODE_HB, the electrodes initially displayed a capacity of roughly 98mAh/g during the first cycle. However, this capacity gradually declined to only 45 mAh/g after 50 cycles. After 100 cycles, an approximate capacity retention of 25% was observed. The electrochemical performance of CATHODE_LB was even worse, with the specific capacity reaching 27 mAh/g during the formation cycles and dropping to only 3 mAh/g after 50 cycles.

The difference in the cycling behavior of CATHODE_HB, and CATHODE_LB was most likely attributed to the utilization of different binder structures. As previously mentioned, CATHODE_LB, with its shorter polymeric chains, was unable to establish a continuous network within the cathode. This lack of continuity within the network may result in interruptions or discontinuities along the electron pathway, impeding the smooth flow of electrons and hindering efficient electron transport. Furthermore, this discontinuous network has the potential to introduce mechanical instability. Throughout the charge/discharge process, stress concentrations can arise at these disconnected regions, potentially leading to mechanical failures such as electrode cracking or delamination.

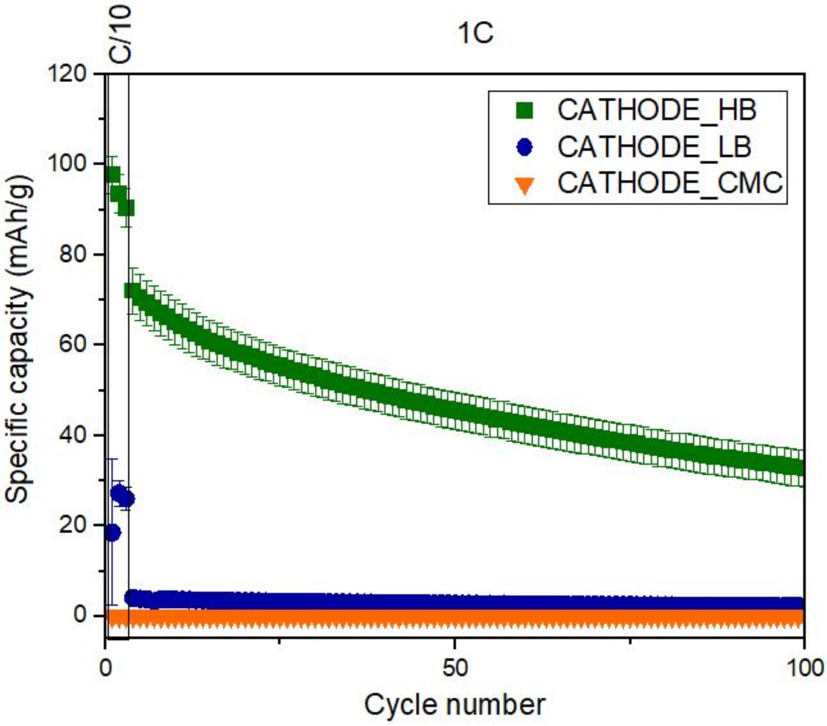

Figure 5.13: Specific capacity vs cycle number at C/10 (3 initial cycles) and 1C (100 cycles) for tape-casted cathodes. The measurements were performed at 25°C

In the study conducted by Noh *et al.* [74], it was reported that cathodes fabricated using NMC333 demonstrated a significantly higher specific capacity of 150 mAh/g compared to the results obtained in our research. However, the electrochemical tests conducted in our study were preliminary and aimed at establishing a baseline for further optimization. Our objective was to compare the effects of binders on cathode performance. However, it is important to note that due to time constraints and the fact that the analyses were carried out in a different laboratory, the preparation and shipping conditions were not thoroughly elaborated upon.

In order to further investigate the effect of CMC, it is necessary to substitute Duramax B-1000 with a product specifically designed for battery applications. Interpreting the results, it becomes challenging to determine whether the deterioration in cathode performance was specifically caused by CMC or water, as there are several other factors that could have contributed. These factors include preparation and storage conditions, the influence of additives, and the ratio between the different components.

5.2 Printability tests

Figure 5.14 presents the results of the printability tests for all studied cathode inks. These images display droplets ejected from the printer's nozzle at different stages of the drop generation process. High jetting frequency did not have a significant impact on the nozzle clogging, so 1000 Hz was used for the tests.

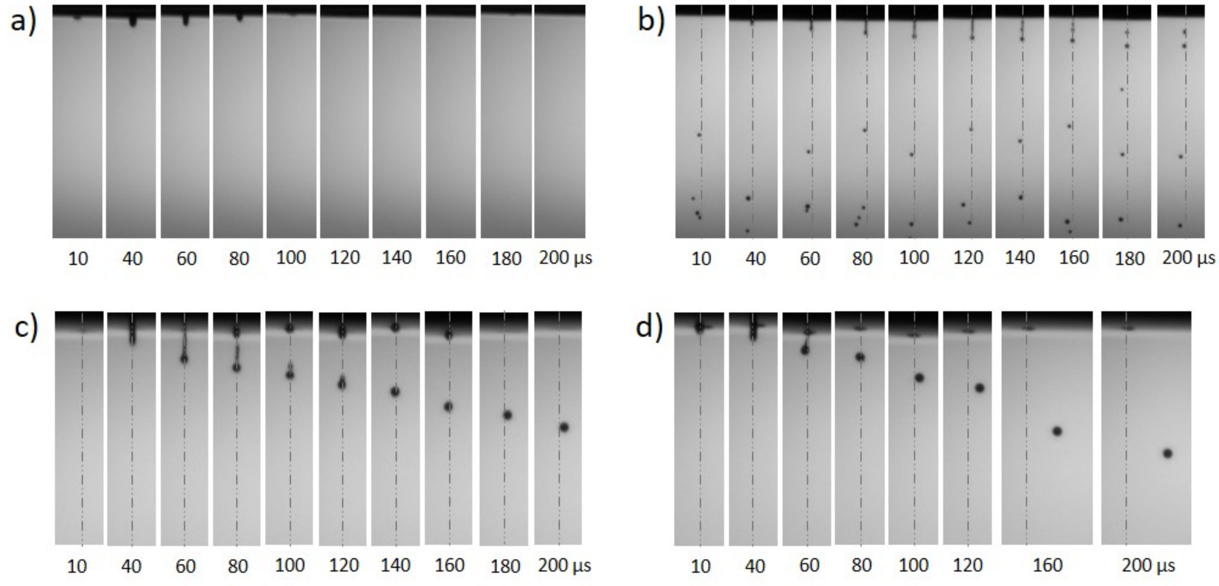

Figure 5.14: Drop generation process at different stages for: a) INK_HB, b) INK_LB, c) INK_CMC, d) INK_PEDOT.

Table 5.3 shows the resulting values of the optimized electric pulse design for each type of ink.

Table 5.3: Optimized electric pulse designs for all formulated cathode inks.

Ink	Voltage (V)	Jetting frequency (Hz)	t_{rise} (µs)	t_{dwell} (µs)	t_{fall} (µs)
INK_HB	120	1000	5	5	5
INK_LB	120→60	1000	2	5	2
INK_CMC	50	1000	2	2	2
INK_PEDOT	80	1000	2	11	2

In the following sections, the results of printability tests are discussed separately as a function of the binder.

5.2.1 INK_HB

For INK_HB, the maximum voltage of 120 V was applied, but the ejection of a single droplet was impossible. In Figure 5.14a it is observable that initially, the ink attempted to pass through the nozzle, but after 80 µs, the fluid was driven back into the cartridge. The strain hardening was believed to be the cause of this effect. A schematic representation of this phenomenon is shown in Figure 5.15. Prior to ejection, the polymeric chains exist in a coiled state as no stress is applied. When the actuation pulse is delivered to the system, the piezoelectric material deforms, propelling the ink through the nozzle at frequencies ranging from 10 to 100 kHz [239]. As a result, the polymeric chains become aligned and stretched out, which indicates a coil-stretch transition. This leads to a significant increase in hydrodynamic drag force, which impedes the fluid flow [240], [241]. The intensity of this phenomenon is influenced by the molecular weight and concentration of the polymer, with higher molecular weight/concentration resulting in a more pronounced strain hardening effect [242], [243].

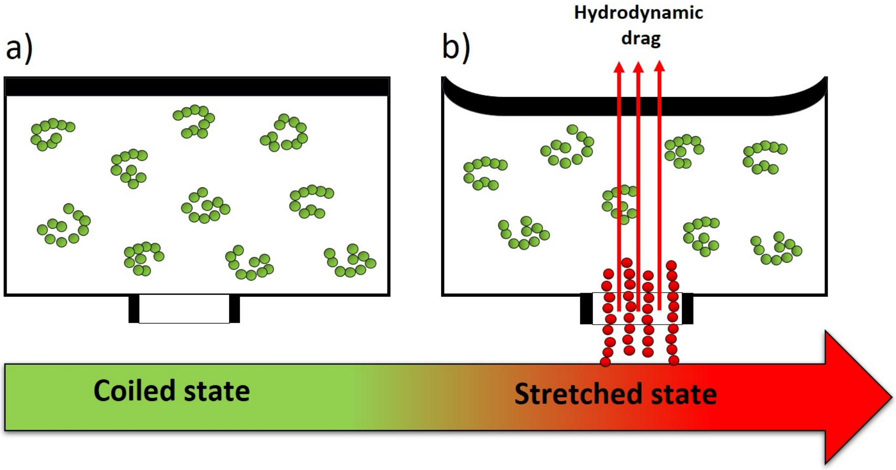

Figure 5.15: Schematic representation of strain hardening phenomenon: a) coiled state of polymeric chains, when no stress is applied, b) stretched state of polymeric chains during the ejection [101].

As previously mentioned, inks inside the cartridge are exposed to high frequencies. Nevertheless, there are challenges in accurately characterizing the rheological properties of these inks under such conditions. The frequencies typically accessible in commercial rheometers are considerably lower, often by several orders of magnitude than those encountered in inkjet printers.

To gain an idea about the behavior of the binder used for the formulation of INK_HB, its behavior was simulated by the frequency sweep test. HB binder was subjected to frequencies ranging from 1 to 80 Hz, and the variations in the loss and storage modulus were recorded. The outcomes are depicted in Figure 5.16.

At a frequency of 80 Hz, the storage modulus (563 Pa) showed a slight excess over the loss modulus (470 Pa), suggesting that the binder exhibited more solid-like behavior rather than liquid-like behavior. While the discrepancy between these two values was not substantial, it could be speculated that higher frequencies may lead to a more pronounced divergence. Therefore, the frequency sweep test can serve as a confirmation of the occurrence of strain hardening. The storage modulus surpassing the value of the loss modulus suggested that the polymer may be in a stretched state, impeding its ejection.

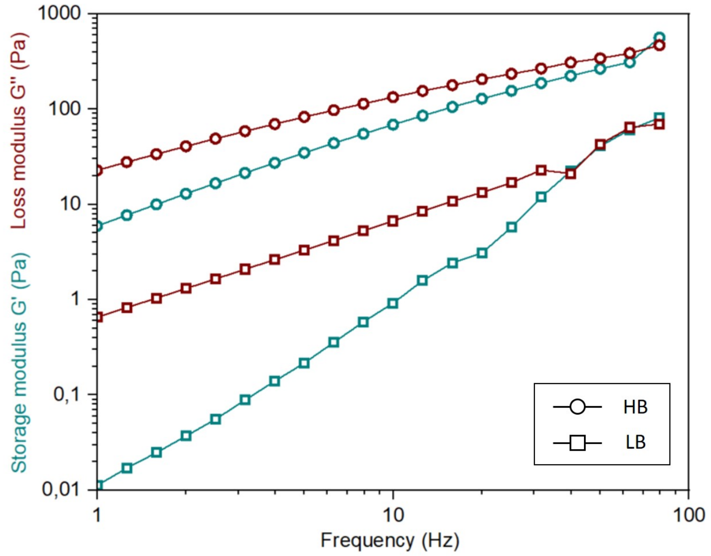

Figure 5.16: Frequency sweep test: storage modulus G’ and loss modulus G” as a function of frequency for HB and LB binders. The measurements were performed using Discovery Hybrid Rheometer HR-2 with a titanium cone plate geometry.

5.2.2 INK_LB

To initiate the ejection of INK_LB, the high value of 120 V had to be applied, followed by the reduction down to 60 V. This could be linked to "first drop problem" (FDP), which refers to the abnormal behavior of the first few droplets after the nozzle was sitting idle [244]. FDP was likely caused by the ink evaporation at the nozzle exit. As a result, the initial ejection settings for the process varied.

Although for the formulation of INK_LB, the same type of binder was used as for the preparation of INK_HB, the ejection was possible. To understand the distinct behaviors, the frequency sweep test was also conducted for LB (see Figure 5.16). Similarly to HB, at high frequency, the storage modulus (81 Pa) was greater than the loss modulus (70 Pa), but their values were much lower. It was hypothesized that shorter polymer chains may not generate sufficient hydrodynamic drag force to hinder the jetting process.

Nevertheless, the drop generation process was unstable, with numerous droplets lacking axisymmetry. Additionally, it was observed that after some time of printing (a few minutes), ejection was disrupted. It might be brought on by the low surface tension of the ink, which in consequence, can spread as a thin layer on the nozzle plate. After evaporation, further solidification modifies the droplet's trajectory or even prevents jetting [134].

5.2.3 INK_CMC and INK_PEDOT

INK_CMC and INK_PEDOT yielded stable individual droplets without any accompanying satellites. However, in both cases, the droplets lacked axisymmetry, and this was more evident for INK_PEDOT. Moreover, the nozzles were clogged after a few minutes of printing. Possible reasons for the instabilities include large agglomeration of powders, progressive deposition of thin multilayer of ink on the nozzle surface, air bubbles entrapment, or viscoelasticity, which were already discussed in Chapter 4 (Section 4.2.1, page 116). It should be pointed out that the deviation of the drop trajectory was not predictable. The droplets were subjected to shift in both directions to a different extent, and Figure 5.14 shows only an example of the drop generation process. However, larger deflections were recorded for INK_PEDOT compared to INK_CMC, which may be explained by a more complex structure of PEDOT:PSS contrary to CMC.

5.3 Microstructural characterization of printed patterns

Despite the challenge posed by the unstable ejection process, which hindered printing efficiency, cathode inks' deposition was demonstrated. Inkjet printing was carried out using only a single nozzle.

To show the patternability of IJP technique, the IRCER name was printed on aluminum foil using INK_CMC (see Figure 5.17). The text was successfully deposited proving the possibilities of inkjet printing at this scale.

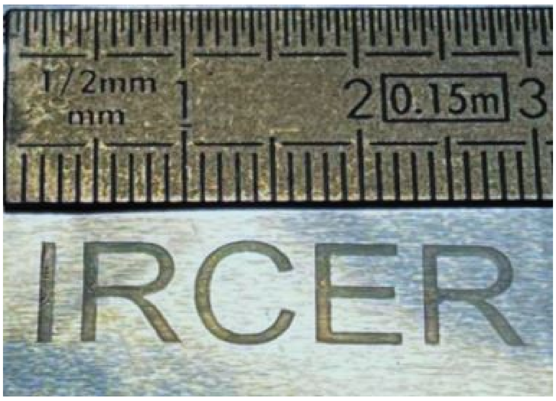

Figure 5.17: Photograph of the IRCER name printed with INK_CMC.

5.3.1 Printing of thin layers

To demonstrate the possibilities of printing thin coatings using IJP, cathode layers were deposited on aluminum foil with the droplets overlapping by 25 µm and the temperature of the substrate holder set at 50°C. The squares of 1x1cm were printed, each made up of 10 layers deposited one upon the other.
FIB cross-section images of inkjet printed planar structures fabricated with INK_LB, INK_CMC, and INK_PEDOT are presented in Figure 5.18.

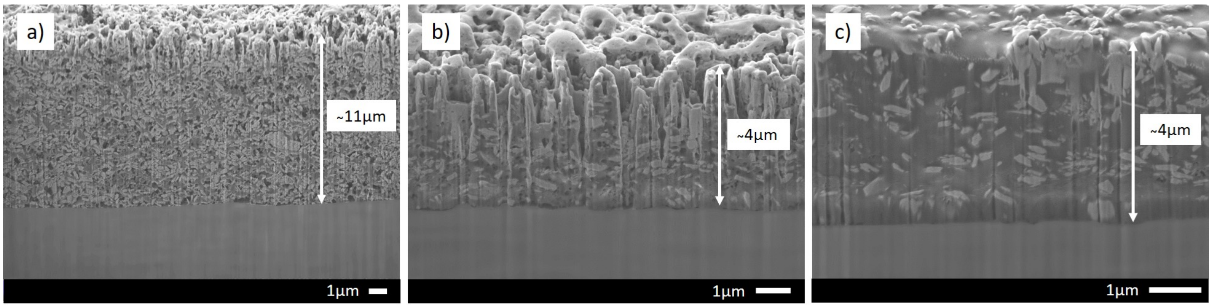

Figure 5.18: FIB cross-section images of inkjet printed planar structures fabricated with:
a) INK_LB, b) INK_CMC, c) INK_PEDOT.

The film of INK_LB is much thicker than those of INK_CMC and INK_PEDOT. For the latter two, the drop formation process was more stable with one drop generated one after another. For INK_LB, many droplets were ejected from the nozzle at the same time, leading to a higher deposition rate. Within each coating, powders were evenly distributed creating a connected network between the active material and the conductive agent, which may be beneficial for the electrochemical performance. Unfortunately, since the printing was not reproducible and the nozzle clogging occurred repeatedly, it was challenging to produce the samples for electrochemical testing.

However, it should be mentioned that using IJP, cathode layers containing CMC were successfully deposited without cracking. The inclusion of latex, which was suspected to negatively affect electrochemical performance, was unnecessary for ink formulation. As previously mentioned in Chapter 4, employing the layer-by-layer printing technique allows for the drying of individual layers before advancing to the subsequent ones. This method mitigates stress accumulation and diminishes the probability of cracking by providing ample drying time for the ink.

5.3.2 Printing of 3D structures

As for printing of 3D anode structures (see Chapter 4), the pillars were built by deposition of single splats one on top of each other. Due to the relatively stable drop generation processes observed only with INK_CMC and INK_PEDOT, the experiments were conducted exclusively with these two inks.

SEM observations of single splats are presented in Figure 5.19. Those deposited with INK_CMC (Figure 5.19a) were evenly distributed on Al foil, creating a uniform pattern. As for INK_PEDOT, there was a chaotic arrangement of splats, with no visible order, which could be foreseen by the printability tests (see Figure 5.14).

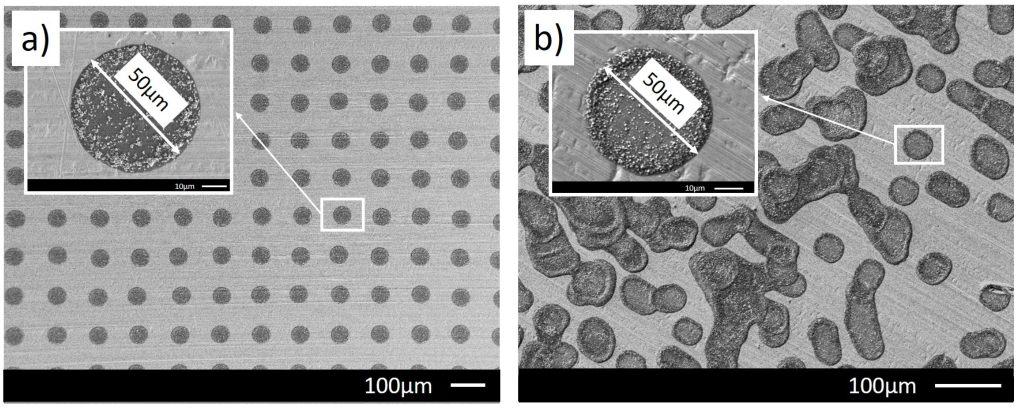

Figure 5.19: SEM observations of single splats deposited with: a) INK_CMC, b) INK_PEDOT.

In both cases, the diameter of a single droplet after drying was around 50 µm. Looking closely at the images of an isolated splat, it was visible that there was not much active material within it, which is due to the need for low viscous inks.

In order to build the 3D cathode architecture, the pattern was repeated 20 times, depositing a layer of ink on top of the other. Given the unstable jetting behavior of INK_PEDOT (see Figure 5.19b), the 3D structure was built only with INK_CMC.

Initially, the substrate holder was heated up to 40°C, so that the previously deposited layer might be dried before the following droplets were ejected. Figure 5.20a presents SEM image of the resulted pattern, and Figure 5.20b shows closer a single pillar.

It was observable that on the edges more material was loaded, leading to a crater in the center. As already mentioned, this phenomenon is called the coffee-ring effect and it is an issue that frequently arises during the drying of particle-laden droplets.

In Figure 5.20c, SEM image of the pattern printed with the temperature of the substrate holder set at 60°C is presented, and Figure 5.20d shows the structure of a single pillar. The coffee-ring effect was successfully diminished. However, in either case, the deposited rods lost a circular shape. Compared to single splats, they were non-symmetric, and their widths were 90 µm and 82 µm for 40°C and 60°C, respectively. Although INK_CMC exhibited quite satisfactory jetting behavior, there was still a little trajectory deviation leading to poor printing quality.

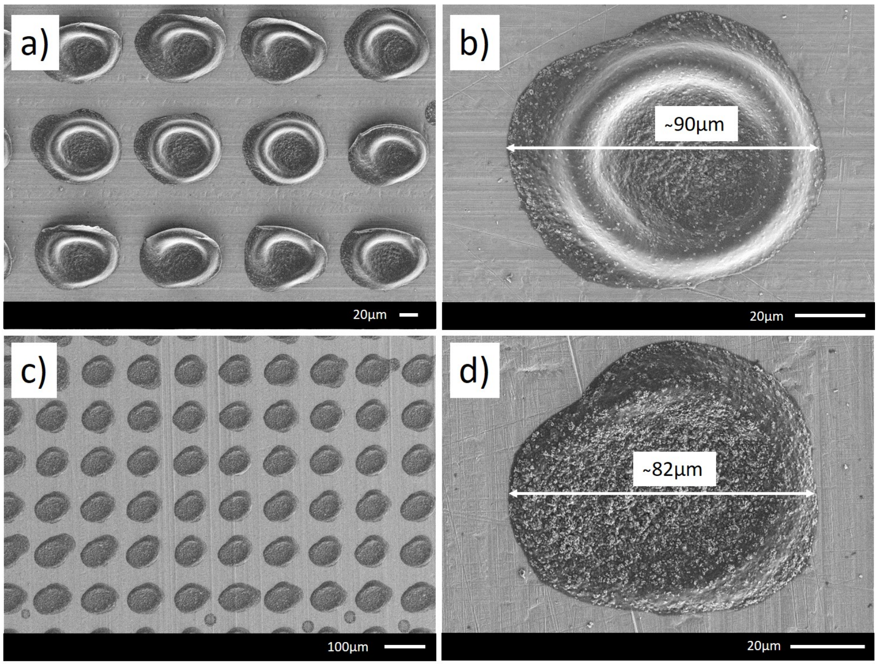

Figure 5.20: SEM observations of deposited 3D structures with INK_CMC: a) pillars deposited with the substrate holder temperature of 40°C, b) single pillar deposited with the substrate holder temperature of 40°C, c) pillars deposited with the substrate holder temperature of 60°C, d) single pillar deposited with the substrate holder temperature of 60°C.

In order to obtain a more comprehensive understanding of the printed pillar shapes, 3D microscope was used for visualizing the structures. Figure 5.21a confirms the coffee-ring effect occurring for the printing with the temperature of 40°C.

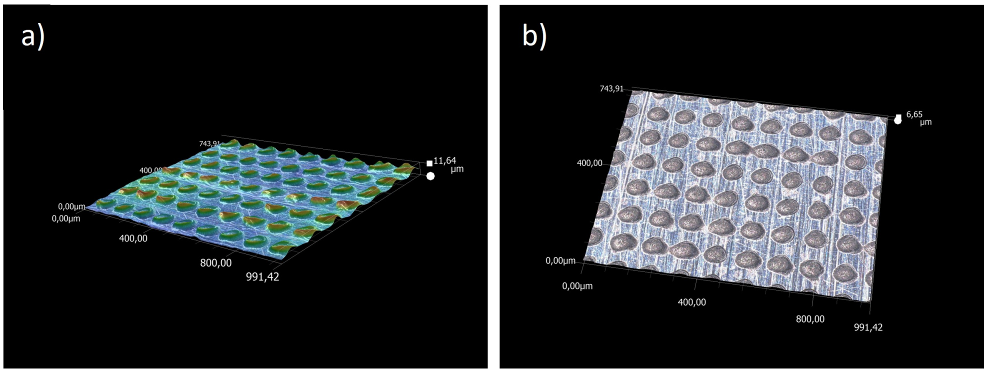

Figure 5.21: 3D microscope images of pillars deposited with INK_CMC and with the temperature of the substrate holder set at: a) 40°C, b) 60°C.

The maximum height of the edges was around 12 µm. With the temperature of 60°C, the material was more homogeneously distributed within the pillars and their height was around 7 µm (see Figure 5.21b).

5.4 Emission measurements

The assessment of potential health risks associated with ink formulation and inkjet printing of cathode inks followed the same procedure as that used for the anode inks (see Section 4.4, page 126).

The analyses were performed on ink samples that included CMC as a binder, i.e. INK_CMC. The particle number concentrations during cathode ink formulation for nanoparticles and microparticles are presented in Figure 5.22a, and Figure 5.22b, respectively.

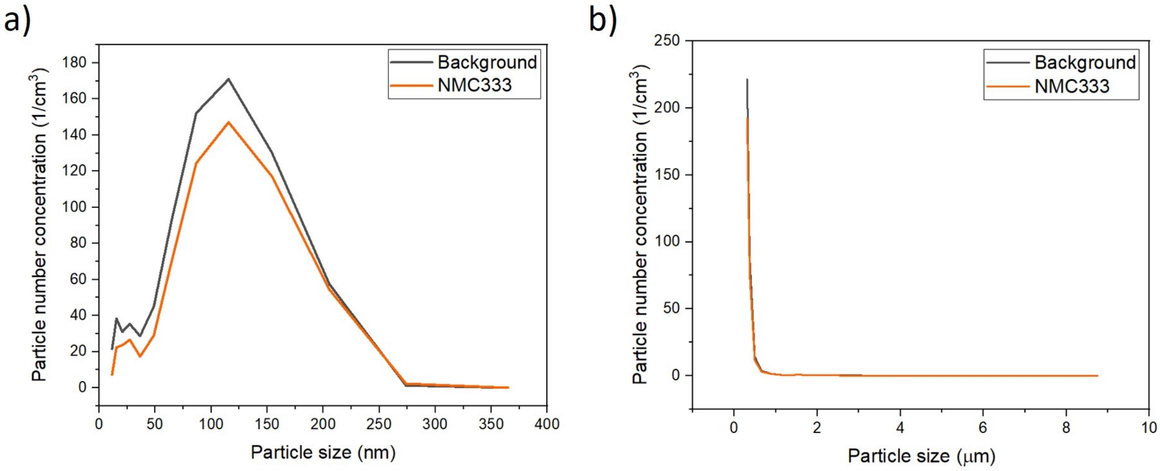

Figure 5.22: The particle number concentrations per cm^3 during cathode ink formulation for: a) nanoparticles, b) microparticles.

In the case of both nanoparticles and microparticles, it was observed that the background particle number concentration exceeded that during the ink formulation process. Since this difference lacks physical or practical significance, it is likely that this variation can be attributed to measurement accuracy.

Figure 5.23 illustrates the particle number concentrations during the inkjet printing of cathode ink. The background particle number concentration was higher than the particle emission during the process for both, nanoparticles and microparticles. Once more, it is probable that this discrepancy can be attributed to measurement accuracy.

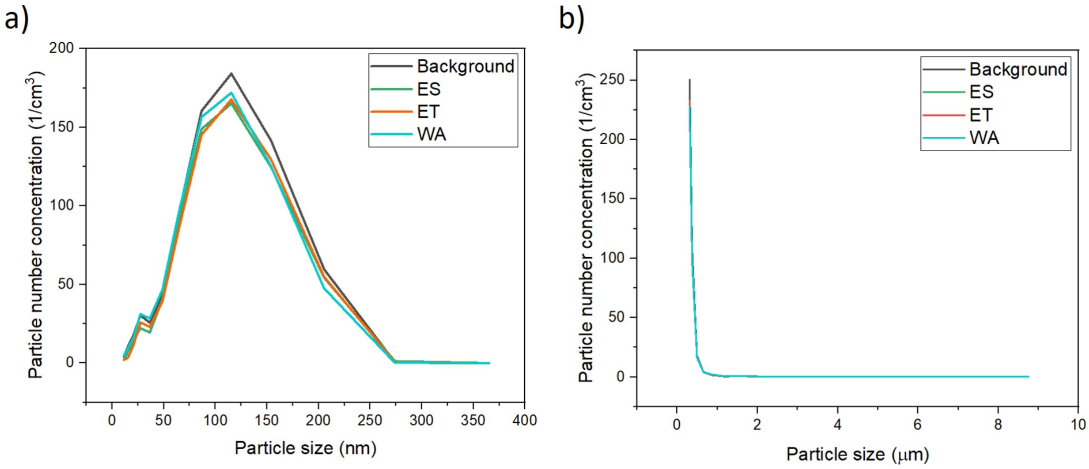

Figure 5.23: The particle number concentrations per cm^3 during inkjet printing of cathode ink for: a) nanoparticles, b) microparticles. ES - Emission Source, ET - Exhaust Tube, WA - Worker Area.

The results suggested that both the ink formulation and inkjet printing processes of the cathode exhibit no particle release. Consequently, these processes do not pose any risks to human health.

5.5 Conclusions

Stable cathode inks with NMC333 as active material, specifically designed for inkjet printing were successfully developed. The measurements of the particle emission during the cathode ink formulation and inkjet printing process showed that the procedures do not pose any risks to human health.

The impact of water exposure on the properties of NMC333 was evaluated, revealing no structural changes and only minimal leaching of Li. This assessment indicates that aqueous processing could be a viable and environmentally advantageous option for NMC333 powder.

The electrochemical analyses demonstrated that the electrodes fabricated with CMC as a binder were unable to store any electrical charge or deliver any energy. This could be attributed to either the influence of CMC itself or the presence of latex. Cathodes formulated with HB and LB displayed pronounced aging. After 100 cycles, CATHODE_HB demonstrated around 25% capacity retention, while the specific capacity of CATHODE_LB declined to nearly 0mAh/g, just after formation. The difference in the cycling behavior of CATHODE_HB, and CATHODE_LB was most likely attributed to the utilization of different binders with distinct structures. As previously mentioned, CATHODE_LB, with its shorter polymeric chains, was unable to establish a continuous network within the cathode. Printability tests demonstrated process instabilities, which lead to poor printing quality. Moreover, the strain hardening phenomenon was observed emphasizing the importance of considering the polymer nature when formulating inks.

Despite the challenge posed by the unstable ejection process, cathode inks' deposition was demonstrated. Thin layers of INK_LB, INK_CMC, and INK_PEDOT were successfully deposited. Unwanted additives such as latex, which were suspected to have a detrimental impact on electrochemical performance, were found to be unnecessary for the formulation of CMC-based inks designed for IJP. The different drying conditions in IJP, as opposed to tape-casted electrodes, enabled the achievement of uniform layers without the need for such additives.

The printing of 3D structures was demonstrated showing the potential for building micropillars with INK_CMC. However, due to the process instabilities (nozzle clogging, drop trajectory deviation), it was challenging to create well-defined structures on a larger scale, that could be electrochemically tested.

As already discussed in Chapter 4, in order to tackle these challenges, additional improvements in the technology are required, with a particular focus on mitigating nozzle clogging (non-adsorbing coatings on the nozzle surface, integration of a cleaning unit).

Summary:

- Stable cathode inks, specifically designed for inkjet printing were successfully developed, and the particle emission measurements confirmed that the preparation procedure and inkjet printing pose no risks to human health.
- The evaluation of water exposure on NMC333 properties showed no structural changes and minimal Li leaching, suggesting that aqueous processing of NMC333 powder could be a feasible and environmentally beneficial choice.
- Printability tests demonstrated the instabilities of the drop generation process and also revealed the strain-hardening phenomenon, which hinders the ejection.
- Thin layers of INK_LB, INK_CMC, and INK_PEDOT were successfully deposited. Latex could be excluded from the formulation of CMC-based cathode, without the risk of electrode cracking.
- Instabilities of the ejection process posed a challenge for printing well-defined 3D cathode structures.
- To enhance printing accuracy and stability of the process, additional improvements in the technology are required.

6

General conclusions

This thesis aimed to investigate the opportunities and challenges associated with manufacturing 3D electrodes for modern lithium-ion batteries using inkjet printing technology. Given the continuous expansion of the Li-ion battery market, there is a notable interest in developing a new generation of batteries with enhanced properties. One of the potential paths for advancement is 3D electrode architecture, which has the potential to supply higher energy density and higher power density compared to conventional laminated structures. As inkjet printing offers numerous advantages (high resolution, high speed of deposition,...), we studied the possibilities of implementing this technology in the battery industry.

We examined the key steps of the process: powders preparation, functional ink formulations, and inkjet printing. Throughout our research, we encountered a few main issues that limit the application of inkjet printing.

Firstly, we had to adapt the granulometry of NMC622 cathode powder to meet the requirements of the printer. In order to avoid the nozzle clogging, the particle size of the powder had to be in the submicron range. Consequently, we evaluated the effectiveness of three different grinding techniques and found that high-energy ball milling produced the most satisfactory outcomes. However, this grinding process led to the deterioration of the electrochemical performance of NMC622. By examining the XRD patterns, we identified crystal defects, and consequently induced lattice microstrains in the structure, as the main cause. To address this issue, we proposed thermal treatments of the powder as a potential method of restoring the initial crystal structure. Unfortunately, these changes proved to be irreversible.
Therefore, we concluded that when nanopowders are necessary for electrode shaping, such as in inkjet printing, it is advisable to purchase NMC raw powders with appropriate granulometry to maintain optimal electrochemical performance. Furthermore, our results emphasized the significance of selecting suitable mixing methods during the preparation of the electrode slurry.

In the subsequent part of our work, we demonstrated the step-by-step preparation procedures of functional electrode inks, specifically designed for IJP, but also adaptable for other wet-processing techniques. We carried out printability tests, which revealed the process instabilities appearing as the loss of the droplets axisymmetry, simultaneous generation of multiple droplets, and nozzle clogging. Our investigations into anode fabrication underscored the significance of powder surface chemistry. Notably, inks comprising pure Si as the active material exhibited ejectability, whereas those containing Si$\mathit{\Omega}$C resulted in immediate nozzle clogging. The underlying cause of this ejection challenge could be attributed to the formation of bonds between the surface of silicon particles and the hydroxyl groups present on the metal surface of the printing nozzles. On the other hand, while investigating the possibilities of cathode inkjet printing, we observed the strain-hardening phenomenon, which may impede the process. These observations proved that piezoelectric inkjet printer poses some limitations in the choice of materials used.

Despite facing many challenges, we showed that inkjet printing of electrode structures is feasible. However, it is important to acknowledge that this method is not without limitations. We successfully optimized the printing parameters and deposited thin layers of anode and cathode. Nevertheless, the optimal parameters necessitated an extensive fabrication time, which is unacceptable for mass production purposes.
The construction of 3D structures posed significant difficulties. Although we successfully deposited the initial layer of splats with a satisfactory resolution, subsequent droplets were not placed with the desired precision. Consequently, the inkjet printing of well-ordered microstructures of electrodes proved to be unattainable wit the formulated inks.

Through our study, we have demonstrated the necessity of considering numerous factors when formulating inks. Firstly, careful attention must be given to the particle size of powders to prevent nozzle clogging. Subsequently, the formulation process demands meticulous consideration to achieve optimal stability. Furthermore, the rheological properties of the inks must be adjusted to align with the specific requirements of the printer. Additionally, if a polymeric binder is employed, its behavior during ejection should be evaluated to avoid the strain-hardening phenomenon. Last but not least, the surface chemistry of powders necessitates consideration to prevent undesired interactions with the printhead material. While we have highlighted a few challenges encountered in our research, we acknowledge that additional obstacles may arise in this domain.

Moreover, it is important to note that even if the ink formulation satisfies all the required aspects and is ejectable, it does not necessarily guarantee a stable process. The fabrication of a well-defined 3D structure can still pose significant challenges.

A more comprehensive analysis is needed to gain a better understanding of the underlying mechanisms behind the ejection issues. We acknowledge that certain parts of our study should be further explored. However, due to confidentiality reasons, certain examinations cannot be publicly disclosed.

Furthermore, we believe that modifications to the printheads could potentially address some of the encountered challenges. For instance, applying a coating to the nozzle plate may mitigate interactions with the inks. Another potential solution involves implementing a cleaning unit that periodically unclogs the nozzles.

In conclusion, we assert that there is still room for improvement before the practical application of DOD piezoelectric inkjet printing in the manufacturing of LIBs electrodes. The main issue centers around nozzle clogging, which suggests the exploration of alternative material jetting techniques such as acoustic inkjet printing or aerosol jet printing.

7

Bibliography

Summary

References

[1] B. Pandey and K. K. Choudhary, "Air pollution: role in climate change and its impact on crop plants," in *Climate change and agricultural ecosystems*, Elsevier, 2019, pp. 211–247.

[2] E. U. S. E. P. Agency, *Overview of greenhouse gases*, `https://www.epa.gov/ghgemissions/overview-greenhouse-gases`, Accessed: 2022-12-18.

[3] P. Transport IEA, *IEA 2022*, `https://www.iea.org/reports/transport`, Accessed: 2022-12-18.

[4] M. A. Tamor and E. B. Stechel, "Electrification of transportation means a lot more than a lot more electric vehicles," *iScience*, vol. 25, no. 6, p. 104 376, 2022.

[5] UN-FCCC, *COP26 the Glasgow climate pact, United Nations International Framework Convention on Climate Change (2021)*, `https://ukcop26.org/wp-content/uploads/2021/11/COP26-Presidency-Outcomes-The-Climate-Pact.pdf`, Accessed: 2022-12-18.

[6] S. S. Rangarajan, S. P. Sunddararaj, A. Sudhakar, *et al.*, "Lithium-ion batteries—the crux of electric vehicles with opportunities and challenges," *Clean Technologies*, vol. 4, no. 4, pp. 908–930, 2022.

[7] M. Armand, P. Axmann, D. Bresser, *et al.*, "Lithium-ion batteries-Current state of the art and anticipated developments," *Journal of Power Sources*, vol. 479, p. 228 708, 2020.

[8] W. Li, E. M. Erickson, and A. Manthiram, "High-nickel layered oxide cathodes for lithium-based automotive batteries," *Nature Energy*, vol. 5, no. 1, pp. 26–34, 2020.

[9] F. Schipper, E. M. Erickson, C. Erk, J.-Y. Shin, F. F. Chesneau, and D. Aurbach, "Recent advances and remaining challenges for lithium ion battery cathodes," *Journal of the Electrochemical Society*, vol. 164, no. 1, p. 6220, 2016.

[10] L. Sun, Y. Liu, R. Shao, J. Wu, R. Jiang, and Z. Jin, "Recent Progress and Future Perspective on Practical Silicon Anode-Based Lithium Ion Batteries," *Energy Storage Materials*, 2022.

[11] W.-F. Ren, Y. Zhou, J.-T. Li, L. Huang, and S.-G. Sun, “Si anode for next-generation lithium-ion battery,” *Current Opinion in Electrochemistry*, vol. 18, pp. 46–54, 2019.

[12] Y. Yang, S. Wu, Y. Zhang, *et al.*, “Towards efficient binders for silicon based lithium-ion battery anodes,” *Chemical Engineering Journal*, vol. 406, p. 126 807, 2021.

[13] J. W. Long, B. Dunn, D. R. Rolison, and H. S. White, “Three-dimensional battery architectures,” *Chemical Reviews*, vol. 104, no. 10, pp. 4463–4492, 2004.

[14] Y. Zhu, J. Li, M. S. Saleh, *et al.*, “Towards high-performance Li-ion batteries via optimized three-dimensional micro-lattice electrode architectures,” *Journal of Power Sources*, vol. 476, p. 228 593, 2020.

[15] L. Li, H. Tan, X. Yuan, *et al.*, “Direct ink writing preparation of $\mathrm{LiFePO}_4/MWCNTselectrodeswit$ $arealLi - ioncapacity$,” *Ceramics International*, vol. 47, no. 15, pp. 21 161–21 166, 2021.

[16] A. Maurel, S. Grugeon, B. Fleutot, *et al.*, “Three-dimensional printing of a LiFePO_4/graphite battery cell via fused deposition modeling,” *Scientific reports*, vol. 9, no. 1, pp. 1–14, 2019.

[17] Y. He, S. Chen, L. Nie, Z. Sun, X. Wu, and W. Liu, “Stereolithography three-dimensional printing solid polymer electrolytes for all-solid-state lithium metal batteries,” *Nano Letters*, vol. 20, no. 10, pp. 7136–7143, 2020.

[18] L. J. Deiner, T. Jenkins, A. Powell, T. Howell, and M. Rottmayer, “High Capacity Rate Capable Aerosol Jet Printed Li-Ion Battery Cathode,” *Advanced Engineering Materials*, vol. 21, no. 5, p. 1 801 281, 2019.

[19] C. C. Ho, K. Murata, D. A. Steingart, J. W. Evans, and P. K. Wright, “A super ink jet printed zinc-silver 3D microbattery,” *Journal of Micromechanics and Microengineering*, vol. 19, no. 9, p. 094 013, 2009.

[20] R. Noguera, M. Lejeune, and T. Chartier, “3D fine scale ceramic components formed by ink-jet prototyping process,” *Journal of the European Ceramic Society*, vol. 25, no. 12, pp. 2055–2059, 2005.

[21] B. Derby and N. Reis, “Inkjet printing of highly loaded particulate suspensions,” *MRS bulletin*, vol. 28, no. 11, pp. 815–818, 2003.

[22] Fujifilm, *Printhead Reference Chart PDS00015*, `https://asset.fujifilm.com/www/nl/files/2020-03/171afe178b58bf4b7833bf9435b81c27/PDS00015.pdf`, Accessed: 2022-09-28.

[23] M. Pei, H. Shi, F. Yao, *et al.*, “3D printing of advanced lithium batteries: A designing strategy of electrode/electrolyte architectures,” *Journal of Materials Chemistry A*, vol. 9, no. 45, pp. 25 237–25 257, 2021.

[24] D. A. Aksyonov and V. A. Nikitina, "Charge transfer through interfaces in metal-ion intercalation systems," *Comprehensive Inorganic Chemistry III*, 2021.

[25] E. C. Evarts, "Lithium batteries: To the limits of lithium," *Nature*, vol. 526, no. 7575, pp. 93–95, 2015.

[26] J.-M. Tarascon and M. Armand, "Issues and challenges facing rechargeable lithium batteries," in *Materials for sustainable energy: a collection of peer-reviewed research and review articles from Nature Publishing Group*, World Scientific, 2011, pp. 171–179.

[27] R. J. Brodd, K. R. Bullock, R. A. Leising, R. L. Middaugh, J. R. Miller, and E. Takeuchi, "Batteries, 1977 to 2002," *Journal of the Electrochemical Society*, vol. 151, no. 3, p. 1, 2004.

[28] D. Choi, W. Wang, and Z. Yang, "Material Challenges and Perspectives," *Lithium-Ion Batteries: Advanced Materials and Technologies*, vol. 1, 2011.

[29] D. Pavlov, "Chapter 1 - Invention and Development of the Lead–Acid Battery," in *Lead-Acid Batteries: Science and Technology*, D. Pavlov, Ed., Amsterdam: Elsevier, 2011, pp. 3–28.

[30] S. Vepachedu, "The history of electric car," *Andhra Journal of Industrial News*, pp. 14–27, Sep. 2017.

[31] V. C. Manz, *A Short History of Electric Vehicles*, `https://www.zf.com/mobile/en/stories_9473.html`, Accessed: 2021-09-07.

[32] ElectricVehiclesNews, *History Electric Vehicles News History of Electric Vehicles*, `https://www.electricvehiclesnews.com/History/historyearlyIII.html`, Accessed: 2021-09-07.

[33] L. Project, *History of electric vehicles*, `https://www.lemo-project.eu/wp-content/uploads/2015/01/History-of-electric-cars.pdf`, Accessed: 2021-09-13, 2015.

[34] N. Burton, *History of electric cars*. Crowood, 2013.

[35] MyAutorWorld, *Ford Model T 1908 to 1927*, `https://myautoworld.com/ford/history/ford-t/ford-t.html`, Accessed: 2021-09-07, 2015.

[36] L. Paoli, "Electric vehicles," IEA, 2022.

[37] F. Mizuno, C. Yada, and H. Iba, "Solid-state lithium-ion batteries for electric vehicles," in *Lithium-Ion Batteries*, Elsevier, 2014, pp. 273–291.

[38] *For a livable climate: Net-zero commitments must be backed by credible action*, `https://www.un.org/en/climatechange/net-zero-coalition`, Accessed: 2022-01-04.

[39] B. N. E. Finance, “Electric vehicle outlook 2017,” *Bloomberg Finance LP, Tech. Rep*, 2017.

[40] J. Deng, C. Bae, A. Denlinger, and T. Miller, “Electric vehicles batteries: requirements and challenges,” *Joule*, vol. 4, no. 3, pp. 511–515, 2020.

[41] A. Dinger, R. Martin, X. Mosquet, *et al.*, “Batteries for electric cars: Challenges, opportunities, and the outlook to 2020,” *The Boston Consulting Group*, vol. 7, p. 2017, 2010.

[42] M. S. Whittingham, “Chemistry of intercalation compounds: Metal guests in chalcogenide hosts,” *Progress in Solid State Chemistry*, vol. 12, no. 1, pp. 41–99, 1978.

[43] M. S. Whittingham, “Electrical energy storage and intercalation chemistry,” *Science*, vol. 192, no. 4244, pp. 1126–1127, 1976.

[44] D. Monroe, “Building a better battery,” *MRS Bulletin*, vol. 45, no. 3, pp. 246–247, 2020.

[45] K. Mizushima, P. Jones, P. Wiseman, and J. B. Goodenough, “Li_xCoO_2 (0 $<$ x $<$ -1): A new cathode material for batteries of high energy density,” *Materials Research Bulletin*, vol. 15, no. 6, pp. 783–789, 1980.

[46] M. Thackeray, W. David, P. Bruce, and J. Goodenough, “Lithium insertion into manganese spinels,” *Materials Research Bulletin*, vol. 18, no. 4, pp. 461–472, 1983.

[47] M. Thackeray, P. Johnson, L. de Picciotto, P. Bruce, and J. Goodenough, “Lithium extraction from $LiMn_2O_4$,” *Mater Res Bull*, vol. 19, pp. 179–187, 1984.

[48] A. K. Padhi, K. S. Nanjundaswamy, and J. B. Goodenough, “Phospho-olivines as positive-electrode materials for rechargeable lithium batteries,” *Journal of the electrochemical society*, vol. 144, no. 4, p. 1188, 1997.

[49] C. Daniel, D. Mohanty, J. Li, and D. L. Wood, “Cathode materials review,” in *AIP Conference Proceedings*, American Institute of Physics, vol. 1597, 2014, pp. 26–43.

[50] T. Zhang, D. Li, Z. Tao, and J. Chen, “Understanding electrode materials of rechargeable lithium batteries via DFT calculations,” *Progress in Natural Science: Materials International*, vol. 23, no. 3, pp. 256–272, 2013.

[51] T. Chen and R. Lin, “Effects of Metal Doping on Properties of $LiFePO_4$ Cathode Material by First-Principle Calculation,” *International Journal of Materials Engineering*, vol. 5, pp. 121–124, 2015.

[52] B. Scrosati, “Lithium rocking chair batteries: an old concept?” *Journal of The Electrochemical Society*, vol. 139, no. 10, p. 2776, 1992.

[53] M. Lazzari and B. Scrosati, “A cyclable lithium organic electrolyte cell based on two intercalation electrodes,” *Journal of The Electrochemical Society*, vol. 127, no. 3, p. 773, 1980.

[54] A. Yoshino, K. Sanechika, and T. Nakajima, “Secondary Battery, US Patent 4,668,595,” 1985.

[55] Y. Nishi, H. Azuma, and A. Omaru, “Non aqueous electrolyte cell,” *Patent US*, vol. 4959281, 1989.

[56] T. Degnan, *John goodenough’s encore battery*, 2017.

[57] D. N. Williams, “2018 Benjamin Franklin Medal in Chemistry presented to John B. Goodenough, Ph. D.,” *Journal of the Franklin Institute - Engineering and Applied Mathematics*, vol. 357, no. 5, pp. 2592–2594, 2020.

[58] Y. Lyu, X. Wu, K. Wang, *et al.*, “An Overview on the Advances of $LiCoO_2$ Cathodes for Lithium-Ion Batteries,” *Advanced Energy Materials*, vol. 11, no. 2, p. 2 000 982, 2021.

[59] A. Manthiram, “A reflection on lithium-ion battery cathode chemistry,” *Nature communications*, vol. 11, no. 1, pp. 1–9, 2020.

[60] A. Chakraborty, S. Kunnikuruvan, S. Kumar, *et al.*, “Layered Cathode Materials for Lithium-Ion Batteries: Review of Computational Studies on $LiNi_{1-x-y}Co_xMn_yO_2$ and $LiNi_{1-x-y}Co_xAl_yO_2$,” *Chemistry of Materials*, vol. 32, no. 3, pp. 915–952, 2020.

[61] A. Chakraborty, M. Dixit, and D. T. Major, “Accurate Cathode Properties of $LiNiO_2$, $LiCoO_2$, and $LiMnO_2$ Using the SCAN Meta-GGA Density Functional,” *npj Computational Materials*, 2018.

[62] W. Liu, P. Oh, X. Liu, *et al.*, “Nickel-rich layered lithium transition-metal oxide for high-energy lithium-ion batteries,” *Angewandte Chemie International Edition*, vol. 54, no. 15, pp. 4440–4457, 2015.

[63] N. A. Chernova, M. Ma, J. Xiao, M. S. Whittingham, J. Breger, and C. P. Grey, “Layered $Li_xNi_yMn_yCo_{1-2y}O_2$ Cathodes for Lithium Ion Batteries: Understanding Local Structure via Magnetic Properties,” *Chemistry of Materials*, vol. 19, no. 19, pp. 4682–4693, 2007.

[64] R. Chebiam, A. M. Kannan, F. Prado, and A. Manthiram, “Comparison of the chemical stability of the high energy density cathodes of lithium-ion batteries,” *Electrochemistry communications*, vol. 3, no. 11, pp. 624–627, 2001.

[65] S. Venkatraman, Y. Shin, and A. Manthiram, “Phase Relationships and Structural and Chemical Stabilities of Charged $Li_{1-x}CoO_{2-\delta}$ and $Li_{1-x}Ni_{0.85}Co_{0.15}O_{2-\delta}$ Cathodes,” *Electrochemical and Solid State Letters*, vol. 6, no. 1, p. 9, 2002.

[66] S. Yamada, M. Fujiwara, and M. Kanda, “Synthesis and properties of $LiNiO_2$ as cathode material for secondary batteries,” *Journal of Power Sources*, vol. 54, no. 2, pp. 209–213, 1995.

[67] G. Dutta, A. Manthiram, J. Goodenough, and J.-C. Grenier, “Chemical synthesis and properties of $Li_{1-\delta-x}Ni_{1+\delta}O_2$ and $Li[Ni_2]O_4$,” *Journal of Solid State Chemistry*, vol. 96, no. 1, pp. 123–131, 1992.

[68] G. Vitins and K. West, “Lithium intercalation into layered $LiMnO_2$,” *Journal of the Electrochemical Society*, vol. 144, no. 8, p. 2587, 1997.

[69] A. R. Armstrong and P. G. Bruce, “Synthesis of layered $LiMnO_2$ as an electrode for rechargeable lithium batteries,” *Nature*, vol. 381, no. 6582, pp. 499–500, 1996.

[70] T. Ohzuku and Y. Makimura, “Layered lithium insertion material of $LiCo_{1/3}Ni_{1/3}Mn_{1/3}O_2$ for lithium-ion batteries,” *Chemistry Letters*, vol. 30, no. 7, pp. 642–643, 2001.

[71] I. Belharouak, Y.-K. Sun, J. Liu, and K. Amine, “$Li(Ni_{1/3}Co_{1/3}Mn_{1/3})O_2$ as a suitable cathode for high power applications,” *Journal of Power Sources*, vol. 123, no. 2, pp. 247–252, 2003.

[72] S. Jaffe, “Vulnerable links in the lithium-ion battery supply chain,” *Joule*, vol. 1, no. 2, pp. 225–228, 2017.

[73] A. K. Stephan, “A Pathway to Understand NMC Cathodes,” *Joule*, vol. 4, no. 8, pp. 1632–1633, 2020.

[74] H.-J. Noh, S. Youn, C. S. Yoon, and Y.-K. Sun, “Comparison of the structural and electrochemical properties of layered Li $[Ni_xCo_yMn_z]O_2$ (x= 1/3, 0.5, 0.6, 0.7, 0.8 and 0.85) cathode material for lithium-ion batteries,” *Journal of power sources*, vol. 233, pp. 121–130, 2013.

[75] W. Xu, J. Wang, F. Ding, *et al.*, “Lithium metal anodes for rechargeable batteries,” *Energy & Environmental Science*, vol. 7, no. 2, pp. 513–537, 2014.

[76] C. M. Hayner, X. Zhao, and H. H. Kung, “Materials for rechargeable lithium-ion batteries,” *Annual review of chemical and biomolecular engineering*, vol. 3, pp. 445–471, 2012.

[77] H. Wu and Y. Cui, “Designing nanostructured Si anodes for high energy lithium ion batteries,” *Nano today*, vol. 7, no. 5, pp. 414–429, 2012.

[78] M. Obrovac and L. Christensen, “Structural changes in silicon anodes during lithium insertion/extraction,” *Electrochemical and solid-state letters*, vol. 7, no. 5, p. 93, 2004.

[79] K. Siczek, “Negative Electrode (Anode) Materials,” in Jan. 2019, pp. 117–131.

[80] X. Chen, K. Gerasopoulos, J. Guo, *et al.*, “A patterned 3D silicon anode fabricated by electrodeposition on a virus-structured current collector,” *Advanced Functional Materials*, vol. 21, no. 2, pp. 380–387, 2011.

[81] N. Dimov, S. Kugino, and M. Yoshio, “Carbon-coated silicon as anode material for lithium ion batteries: advantages and limitations,” *Electrochimica acta*, vol. 48, no. 11, pp. 1579–1587, 2003.

[82] H. Wu, G. Zheng, N. Liu, T. J. Carney, Y. Yang, and Y. Cui, “Engineering empty space between Si nanoparticles for lithium-ion battery anodes,” *Nano letters*, vol. 12, no. 2, pp. 904–909, 2012.

[83] F. Luo, B. Liu, J. Zheng, *et al.*, “Nano-silicon/carbon composite anode materials towards practical application for next generation Li-ion batteries,” *Journal of The Electrochemical Society*, vol. 162, no. 14, p. 2509, 2015.

[84] M. A. Rahman, G. Song, A. I. Bhatt, Y. C. Wong, and C. Wen, “Nanostructured silicon anodes for high-performance lithium-ion batteries,” *Advanced Functional Materials*, vol. 26, no. 5, pp. 647–678, 2016.

[85] M. Ko, S. Chae, and J. Cho, “Challenges in accommodating volume change of Si anodes for Li-ion batteries,” *ChemElectroChem*, vol. 2, no. 11, p. 1645, 2015.

[86] Y. Yang, W. Yuan, W. Kang, *et al.*, “Silicon-nanoparticle-based composites for advanced lithium-ion battery anodes,” *Nanoscale*, vol. 12, no. 14, pp. 7461–7484, 2020.

[87] H. Li, X. Huang, L. Chen, Z. Wu, and Y. Liang, “A high capacity nano Si composite anode material for lithium rechargeable batteries,” *Electrochemical and solid-state letters*, vol. 2, no. 11, p. 547, 1999.

[88] H. Kim, M. Seo, M.-H. Park, and J. Cho, “A critical size of silicon nano-anodes for lithium rechargeable batteries,” *Angewandte Chemie International Edition*, vol. 49, no. 12, pp. 2146–2149, 2010.

[89] C. K. Chan, H. Peng, G. Liu, *et al.*, “High-performance lithium battery anodes using silicon nanowires,” *Nature nanotechnology*, vol. 3, no. 1, pp. 31–35, 2008.

[90] N. Liu, L. Hu, M. T. McDowell, A. Jackson, and Y. Cui, “Prelithiated silicon nanowires as an anode for lithium ion batteries,” *ACS nano*, vol. 5, no. 8, pp. 6487–6493, 2011.

[91] M.-H. Park, M. G. Kim, J. Joo, *et al.*, “Silicon nanotube battery anodes,” *Nano letters*, vol. 9, no. 11, pp. 3844–3847, 2009.

[92] H. Li, X. Huang, L. Chen, *et al.*, “The crystal structural evolution of nano-Si anode caused by lithium insertion and extraction at room temperature,” *Solid State Ionics*, vol. 135, no. 1-4, pp. 181–191, 2000.

[93] Y. Chen, X. Li, L. Zhou, Y. W. Mai, and H. Huang, “High-performance electrospun nanostructured composite fiber anodes for lithium-ion batteries,” in *Multifunctionality of Polymer Composites: Challenges and New Solutions*, Elsevier Inc., 2015, pp. 662–689.

[94] C.-C. Hsieh, Y.-G. Lin, C.-L. Chiang, and W.-R. Liu, “Carbon-coated porous Si/C composite anode materials via two-step etching/coating processes for lithium-ion batteries,” *Ceramics International*, vol. 46, no. 17, pp. 26 598–26 607, 2020.

[95] M. Yoshio, H. Wang, K. Fukuda, T. Umeno, N. Dimov, and Z. Ogumi, “Carbon-coated Si as a lithium-ion battery anode material,” *Journal of The Electrochemical Society*, vol. 149, no. 12, p. 1598, 2002.

[96] Z.-L. Xu, K. Cao, S. Abouali, *et al.*, “Study of lithiation mechanisms of high performance carbon-coated Si anodes by in-situ microscopy,” *Energy Storage Materials*, vol. 3, pp. 45–54, 2016.

[97] T. Huang, D. Sun, W. Yang, H. Wang, Q. Wu, and R. Xiao, “Binder-free anode with porous Si/Cu architecture for lithium-ion batteries,” *Scripta Materialia*, vol. 146, pp. 304–307, 2018.

[98] L.-F. Cui, L. Hu, H. Wu, J. W. Choi, and Y. Cui, “Inorganic glue enabling high performance of silicon particles as lithium ion battery anode,” *Journal of the Electrochemical Society*, vol. 158, no. 5, p. 592, 2011.

[99] B. Deng, L. Shen, Y. Liu, *et al.*, “Porous Si/C composite as anode materials for high-performance rechargeable lithium-ion battery,” *Chinese Chemical Letters*, vol. 28, no. 12, pp. 2281–2284, 2017.

[100] H. Kim, B. Han, J. Choo, and J. Cho, “Three-dimensional porous silicon particles for use in high-performance lithium secondary batteries,” *Angewandte Chemie*, vol. 120, no. 52, pp. 10 305–10 308, 2008.

[101] K. Sztymela, M. Bienia, F. Rossignol, *et al.*, “Fabrication of modern Lithium Ion Batteries by 3D inkjet printing: opportunities and challenges,” *Heliyon*, p. 12 623, 2022.

[102] B. Lestriez, “Functions of polymers in composite electrodes of lithium ion batteries,” *Comptes Rendus Chimie*, vol. 13, no. 11, pp. 1341–1350, 2010.

[103] K.-A. Seı-d, J.-C. Badot, O. Dubrunfaut, S. Levasseur, D. Guyomard, and B. Lestriez, “Influence of the carboxymethyl cellulose binder on the multiscale electronic transport in carbon–$LiFePO_4$ nanocomposites,” *Journal of Materials Chemistry*, vol. 22, no. 45, pp. 24 057–24 066, 2012.

[104] Y. Liu, R. Zhang, J. Wang, and Y. Wang, “Current and future lithium-ion battery manufacturing,” *Iscience*, vol. 24, no. 4, p. 102 332, 2021.

[105] M. Schmitt, M. Baunach, L. Wengeler, *et al.*, "Slot-die processing of lithium-ion battery electrodes—Coating window characterization," *Chemical Engineering and Processing: Process Intensification*, vol. 68, pp. 32–37, 2013.

[106] C. de la Torre-Gamarra, M. Sotomayor, W. Bucheli, *et al.*, "Tape casting manufacturing of thick $Li_4Ti_5O_{12}$ ceramic electrodes with high areal capacity for lithium-ion batteries," *Journal of the European Ceramic Society*, vol. 41, no. 1, pp. 1025–1032, 2021.

[107] S. Ferrari, M. Loveridge, S. D. Beattie, M. Jahn, R. J. Dashwood, and R. Bhagat, "Latest advances in the manufacturing of 3D rechargeable lithium microbatteries," *Journal of Power Sources*, vol. 286, pp. 25–46, 2015.

[108] Z. Lyu, G. J. Lim, J. J. Koh, *et al.*, "Design and manufacture of 3D-printed batteries," *Joule*, vol. 5, no. 1, pp. 89–114, 2021.

[109] M. Nathan, D. Golodnitsky, V. Yufit, *et al.*, "Three-dimensional thin-film Li-ion microbatteries for autonomous MEMS," *Journal of microelectromechanical systems*, vol. 14, no. 5, pp. 879–885, 2005.

[110] E. Eustache, P. Tilmant, L. Morgenroth, *et al.*, "Silicon-microtube scaffold decorated with anatase TiO_2 as a negative electrode for a 3D litium-ion microbattery," *Advanced Energy Materials*, vol. 4, no. 8, p. 1 301 612, 2014.

[111] N. Li and C. R. Martin, "A high-rate, high-capacity, nanostructured Sn-based anode prepared using sol-gel template synthesis," *Journal of the Electrochemical Society*, vol. 148, no. 2, p. 164, 2001.

[112] X. Chen, K. Gerasopoulos, J. Guo, *et al.*, "Virus-enabled silicon anode for lithium-ion batteries," *ACS nano*, vol. 4, no. 9, pp. 5366–5372, 2010.

[113] A. Stein, B. E. Wilson, and S. G. Rudisill, "Design and functionality of colloidal-crystal-templated materials—chemical applications of inverse opals," *Chemical Society Reviews*, vol. 42, no. 7, pp. 2763–2803, 2013.

[114] H. Liu, H.-M. Cho, Y. S. Meng, and Q. Li, "Engineering three-dimensionally electrodeposited Si-on-Ni inverse opal structure for high volumetric capacity Li-ion microbattery anode," *ACS applied materials & interfaces*, vol. 6, no. 12, pp. 9842–9849, 2014.

[115] F. Mo, B. Guo, Q. Liu, *et al.*, "Additive manufacturing for advanced rechargeable lithium batteries: A mini review," *Frontiers in Energy Research*, vol. 10, p. 986 985, 2022.

[116] "Standard Terminology for Additive Manufacturing Technologies," ASTM International, West Conshohocken, PA, Standard, Mar. 2012.

[117] P. Chang, H. Mei, S. Zhou, K. G. Dassios, and L. Cheng, “3D printed electrochemical energy storage devices,” *Journal of Materials Chemistry A*, vol. 7, no. 9, pp. 4230–4258, 2019.

[118] R. E. Sousa, C. M. Costa, and S. Lanceros-Méndez, “Advances and future challenges in printed batteries,” *ChemSusChem*, vol. 8, no. 21, pp. 3539–3555, 2015.

[119] K. Sun, T.-S. Wei, B. Y. Ahn, J. Y. Seo, S. J. Dillon, and J. A. Lewis, “3D printing of interdigitated Li-Ion microbattery architectures,” *Advanced materials*, vol. 25, no. 33, pp. 4539–4543, 2013.

[120] A. Soleimani–Gorgani, *Inkjet printing in Printing on Polymers*, 2016.

[121] P. J. Smith and J. Stringer, “Applications in Inkjet Printing,” *Fundamentals of Inkjet Printing*, 2016.

[122] M. Singh, H. M. Haverinen, P. Dhagat, and G. E. Jabbour, “Inkjet printing—process and its applications,” *Advanced materials*, vol. 22, no. 6, pp. 673–685, 2010.

[123] F. Xu, T. Wang, W. Li, and Z. Jiang, “Preparing ultra-thin nano-MnO_2 electrodes using computer jet-printing method,” *Chemical physics letters*, vol. 375, no. 1-2, pp. 247–251, 2003.

[124] Y. Zhao, G. Liu, L. Liu, and Z. Jiang, “High-performance thin-film $Li_4Ti_5O_{12}$ electrodes fabricated by using ink-jet printing technique and their electrochemical properties,” *Journal of Solid State Electrochemistry*, vol. 13, no. 5, pp. 705–711, 2009.

[125] M. R. Arcila-Velez, J. Zhu, A. Childress, *et al.*, “Roll-to-roll synthesis of vertically aligned carbon nanotube electrodes for electrical double layer capacitors,” *Nano Energy*, vol. 8, pp. 9–16, 2014.

[126] D. Pech, M. Brunet, P.-L. Taberna, *et al.*, “Elaboration of a microstructured inkjet-printed carbon electrochemical capacitor,” *Journal of Power Sources*, vol. 195, no. 4, pp. 1266–1269, 2010.

[127] W. Zapka, “Pros and Cons of Inkjet Technology in Industrial Inkjet Printing,” *Handbook of Industrial Inkjet Printing: A Full System Approach*, pp. 1–6, 2017.

[128] M. M. Nir, D. Zamir, I. Haymov, *et al.*, “Electrically conductive inks for inkjet printing,” *the chemistry of inkjet inks*, pp. 225–254, 2010.

[129] B. Derby, “Additive manufacture of ceramics components by inkjet printing,” *Engineering*, vol. 1, no. 1, pp. 113–123, 2015.

[130] C. Goth, S. Putzo, and J. Franke, “Aerosol jet printing on rapid prototyping materials for fine pitch electronic applications,” in *2011 IEEE 61st electronic components and technology conference (ECTC)*, IEEE, 2011, pp. 1211–1216.

[131] R. Kenyon, “Ink jet printing,” in *Chemistry and technology of printing and imaging systems*, Springer, 1996, pp. 113–138.

[132] S. K. Karunakaran, G. M. Arumugam, W. Yang, *et al.*, “Recent progress in inkjet-printed solar cells,” *Journal of Materials Chemistry A*, vol. 7, no. 23, pp. 13 873–13 902, 2019.

[133] H. Tan, T. Tran, and C. Chua, “A review of printed passive electronic components through fully additive manufacturing methods,” *Virtual and Physical Prototyping*, vol. 11, no. 4, pp. 271–288, 2016.

[134] J. Li, F. Rossignol, and J. Macdonald, “Inkjet printing for biosensor fabrication: combining chemistry and technology for advanced manufacturing,” *Lab on a Chip*, vol. 15, no. 12, pp. 2538–2558, 2015.

[135] A. Hudd, *Inkjet printing technologies.* World Scientific Publishing, Hackensack, NJ, USA, 2010.

[136] B. Derby, “Inkjet printing ceramics: From drops to solid,” *Journal of the European Ceramic Society*, vol. 31, no. 14, pp. 2543–2550, 2011.

[137] B. Derby, “Inkjet printing of functional and structural materials: fluid property requirements, feature stability, and resolution,” *Annual Review of Materials Research*, vol. 40, pp. 395–414, 2010.

[138] G. D. Martin, S. D. Hoath, and I. M. Hutchings, “Inkjet printing-the physics of manipulating liquid jets and drops,” in *Journal of Physics: Conference Series*, IOP Publishing, vol. 105, 2008, p. 012 001.

[139] Ceradrop, *X-Serie TurnKey Materials Deposition Inkjet Printer*, `http://www.ceradrop.com/en/products/x-serie/`, Accessed: 2022-06-13.

[140] S. Zhou, I. Usman, Y. Wang, and A. Pan, “3D printing for rechargeable lithium metal batteries,” *Energy Storage Materials*, vol. 38, pp. 141–156, 2021.

[141] S. Arora, A. T. Abkenar, S. G. Jayasinghe, and K. Tammi, “Chapter 4 - Materials and Manufacturing Methods for Advanced Li-ion Batteries,” in *Heavy-Duty Electric Vehicles*, Butterworth-Heinemann, 2021, pp. 69–104.

[142] B. Clement, M. Lyu, E. Sandeep Kulkarni, *et al.*, “Recent Advances in Printed Thin-Film Batteries,” *Engineering*, pp. 2095–8099, 2022.

[143] Y. Zhao, Q. Zhou, L. Liu, J. Xu, M. Yan, and Z. Jiang, “A novel and facile route of ink-jet printing to thin film SnO_2 anode for rechargeable lithium ion batteries,” *Electrochimica Acta*, vol. 51, no. 13, pp. 2639–2645, 2006.

[144] J. Huang, J. Yang, W. Li, W. Cai, and Z. Jiang, “Electrochemical properties of $LiCoO_2$ thin film electrode prepared by ink-jet printing technique,” *Thin Solid Films*, vol. 516, no. 10, pp. 3314–3319, 2008.

[145] Y. Gu, A. Wu, H. Sohn, C. Nicoletti, Z. Iqbal, and J. F. Federici, "Fabrication of rechargeable lithium ion batteries using water-based inkjet printed cathodes," *Journal of Manufacturing Processes*, vol. 20, pp. 198–205, 2015.

[146] P.-E. Delannoy, B. Riou, T. Brousse, J. Le Bideau, D. Guyomard, and B. Lestriez, "Ink-jet printed porous composite $LiFePO_4$ electrode from aqueous suspension for microbatteries," *Journal of Power Sources*, vol. 287, pp. 261–268, 2015.

[147] P.-E. Delannoy, B. Riou, B. Lestriez, D. Guyomard, T. Brousse, and J. Le Bideau, "Toward fast and cost-effective ink-jet printing of solid electrolyte for lithium microbatteries," *Journal of Power Sources*, vol. 274, pp. 1085–1090, 2015.

[148] S. Lawes, Q. Sun, A. Lushington, B. Xiao, Y. Liu, and X. Sun, "Inkjet-printed silicon as high performance anodes for Li-ion batteries," *Nano Energy*, vol. 36, pp. 313–321, 2017.

[149] S. D. Lawes, "Inkjet Printed Thin Film Electrodes for Lithium-Ion Batteries," Ph.D. dissertation, The University of Western Ontario, 2015.

[150] M. Maximov, D. Kolchanov, I. Mitrofanov, *et al.*, "Inks development for 3D printing cathode of Li-ion microbatteries," *Multidisciplinary Digital Publishing Institute Proceedings*, vol. 3, no. 1, p. 7, 2018.

[151] D. S. Kolchanov, I. Mitrofanov, A. Kim, *et al.*, "Inkjet printing of Li-rich cathode material for thin-film lithium-ion microbatteries," *Energy Technology*, vol. 8, no. 3, p. 1 901 086, 2020.

[152] Y. Wang, T. Lubbers, R. Xia, *et al.*, "Printable two-dimensional V_2O_5/MXene heterostructure cathode for lithium-ion battery," *Journal of The Electrochemical Society*, vol. 168, no. 2, p. 020 507, 2021.

[153] P. Viviani, E. Gibertini, F. Iervolino, M. Levi, and L. Magagnin, "Carbon additive effect on the electrochemical performances of inkjet printed thin-film $Li_4Ti_5O_{12}$ electrodes," *Journal of Manufacturing Processes*, vol. 72, pp. 411–418, 2021.

[154] A. Kushwaha, M. K. Jangid, B. B. Bhatt, A. Mukhopadhyay, and D. Gupta, "Inkjet-printed environmentally friendly graphene film for application as a high-performance anode in Li-ion batteries," *ACS Applied Energy Materials*, vol. 4, no. 8, pp. 7911–7921, 2021.

[155] C.-C. Li and Y.-W. Wang, "Importance of binder compositions to the dispersion and electrochemical properties of water-based $LiCoO_2$ cathodes," *Journal of power sources*, vol. 227, pp. 204–210, 2013.

[156] M. Cerbelaud, B. Lestriez, A. Videcoq, R. Ferrando, and D. Guyomard, "Understanding the structure of electrodes in Li-ion batteries: a numerical study," *Journal of The Electrochemical Society*, vol. 162, no. 8, p. 1485, 2015.

[157] K. Konda, S. B. Moodakare, P. L. Kumar, *et al.*, "Comprehensive effort on electrode slurry preparation for better electrochemical performance of $LiFePO_4$ battery," *Journal of Power Sources*, vol. 480, p. 228 837, 2020.

[158] K. M. Kim, W. S. Jeon, I. J. Chung, and S. H. Chang, "Effect of mixing sequences on the electrode characteristics of lithium-ion rechargeable batteries," *Journal of power sources*, vol. 83, no. 1-2, pp. 108–113, 1999.

[159] G. H. McKinley and M. Renardy, "Wolfgang von Ohnesorge," *Physics of Fluids*, vol. 23, no. 12, p. 127 101, 2011.

[160] J. Fromm, "Numerical calculation of the fluid dynamics of drop-on-demand jets," *IBM Journal of Research and Development*, vol. 28, no. 3, pp. 322–333, 1984.

[161] N. Reis and B. Derby, "Ink jet deposition of ceramic suspensions: Modeling and experiments of droplet formation," *MRS Online Proceedings Library (OPL)*, vol. 625, 2000.

[162] A. K. Mogalicherla, S. Lee, P. Pfeifer, and R. Dittmeyer, "Drop-on-demand inkjet printing of alumina nanoparticles in rectangular microchannels," *Microfluidics and nanofluidics*, vol. 16, no. 4, pp. 655–666, 2014.

[163] P. C. Duineveld, M. M. De Kok, M. Buechel, *et al.*, "Ink-jet printing of polymer light-emitting devices," in *Organic Light-Emitting Materials and Devices V*, SPIE, vol. 4464, 2002, pp. 59–67.

[164] C. D. Stow and M. G. Hadfield, "An experimental investigation of fluid flow resulting from the impact of a water drop with an unyielding dry surface," *Proceedings of the Royal Society of London. A. Mathematical and Physical Sciences*, vol. 373, no. 1755, pp. 419–441, 1981.

[165] L. Bergstrom, "Colloidal processing of ceramics," *Handbook of applied surface and colloid chemistry*, vol. 1, pp. 201–217, 2001.

[166] H. J. Shore and G. M. Harrison, "The effect of added polymers on the formation of drops ejected from a nozzle," *Physics of fluids*, vol. 17, no. 3, p. 033 104, 2005.

[167] D. McKinney and W. Sigmund, "Chapter 11.1.3 - Colloidal Processing Fundamentals," in *Handbook of Advanced Ceramics (Second Edition)*, S. Somiya, Ed., Second Edition, Oxford: Academic Press, 2013, pp. 911–926.

[168] B. He, S. Yang, Z. Qin, B. Wen, and C. Zhang, "The roles of wettability and surface tension in droplet formation during inkjet printing," *Scientific reports*, vol. 7, no. 1, pp. 1–7, 2017.

[169] M. Bienia, M. Lejeune, M. Chambon, *et al.*, "Inkjet printing of ceramic colloidal suspensions: Filament growth and breakup," *Chemical Engineering Science*, vol. 149, pp. 1–13, 2016.

[170] G. Vescio, J. López-Vidrier, R. Leghrib, A. Cornet, and A. Cirera, “Flexible inkjet printed high-k HfO_2-based MIM capacitors,” *Journal of Materials Chemistry C*, vol. 4, no. 9, pp. 1804–1812, 2016.

[171] D. Kuscer and J. Z. Shen, “Advanced direct forming processes for the future,” in *Advanced Ceramics for Dentistry*, Elsevier, 2014, pp. 375–390.

[172] S. Sharma, S. S. Pande, and P. Swaminathan, “Top-down synthesis of zinc oxide based inks for inkjet printing,” *RSC advances*, vol. 7, no. 63, pp. 39 411–39 419, 2017.

[173] C. D. Modak, A. Kumar, A. Tripathy, and P. Sen, “Drop impact printing,” *Nature communications*, vol. 11, no. 1, pp. 1–11, 2020.

[174] J. Zikulnig and J. Kosel, “Flexible Printed Sensors—Overview of Fabrication Technologies,” in *Reference Module in Biomedical Sciences*, 2021.

[175] X.-J. Zhang, “Van der Waals Forces,” in *Encyclopedia of Tribology*, Q. J. Wang, Ed., Boston, MA: Springer US, 2013, pp. 3945–3947.

[176] W. Sigmund, G. Pyrgiotakis, and A. Daga, “11 Theory and Applications of Colloidal Processing,” *Chemical processing of ceramics*, p. 269, 2005.

[177] A. K. Alias, *Emulsion stability [powerpoint slides]*, `https://www.slideshare.net/akarim717/emulsion-stability`, Accessed: 2022-09-20, 2015.

[178] S.-J. Park and M.-K. Seo, “Intermolecular force,” *Interface science and technology*, vol. 18, pp. 1–57, 2011.

[179] K. Pate and P. Safier, “Chemical metrology methods for CMP quality,” in *Advances in chemical mechanical planarization (CMP)*, Elsevier, 2022, pp. 355–383.

[180] T. Tadros, “Electrostatic and steric stabilization of colloidal dispersions,” *Electrical phenomena at interfaces and biointerfaces*, pp. 153–172, 2012.

[181] M. Trunec and K. Maca, *Advanced Ceramics for Dentistry: Chapter 7. Advanced Ceramic Processes*. Elsevier Inc. Chapters, 2013.

[182] S. Leo, C. Tallon, and G. V. Franks, “Aqueous and nonaqueous colloidal processing of difficult-to-densify ceramics: suspension rheology and particle packing,” *Journal of the American Ceramic Society*, vol. 97, no. 12, pp. 3807–3817, 2014.

[183] *FUJIFILM United States*, `https://www.fujifilm.com/us/en/business/inkjet-solutions/industrial-printheads/sl-128-aa`, Accessed: 2023-02-08.

[184] *Elcometer*, `https://www.elcometer.com/en/`, Accessed: 2023-02-08.

[185] V. Selvamani, “Stability studies on nanomaterials used in drugs,” in *Characterization and biology of nanomaterials for drug delivery*, Elsevier, 2019, pp. 425–444.

[186] H. Ohshima, “Zeta potential,” in *Encyclopedia of Colloid and Interface Science*, T. Tadros, Ed. Berlin, Heidelberg: Springer Berlin Heidelberg, 2013, pp. 1423–1436.

[187] Y. Lu, W. Kang, J. Jiang, *et al.*, "Study on the stabilization mechanism of crude oil emulsion with an amphiphilic polymer using the β-cyclodextrin inclusion method," *RSC advances*, vol. 7, no. 14, pp. 8156–8166, 2017.

[188] X.-L. Wang, K. An, L. Cai, *et al.*, "Visualizing the chemistry and structure dynamics in lithium-ion batteries by in-situ neutron diffraction," *Scientific Reports*, vol. 2, no. 1, p. 747, 2012.

[189] R. Wahab, N. Ahmad, and M. Alam, "Silicon nanoparticles: a new and enhanced operational material for nitrophenol sensing," *Journal of Materials Science: Materials in Electronics*, vol. 31, pp. 17 084–17 099, 2020.

[190] P. Bu, S. Liu, Y. Lu, S. Zhuang, H. Wang, and F. Tu, "Effects of carbon black on the electrochemical performance of lithium-organic coordination compound batteries," *Int. J. Electrochem. Sci*, vol. 7, pp. 4617–4624, 2012.

[191] J.-B. Donnet and A. Voet, *Carbon black: physics, chemistry, and elastomer reinforcement.* M. Dekker, 1976.

[192] J. Biscoe and B. Warren, "An x-ray study of carbon black," *Journal of Applied Physics*, vol. 13, no. 6, pp. 364–371, 1942.

[193] K. M. Łęcka, B. D. Stępak, P. Kunicki, and A. J. Antończak, *The influence of laser radiation on pyrolytic carbon.* Conference: Influence of Young Scientists on the Polish Science Achievements At: Wrocław, Poland, 2017.

[194] H. Zhang, L. Ben, H. Yu, W. Qi, W. Zhao, and X. Huang, "Ultrathin Ta_2O_5-coated super P carbon black as a stable conducting additive for lithium batteries charged to 4.9 Vat 55°C," *Carbon*, vol. 162, pp. 519–527, 2020.

[195] V. Palomares, A. Goñi, I. G. De Muro, *et al.*, "Conductive additive content balance in Li-ion battery cathodes: Commercial carbon blacks vs. in situ carbon from $LiFePO_4$/C composites," *Journal of Power Sources*, vol. 195, no. 22, pp. 7661–7668, 2010.

[196] S. Hidayat, P. Ardiaksa, N. Riveli, and I. Rahayu, "Synthesis and characterization of carboxymethyl cellulose (CMC) from salak-fruit seeds as anode binder for lithium-ion battery," in *Journal of Physics: Conference Series*, IOP Publishing, vol. 1080, 2018, p. 012 017.

[197] C. G. Lopez, S. E. Rogers, R. H. Colby, P. Graham, and J. T. Cabral, "Structure of sodium carboxymethyl cellulose aqueous solutions: A SANS and rheology study," *Journal of Polymer Science Part B: Polymer Physics*, vol. 53, no. 7, pp. 492–501, 2015.

[198] M. Ndour, J.-P. Bonnet, S. Cavalaglio, *et al.*, "The formulation of a CMC binder/silicon composite anode for Li-ion batteries: from molecular effects of ball milling on poly-

mer chains to consequences on electrochemical performances," *Materials Advances*, vol. 3, no. 23, pp. 8522–8533, 2022.

[199] Y. J. Cheon, "Direct Observation of Carboxymethyl cellulose (CMC) and Styrene-Butadiene Rubber (SBR) Binder Distribution in Practical Graphite Anodes for Li-Ion System," Ph.D. dissertation, 2020.

[200] K. Sun, S. Zhang, P. Li, *et al.*, "Review on application of PEDOTs and PEDOT: PSS in energy conversion and storage devices," *Journal of Materials Science: Materials in Electronics*, vol. 26, pp. 4438–4462, 2015.

[201] P. R. Das, L. Komsiyska, O. Osters, and G. Wittstock, "PEDOT: PSS as a functional binder for cathodes in lithium ion batteries," *Journal of The Electrochemical Society*, vol. 162, no. 4, p. 674, 2015.

[202] S. Bai, Y. Ma, X. Jiang, *et al.*, "Greatly improved cyclability for Li-ion batteries with a PEDOT–PSS coated nanostructured Ge anode," *Surfaces and Interfaces*, vol. 8, pp. 214–218, 2017.

[203] L. Fernandez-Diaz, J. Castillo, E. Sasieta-Barrutia, *et al.*, "Mixing methods for solid state electrodes: Techniques, fundamentals, recent advances, and perspectives," *Chemical Engineering Journal*, vol. 464, p. 142 469, 2023.

[204] J. Alonso, J. M. Barandiarán, L. F. Barquín, and A. García-Arribas, "Magnetic nanoparticles, synthesis, properties, and applications," in *Magnetic nanostructured materials*, Elsevier, 2018, pp. 1–40.

[205] F. Lemoisson and L. Froyen, "Understanding and improving powder metallurgical processes," 2005.

[206] M. S. El-Eskandarany, "Controlling the powder milling process," *Mechanical Alloying*, pp. 48–83, 2015.

[207] T. Pan, J. Alvarado, J. Zhu, *et al.*, "Structural degradation of layered cathode materials in lithium-ion batteries induced by ball milling," *Journal of the Electrochemical Society*, vol. 166, no. 10, p. 1964, 2019.

[208] S. Patoux and M. M. Doeff, "Direct synthesis of $LiNi_{1/3}Co_{1/3}Mn_{1/3}O_2$ from nitrate precursors," *Electrochemistry Communications*, vol. 6, no. 8, pp. 767–772, 2004.

[209] J. Reimers, E. Rossen, C. Jones, and J. Dahn, "Structure and electrochemistry of $Li_xFe_yNi_{1-y}O_2$," *Solid State Ionics*, vol. 61, no. 4, pp. 335–344, 1993.

[210] M. Latifatu, C. Y. Bon, K. S. Lee, *et al.*, "Structural Effect of Conductive Carbons on the Adhesion and Electrochemical Behavior of $LiNi_{0.4}Mn_{0.4}Co_{0.2}O_2$ Cathode for Lithium Ion Batteries," *Journal of Electrochemical Science and Technology*, vol. 9, no. 4, pp. 330–338, 2018.

[211] C. Park, S. Lee, K. Kim, M. Kim, S. Choi, and D. Shin, "Electrochemical Properties of composite cathode using bimodal sized electrolyte for all-solid-state batteries," *Journal of The Electrochemical Society*, vol. 166, no. 3, p. 5318, 2019.

[212] V. Wurster, C. Engel, H. Graebe, T. Ferber, W. Jaegermann, and R. Hausbrand, "Characterization of the interfaces in $LiFePO_4$/PEO-LiTFSI composite cathodes and to the adjacent layers," *Journal of The Electrochemical Society*, vol. 166, no. 3, p. 5410, 2019.

[213] J. Zheng, J. Xiao, and J.-G. Zhang, "The roles of oxygen non-stoichiometry on the electrochemical properties of oxide-based cathode materials," *Nano Today*, vol. 11, no. 5, pp. 678–694, 2016.

[214] A. D. Prasetya, M. Rifai, H. Miyamoto, *et al.*, "X-ray diffraction (XRD) profile analysis of pure ECAP-annealing Nickel samples," in *Journal of Physics: Conference Series*, IOP Publishing, vol. 1436, 2020, p. 012 113.

[215] C. Busá, M. Belekoukia, and M. J. Loveridge, "The effects of ambient storage conditions on the structural and electrochemical properties of NMC-811 cathodes for Li-ion batteries," *Electrochimica Acta*, vol. 366, p. 137 358, 2021.

[216] Y. Waseda, E. Matsubara, and K. Shinoda, "X-ray diffraction crystallography: introduction, examples and solved problems," in Springer Science & Business Media, 2011, ch. Diffraction from Polycrystalline Samples and Determination of Crystal Structure.

[217] T. Ungar, "Microstructural parameters from X-ray diffraction peak broadening," *Scripta Materialia*, vol. 51, no. 8, pp. 777–781, 2004.

[218] V. Vinila and J. Isac, "Synthesis and structural studies of superconducting perovskite $GdBa_2Ca_3Cu_4O_{10.5+\delta}$ nanosystems," in *Design, Fabrication, and Characterization of Multifunctional Nanomaterials*, Elsevier, 2022, pp. 319–341.

[219] J. I. Langford and A. Wilson, "Scherrer after sixty years: a survey and some new results in the determination of crystallite size," *Journal of applied crystallography*, vol. 11, no. 2, pp. 102–113, 1978.

[220] A. Monshi, M. R. Foroughi, M. R. Monshi, *et al.*, "Modified Scherrer equation to estimate more accurately nano-crystallite size using XRD," *World journal of nano science and engineering*, vol. 2, no. 3, pp. 154–160, 2012.

[221] M. N. ur Rehman, T. Munawar, M. S. Nadeem, *et al.*, "Facile synthesis and characterization of conducting polymer-metal oxide based core-shell PANI-Pr_2O–NiO–Co_3O_4 nanocomposite: As electrode material for supercapacitor," *Ceramics International*, vol. 47, no. 13, pp. 18 497–18 509, 2021.

[222] S. A.-A. Jabir and K. H. Harbbi, “A comparative study of Williamson-Hall method and size-strain method through x-ray diffraction pattern of cadmium oxide nanoparticle,” in *AIP Conference Proceedings*, AIP Publishing LLC, vol. 2307, 2020, p. 020 015.

[223] A. H. Abed, Z. T. Khodair, T. M. Al-Saadi, and T. A. Al-Dhahir, “Study the evaluation of Williamson–Hall (WH) strain distribution in silver nanoparticles prepared by sol-gel method,” in *AIP Conference Proceedings*, AIP Publishing LLC, vol. 2123, 2019, p. 020 019.

[224] G. Williamson and W. Hall, “X-ray line broadening from filed aluminium and wolfram,” *Acta metallurgica*, vol. 1, no. 1, pp. 22–31, 1953.

[225] S. Subramanian and G. Øye, “Aqueous carbon black dispersions stabilized by sodium lignosulfonates,” *Colloid and Polymer Science*, vol. 299, no. 7, pp. 1223–1236, 2021.

[226] C. G. Kolb, M. Lehmann, J.-L. Lindemann, A. Bachmann, and M. F. Zaeh, “Improving the dispersion behavior of organic components in water-based electrode dispersions for inkjet printing processes,” *Applied Sciences*, vol. 11, no. 5, p. 2242, 2021.

[227] J.-S. Bridel, T. Azais, M. Morcrette, J.-M. Tarascon, and D. Larcher, “Key parameters governing the reversibility of Si/carbon/CMC electrodes for Li-ion batteries,” *Chemistry of materials*, vol. 22, no. 3, pp. 1229–1241, 2010.

[228] J. Kang, “High molecular weight carboxymethyl cellulose binder to enhance integrity of silicon anodes for li-ion batteries,” 2019.

[229] A. M. Escamilla-Pérez, A. Roland, S. Giraud, *et al.*, “Pitch-based carbon/nano-silicon composite, an efficient anode for li-ion batteries,” *RSC advances*, vol. 9, no. 19, pp. 10 546–10 553, 2019.

[230] A. Roland, J. Fullenwarth, J.-B. Ledeuil, H. Martinez, N. Louvain, and L. Monconduit, “How carbon coating or continuous carbon pitch matrix influence the silicon electrode/electrolyte interfaces and the performance in Li-ion batteries,” *Battery Energy*, vol. 1, no. 1, p. 20 210 009, 2022, https://doi.org/10.1002/bte2.20210009.

[231] Y. Li, O. Dahhan, C. D. Filipe, J. D. Brennan, and R. H. Pelton, “Optimizing piezoelectric inkjet printing of silica sols for biosensor production,” *Journal of Sol-Gel Science and Technology*, vol. 87, pp. 657–664, 2018.

[232] Y. Li, O. Dahhan, C. D. Filipe, J. D. Brennan, and R. H. Pelton, “Deposited nanoparticles can promote air clogging of piezoelectric inkjet printhead nozzles,” *Langmuir*, vol. 35, no. 16, pp. 5517–5524, 2019.

[233] G. Mussabek, S. A. Alekseev, A. I. Manilov, *et al.*, “Kinetics of hydrogen generation from oxidation of hydrogenated silicon nanocrystals in aqueous solutions,” *Nanomaterials*, vol. 10, no. 7, p. 1413, 2020.

[234] D. B. Mawhinney, J. A. Glass, and J. T. Yates, “FTIR study of the oxidation of porous silicon,” *The Journal of Physical Chemistry B*, vol. 101, no. 7, pp. 1202–1206, 1997.

[235] K. N. Al-Milaji and H. Zhao, “New Perspective of mitigating the coffee-ring effect: Interfacial assembly,” *The Journal of Physical Chemistry C*, vol. 123, no. 19, pp. 12 029–12 041, 2019.

[236] I. A. Shkrob, J. A. Gilbert, P. J. Phillips, *et al.*, “Chemical weathering of layered Ni-rich oxide electrode materials: evidence for cation exchange,” *Journal of The Electrochemical Society*, vol. 164, no. 7, p. 1489, 2017.

[237] S.-M. Bak, E. Hu, Y. Zhou, *et al.*, “Structural changes and thermal stability of charged $\mathrm{LiNi}_x\mathrm{Mn}_y\mathrm{Co}_z\mathrm{O}_2$ cathode materials studied by combined in situ time-resolved XRD and mass spectroscopy,” *ACS applied materials & interfaces*, vol. 6, no. 24, pp. 22 594–22 601, 2014.

[238] M. Wood, J. Li, R. E. Ruther, *et al.*, “Chemical stability and long-term cell performance of low-cobalt, Ni-Rich cathodes prepared by aqueous processing for high-energy Li-Ion batteries,” *Energy Storage Materials*, vol. 24, pp. 188–197, 2020.

[239] D. Jang, D. Kim, and J. Moon, “Influence of fluid physical properties on ink-jet printability,” *Langmuir*, vol. 25, no. 5, pp. 2629–2635, 2009.

[240] B.-J. de Gans, L. Xue, U. S. Agarwal, and U. S. Schubert, “Ink-Jet Printing of Linear and Star Polymers,” *Macromolecular Rapid Communications*, vol. 26, no. 4, pp. 310–314, 2005.

[241] D. Xu, V. Sanchez-Romaguera, S. Barbosa, *et al.*, “Inkjet printing of polymer solutions and the role of chain entanglement,” *Journal of Materials Chemistry*, vol. 17, no. 46, pp. 4902–4907, 2007.

[242] S. D. Hoath, D. C. Vadillo, O. G. Harlen, *et al.*, “Inkjet printing of weakly elastic polymer solutions,” *Journal of Non-Newtonian Fluid Mechanics*, vol. 205, pp. 1–10, 2014.

[243] B.-J. de Gans, E. Kazancioglu, W. Meyer, and U. S. Schubert, “Ink-jet printing polymers and polymer libraries using micropipettes,” *Macromolecular Rapid Communications*, vol. 25, no. 1, pp. 292–296, 2004.

[244] H. Dong, W. W. Carr, and J. F. Morris, “Visualization of drop-on-demand inkjet: Drop formation and deposition,” *Review of Scientific Instruments*, vol. 77, no. 8, p. 085 101, 2006.

List of works

Publications

- Sztymela K., Bienia M., Rossignol F., Mailley S., Ziesche S., Varghese J., Cerbelaud M., "Fabrication of modern lithium ion batteries by 3D inkjet printing: opportunities and challenges," *Heliyon*, 2022 Dec 27: e12623.
- Sztymela K., Rossignol F., Bienia M., Zapp N., Nikolowski K., Cerbelaud M., "Fabrication of 3D silicon anode by inkjet printing: opportunities and challenges", *Journal of Energy Storage*, 2024 Jan 1: 75:109567.
- Sztymela K., Rossignol F., Geffroy P.M., Murat Y., Cerbelaud M., "Impact of grinding on the structural and electrochemical properties of NMC622 cathode material", *Ceramics International*, 2023, submitted.

Conferences

- Sztymela K., Cerbelaud M., Rossignol F., "Cathode ink formulation for inkjet printing technology", oral presentation, *CERAMICS IN EUROPE*, ECerS XVII, Jul 2022, Cracovie, Poland.
- Sztymela K., Bienia M., Cerbelaud M., Rossignol F., "Fabrication of composite electrodes for Lithium-ion batteries by inkjet printing technology", oral presentation, *Shaping8*, Empa, ECerS, Sept 2022, Dübendorf, Switzerland.
- Sztymela K., Cerbelaud M., Rossignol F., Bienia M., "Inkjet printing for the fabrication of Lithium-ion batteries: opportunities and challenges ", oral presentation, *ICACC*, ACerS, Jan 2023, Daytona Beach, USA.

Fabrication of 3D electrodes for modern lithium-ion batteries by inkjet printing: opportunities and challenges

Abstract: Owing to high energy density, high operating voltage, and long cycle life, lithium-ion batteries (LIBs) are currently the leading energy storage technology for mobile devices and electric vehicles. The LIB market is continuously expanding and is expected to remain the preferred battery technology in the short- to medium-term future. Although LIBs are already well-developed, there is still potential to improve their performance, safety, and cost, and one promising approach for achieving this is through the use of a three-dimensional (3D) electrode structure. Additive manufacturing techniques, such as inkjet printing (IJP), offer the advantages of rapid deposition of thin films or complex patterns with high precision. This study explores the possibilities and challenges associated with the fabrication of 3D composite electrodes using IJP technology. The physical and rheological properties of the composite inks are adjusted to meet the requirements of IJP, and the effect of these formulations on the electrochemical characteristics of the electrodes is assessed. The printability tests are presented revealing a problem of process instabilities, and their underlying causes are explained. Finally, microstructural characterization of deposited 3D patterns is demonstrated.

Keywords: Inkjet printing; Lithium-ion batteries; Electrodes; Printability; Three-dimensional structures; Ink formulation.

Fabrication par impression jet d'encre d'électrodes 3D pour les nouvelles batteries Li-ion: opportunités et défis

Résumé : En raison de leur densité d'énergie élevée, leur tension de fonctionnement élevée et leur longue durée de vie, les batteries lithium-ion (LIB) sont actuellement la technologie de stockage d'énergie la plus avancée pour les appareils mobiles et les véhicules électriques. Le marché des LIB est en constante expansion et devrait rester la technologie de batterie préférée à court et moyen termes. Bien que les LIB soient déjà bien développées, il y a du potentiel pour améliorer leurs performances, leur sécurité et leur coût. Une approche prometteuse pour y parvenir est l'utilisation d'une structure d'électrode tridimensionnelle (3D). Les techniques de fabrication additive, telles que l'impression jet d'encre (IJP), offrent les avantages d'un dépôt rapide de films minces ou de motifs complexes avec une grande précision. Cette étude explore les possibilités et les défis associés à la fabrication d'électrodes composites 3D à l'aide de cette technologie IJP. Les propriétés physiques et rhéologiques des encres composites sont ajustées pour répondre aux exigences de l'IJP, et l'effet de ces formulations sur les caractéristiques électrochimiques des électrodes est évalué. Les tests d'impression sont présentés, révélant un problème d'instabilités du procédé, et leurs causes sous-jacentes sont expliquées. Enfin, la caractérisation microstructurale des motifs 3D déposés est démontrée.

Mots clés : Impression jet d'encre; Batteries lithium-ion; Electrodes; Imprimabilité; Structures tridimensionnelles; Formulation d'encre.